Ambient backscatter communications in future mobile networks

Romain Fara

université PARIS-SACLAY

Communications par rétrodiffusion ambiante dans les futurs réseaux mobiles

Ambient backscatter communications in future mobile networks

Thèse de doctorat de l'université Paris-Saclay préparée à CentraleSupélec

École doctorale n° 580 Sciences et technologies de l'information et de la communication (STIC)
Spécialité de doctorat : Réseaux, information et communications
Unité de recherche : Université Paris-Saclay, CNRS, CentraleSupélec, Laboratoire des signaux et systèmes, 91190, Gif-sur-Yvette, France
Référent : CentraleSupélec

Thèse présentée et soutenue à Paris-Saclay, le 15/10/2021, par

Romain FARA

Composition du Jury

Alain SIBILLE Professeur (HDR), Telecom Paris, IP Paris	Président du Jury
Carlos BADER Directeur de la Recherche (HDR), ISEP	Rapporteur & Examinateur
Laurent CLAVIER Professeur (HDR), IMT Lille Douai	Rapporteur & Examinateur
Martine LIENARD Professeure (HDR), Université Lille 1	Examinatrice
Inbar FIJALKOW Professeure (HDR), ENSEA	Examinatrice

Direction de la thèse

Marco DI RENZO Directeur CNRS (HDR), Université Paris-Saclay	Directeur de thèse
Dinh-Thuy PHAN-HUY Ingénieure de Recherche, Orange Labs	Co-Encadrante de thèse
Julien DE ROSNY Directeur CNRS (HDR), Université PSL	Co-Encadrant de thèse

Thèse de doctorat

NNT : 2021UPASG057

université PARIS-SACLAY

ÉCOLE DOCTORALE
Sciences et technologies de l'information et de la communication (STIC)

Titre : Communications par rétrodiffusion ambiante dans les futurs réseaux mobiles.

Mots clés : Rétrodiffusion ambiante, Internet des Objets, Modulation Spatiale, 5G, 6G.

Résumé : Comment rendre les villes, les usines et les maisons à la fois intelligentes et sensibles aux hommes ? Pour y parvenir il est possible d'équiper les personnes, les villes, les usines et les maisons de dispositifs radio pour communiquer des messages, grâce à l'Internet des objets. Cependant, les émissions radio permanentes s'accompagnent d'une dépense énergétique rédhibitoire.

La technologie de communication par rétrodiffusion ambiante (AmBC) permet de communiquer sans émettre d'onde radio supplémentaires, en exploitant les ondes radio ambiantes (Wifi, diffusion TV ou FM, cellulaire, etc.). Les dispositifs AmBC rétrodiffusent le champ électromagnétique ambiant grâce à une antenne connectée à une impédance variable. L'information est alors communiquée à un récepteur en modulant l'impédance du dispositif AmBC. Grâce à leur très faible consommation, ils peuvent être alimentés par un système de récupération d'énergie. Cependant la portée et le débit restent encore très limités.

Dans ce travail, nous nous focalisons sur l'étude des améliorations de cette technologie en tirant profit des réseaux mobiles du futur.

Premièrement nous montrons que les antennes compactes reconfigurables peuvent avantageusement remplacer les antennes à impédance ajustable dans les dispositifs AmBC. Ces antennes compactes reconfigurables utilisent différents diagrammes de rayonnement et différentes polarisations pour rendre plus robuste la communication.

Deuxièmement nous démontrons que les antennes existantes au sein des réseaux 5G peuvent être utilisées dans les systèmes AmBC afin d'améliorer significativement leur débit et leur portée.
Dans un scénario 5G, l'antenne « massive Multiple-Input Multiple-Output » (mMIMO) de la station de base peut être utilisée comme source d'ondes ambiantes pour créer des zones de forte puissance et des zones de bonne réception grâce à la technique de précodage. Ces zones visent à améliorer les performances de la communication entre le dispositif AmBC et le récepteur. Nous démontrons également que l'antenne mMIMO peut aussi être utilisée comme récepteur pour améliorer la détection des dispositifs AmBC.

Enfin nous montrons qu'une technologie émergente pour la 6G, appelée surface intelligente reconfigurable (RIS), qui permet de contrôler partiellement le canal de propagation des ondes, peut assister les systèmes AmBC. Nous montrons qu'il est possible d'exploiter la capacité de formation de faisceau de manière passive de la technologie RIS pour améliorer la performance des systèmes AmBC.

Maison du doctorat de l'Université Paris-Saclay
2ème étage aile ouest, Ecole normale supérieure Paris-Saclay
4 avenue des Sciences,
91190 Gif sur Yvette, France

Title : Ambient backscatter communication in future mobile networks.

Keywords : Ambient Backscatter, Internet of Things, Spatial Modulation, 5G, 6G.

Abstract : How can cities, factories and homes be made both intelligent and responsive to people? To achieve this, it is possible to equip people, cities, factories and houses with radio devices to communicate messages, thanks to the Internet of things. However, permanent radio emissions result in a crippling energy expense.

Ambient Backscatter Communication (AmBC) technology enables communication without the need for additional radio emission, by exploiting ambient radio waves (Wi-Fi, TV or FM broadcast, cellular, etc.). AmBC devices, named tags, backscatter the ambient electromagnetic field thanks to an antenna connected to a tunable impedance. The information is communicated to a reader by modulating the impedance of the AmBC tag. Therefore, thanks to their very low consumption, they can be powered by energy harvesting. However, the range and the data rate of these devices are still very limited.

We focus this work on the study of improvements of this technology by taking advantage of the future mobile networks.

Firstly, we show that the compact reconfigurable antennas can advantageously replace antenna with tunable impedance in AmBC tags. Such compact reconfigurable antennas use different radiation patterns and polarizations to make the communication more robust.

Secondly, we demonstrate that existing antennas within 5G networks can be used in AmBC systems to significantly improve the data rate and the range of the AmBC tags. In a 5G scenario, the massive Multiple-Input Multiple-Output (mMIMO) antenna of the base station can be used as source of ambient waves to create hot spots and good reception spots thanks to the precoding technique. These spots aim at improving the performance of the communication from the tag to the reader. We demonstrate also that the mMIMO antenna can also be used as reader to enhance the detection of AmBC tags.

Finally, we show that an emerging technology for 6G, called reconfigurable intelligent surface (RIS), which allows to partially control the wave propagation channel, can assist AmBC systems. We exploit the passive beamforming capability of the RIS technology to improve the performance of AmBC systems.

Acknowledgements

I would like to thank my advisors Prof. Marco Di Renzo, Dr. Dinh-Thuy Phan-Huy and Prof. Julien De Rosny for giving me the opportunity to work on this thesis. I am extremely thankful for your confidence, your patience, your continuous support and your precious advices.

I would also like to thank my committee members Prof. Alain Sibille, Prof. Carlos Bader, Prof. Laurent Clavier, Prof. Martine Lienard and Prof. Inbar Fijalkow for serving as my committee members and for their valuable comments.

I would like to express my sincere gratitude to my colleagues who shared with me their knowledge and helped me in my research work, in setting up the experiments, in obtaining and analysing new results. I would like to thank everyone and especially my colleagues and my managers in Orange who gave me the opportunity to share and present my research work during events, congress and conferences.

Finally, I would like to thanks my parents, my sister, my family, my friends, my colleagues from Orange and CentraleSupelec for their support during my PhD, and for their encouragement to strive towards my goal. I would extend my sincere thanks to everyone who contributed directly or indirectly to my PhD work.

Table of contents

List of figures

List of tables

List of acronyms

IoT	Internet of Things
RFID	Radio-Frequency Identification
LoRAWAN	Long Range WAN
AmBC	Ambient Backscatter Communication
EM	Electromagnetic
5G	Fifth Generation of Mobile Networks
SM	Spatial Modulation
6G	Sixth Generation of Mobile Networks
MIMO	Multiple-Input Multiple-Output
RISs	Reconfigurable Intelligent Surfaces
mMIMO	Massive MIMO
LSE	Least Square Error
BER	Bit Error Rate
RF	Radio Frequency
MBC	Monostatic Backscatter Communications
BBC	Bistatic Backscatter Communications
BS	Base Station
TV	Television
OFDM	Orthogonal Frequency Division Multiplexing
LOS	Line-of-Sight
SNR	Signal-to-Noise Ratio
PIN diode	Positive Intrinsic Negative diode
UEs	User Equipments
LDPC	Low-Density Parity-Check channel coding
3GPP	3rd Generation Partnership Project
mmWave	Millimeter Wavelengths
MRT	Maximum Ratio Transmission
ZF	Zero Forcing

CSI	Channel State Information
MMSE	Minimum Mean Square Error
Tx	Transmitter
Rx	Receiver
ML	Machine Learning
PR	Polarization-based Reconfigurable
BTS	Backscattering/Transparent Scheme
MoM	Method of Moments
PCS	Polarization Coding Scheme
IPR	“Ideal” Polarization Reconfigurable
4PR	4-Polarization Reconfigurable
NR	Non-Reconfigurable
SRR	Split Ring Resonators
XPOL	Cross-Polarization Antenna
ED	Energy Detector
NEC	Numerical Electromagnetic Code
NLOS	Non Line-of-Sight
SCAT	Scattering
SRS	Sounding Reference Signals
CSIT	Channel State Information at the Transmission
CC	Coherent Combining
S	Source
T	Tag
R	Reader
D	Legacy device
REF	Reference
QoS	Quality of Service
CDF	Cumulative Distribution Function
SUPA	Slant Uniform Planar Array
AWGN	Additive White Gaussian Noise
OFF	Transparent State
ON	Backscattering State
CIR	Channel Impulse Response

Chapter 1

Introduction

Internet of Things (IoT) designates the network that connects physical objects [1]. An IoT device is embedded with sensors and generate an important amount of data that are communicated through the network, for example it can be a smartwatch, a wearable, a security camera, etc. These devices can be of radically different nature to cover applications in various domains such as healthcare monitoring, manufacturing monitoring, wireless sensor networks, smart home, etc. As IoT evolves, new use cases and new applications are developed [2]. IoT is a recent and very promising technology and the associated market is dynamic and growing. The number of IoT devices is continuously increasing and according to studies it is believed to have reached 10 billion in 2018 and it is expected to reach 25 billion by the end of 2021 [3][4] [5][6][7].

The essential feature of an IoT device is the ability to probe some physical or biological quantity and transmit this last to master device in order to analyze the data. Two different families of technologies can be used to achieve these communications: wireless and wired ones. The wired technology has been used extensively for communication, yet it is difficult to implement because it requires deploying cables between the fixed devices and a gateway to the network. Wired technology is therefore limited and expensive, however, it has the advantages of being very secure and reliable. The second category corresponds to wireless technology that is more flexible and for which devices can be deployed more easily and cheaply.

In the IoT context, wireless technology addresses two challenges which are the range of communication and the lifetime of the device. Considering these two key points, new technologies have been proposed: Radio-Frequency Identification (RFID) [8], Long Range WAN (LoRAWAN) [9], Zigbee [10], Bluetooth [11], etc. Each technology provides specific advantages for various applications, for example RFID is very low-power, while LoRaWAN can achieve long-range communications. Depending on the requirement of the applications, different IoT solutions can be envisaged. A recent and promising technology filling the lifetime limitations is the ambient backscatter communication (AmBC) [12]. This technology allows extremely low

power communication, such that devices can be self-powered using energy harvesting of solar light or even radio frequency (RF) waves. Similarly, to RFID technology, the ambient backscatter devices transmit the data in a passive way but also exploit ambient electromagnetic (EM) waves. The breakthrough with other wireless communication technology is that AmBC is “reusing” EM waves from the environment.

More practically, in AmBC, a device named tag modulates the existing RF field coming from an ambient RF source, also called source of opportunity, in the environment like a television (TV) tower [12], a Wi-Fi hotspot [13], a base station, etc. Naturally, the signal radiated by the ambient source is already modulated and meets the standards of the source technology. Nevertheless, the ambient backscatter tag modulates the ambient signal at a slow rate such that the tag modulation, can be considered as variation of the propagation channel by the legacy receiver of the ambient signal and are therefore not impacted by the AmBC tags. However, a receiver dedicated to AmBC, also called reader, is able to detect the information modulated by the tag in the ambient signal. Usually the reader takes benefit of the variation of the amplitude of the backscattered field induced by the tag. More precisely, in the simplest implementation a tag modulates the amplitude of the ambient signal with two different states, in one state the tag reflects the ambient waves in all directions, i.e. the tag backscatters the signal, while in a second state the tag is nearly transparent to the EM signal and has almost no impact on the ambient signal. By electronically switching from one state to another, the tag modulates the backscattered signal according to the message to transmit, resulting in power level variations of the ambient signal at the reader side. From these variations, the reader can decode the signal to recover the message of the tag.

Therefore this breakthrough technology allows devices to communicate information to a reader without emitting additional waves. At a time when people are questioning the effects of the radio EM waves, this recent technique aims at “recycling” EM wave and therefore improving the spectral efficiency of radio signals. It also enables ultra-low power communication for the IoT as the radio emission is one of the most consuming parts of a wireless device. This characteristic is very important in the design of IoT devices, such that they could be deployed without any battery and only powered by energy harvesting.

The research on low power communication technology fits another concern of our actual world, the ecology and the energy consumption and in particular the emission of greenhouse gases. Relatively to this concern, “information technology” counts for 4% of the global emission of greenhouse gases [14], therefore it is essential to develop communication technology that could reduce the global ecological impact.

In the telecommunication domain, new challenges are faced and need to be solved in order to achieve a sustainable world. Considering the actual concerns, AmBC systems can be considered as one step to future communication evolution [15]. As the fifth generation of mobile networks (5G) is currently being deployed and targeting more important throughput, lower latency, and connecting millions or more devices, the next generation may also take into account the

ecological impact of the telecommunications. AmBC technology could be developed and if satisfactory enough promoted to any normalization entity for next generations communications standards.

1.1. BACKGROUND AND MOTIVATION

This promising technology that "reuses" ambient EM waves has also some drawbacks due to the fact that the tag is not emitting any signal. Indeed, in its simplest form, this technology can be subject to strong interference effects that dramatically reduces the communication range and lower the data rate.

In this thesis, we aim to develop a theoretical framework for signal propagation in the context of AmBCs, determine the limitations of such technology, propose improvements to these systems considering latest research advances, and evaluate the performance of the AmBC systems. We specifically investigate the evolution of AmBC considering actual technologies from the field of spatial modulation (SM) [16], of 5G networks [17] and also latest technologies emerging for the sixth generation of mobile networks (6G) [18].

We investigate three different evolutions of the AmBCs to improve the performance of such systems, namely:

- In Chapter 3, we propose to exploit the polarization diversity of the propagation channel to improve the performance and the robustness of AmBC systems. This chapter is partially based on the results obtained in a project devoted to SM in order to increase the data rate thanks to reconfigurable compact antennas.
- In Chapter 4, we investigate the potential of 5G networks to improve the performance and overcome the limitations of AmBC. Indeed as 5G network is largely being deployed it could bring benefits to AmBC, thanks to its new features. More precisely, we focus on multiple-input multiple-output (MIMO) antennas used in the 5G networks to facilitate the detection of ambient backscatter tags and to improve the quality of the backscattered signal. We propose to make the ambient backscattered tags friendly 5G networks.
- In Chapter 5 we investigate reconfigurable intelligent surfaces (RISs), a recent technology currently envisaged for future mobile networks. RISs have the ability to reflect signals in a controlled manner. In the actual use cases, RIS could be deployed in the environment to increase the channel diversity and therefore to enhance the signal quality within a network. We propose to use RISs to assist AmBC systems by improving the link performance between tags and receivers.

For each investigation we propose a method to evaluate the benefits of the proposed system evolution. First, we define a reference system corresponding to current AmBC systems and we determine with measurable data, a performance metric. Based on the reference system, we can

determine the improvement or the deterioration due to the proposed evolutions. The performance of this system is mainly evaluated based on two metrics:

- the achievable data rate: the number of bits that a AmBC tag can transmit per second.
- the range of the communication: it corresponds to the distance where tags can be detected by a reader.

These two metrics are obviously strongly dependent. Consequently, in most of this work, only one metric will be evaluated.

Other parameters exist, such as the energy consumption. In this work, we use conventional diodes or varicap for which the energy efficiency has been already evaluated and shown that they outperform other technologies. Therefore, the consumption aspect that is heavily related to technological progress is not addressed in this work.

In terms of performance, the scenarios can be evaluated based on three different and complementary approaches: theoretical, simulation or experimental. In this thesis, we investigate potential evolutions of AmBC systems from these three perspectives. We propose to establish a theoretical model of the system by considering and justifying different "simple" assumptions. We evaluate, from the theoretical and simulation approaches, the system performance for various configurations. Finally, thanks to experimentation taking into account the complexity of the environment, we validate the theoretical and the simulation results for some specific configurations.

1.2. CONTRIBUTIONS

Our main contributions are articulated as follows:

In Chapter 3 we consider an AmBC system composed of an ambient source, a reader and a tag that is able to change the polarization of its antenna. We propose to improve the ambient backscatter tag by using the reconfigurable antenna technology developed for SM. We introduce a polarization-reconfigurable tag to improve the robustness of the tag-to-reader link against the source-to-reader direct interference. We show that the reconfigurability of the tag antenna can increase the spectral efficiency, similarly to SM. We use this property to improve the robustness of the system.

We compare two coding schemes that exploit polarization diversity. In the first considered coding scheme, the tag, as any standard two-state tag, sends its message by switching between a backscattering state and a "transparent" state. In practice, this is realized by switching the antenna between two different load impedances. With this approach, the tag sends the same message several times, by using each time a different radiation pattern corresponding to a different polarization state. Therefore, it is expected to receive a good quality signal over at least one

polarization state. We introduce a second coding scheme, the data is encoded by switching among different radiation patterns. According to the SM principle each pattern is associated to a sequence of bits. Similar to the first scheme, we expect that an optimized choice of the polarization states will improve the system performance.

To assess the benefits of the proposed tag, we introduce a simple model of the tag that can be studied theoretically and numerically with the aid of an electromagnetic-based simulation software based on the method of moments (MoM). We assess the performance of the system by simulation using this model. Finally, we also experimentally evaluate the proposed implementation by using different antennas, including reconfigurable antennas. This work lead to the publication of two articles [19], [20].

We propose in Chapter 4 to improve the performance of the ambient backscatter system by using 5G massive MIMO (mMIMO) equipment. Ambient backscatter tags in 5G networks could be communicating with base stations or smartphones. We consider two configurations, uplink and downlink 5G transmission, where the ambient source of signal can be either the base station (downlink) or the smartphone (uplink).

First we investigate the downlink configuration and we exploit the mMIMO beamforming feature of the source antenna. We propose to use the beamforming capability of the source antenna to create “hot spots” for tags with very high power and “good reception spots” for readers. We consider two types of good reception spots: a “quiet spot” with very weak source-to-reader interference; and a “coherent spot” with source-to-reader interference, this interference being coherent (i.e. in phase) with the backscattered signal. We developed a multi-step approach consisting of:

- a training phase during which the base station acquires the propagation channel to create the precoding matrix
- a beamforming phase, in which the base station determines the precoding based on the channel estimation and transmits the beamformed broadcast signal that creates the different spots
- a communication phase, in which, finally the tag backscatters the broadcasted signal to the reader.

In the investigation, we compare three different precoders each having a different impact on the backscattering signal. We assess the performance of the system for the three configurations by simulation in a Rayleigh propagation channel. This work lead to the publication of one article [21].

In a second scenario, we investigate the uplink configuration where the mMIMO antenna is used on the reader side to detect the backscattered messages from the tag. We propose to exploit

the channel spatial diversity using an antenna with 64 elements as reader. We experimentally assess an uplink transmission scenario in an anechoic chamber. In a first step, a mobile device, considered as the source, sends pilots to the mMIMO reader. The AmBC tag located between the device and the reader impacts the propagation channel. As the considered tag has two states: a backscattering state and a transparent state, the propagation channel between the device and the reader depends on the tag state. On the reader side, the estimation of the propagation channel is made for the backscattering and the transparent states of the tag. As each state encodes a bit of the tag message, the reader is able to decode the tag message with a better sensitivity thanks to the large number of antennas. We propose to evaluate the performance of the system using a least square error (LSE) estimator to detect the state of the tag. This work lead to the publication of one article [22].

We investigate in Chapter 5, future mobile networks and the emerging technology of RISs. We propose a new practical RIS-assisted AmBC system, to be deployed on an information desk exposing tags for the purpose of reading. In the proposed system, the RIS is used to enhance the transmission between the tags and the reader locations. The benefit of RISs is to allow a partial control of the propagation channel. This property is especially relevant in the case of AmBC where the source cannot be controlled.

We evaluate the passive beamforming capability of the RIS in order to assist AmBC tags. We propose a method where the RIS reflects the signal into the direction of the tag. First, the RIS can pick a beam among a pre-defined codebook of beams. Each beam is designed to reflect waves coming from the exact source location toward one of the pre-defined locations on the desk. Second, the RIS can apply a common phase shift to all its elements. The RIS tests several pairs of beam and common phase shift. Each time, the reader reports a performance quality feedback. The RIS and the reader together search for the beam and common phase-shift pair that maximizes the performance. We expect, with such approach, to improve the bit error rate (BER), with respect to the scenario without RIS, either by creating a “hot spot” on the tag and boosting the backscattered wave, or by creating “coherent spots” both on the tag and the reader, in such a way that all waves reflected by the RIS combine coherently with all other waves, when arriving at the reader to boost the received signal contrast. We propose to validate this approach through experiments. This work lead to the publication of two articles [23], [24].

1.3. THESIS ORGANIZATION

In Chapter 2, we provide an overview of the AmBC system and we present the technologies investigated in the next chapters: the basic features of SM and reconfigurable antennas, we also presents the MIMO technique in 5G network and the RIS technology. We also express the challenges we face when designing an AmBC system. Chapter 3 presents a polarization reconfigurable approach for the ambient backscatter tags. Chapter 4 investigates the mMIMO antenna of 5G networks used as the source and the reader. Chapter 5 presents a new approach considering RISs. Finally, Chapter 6 concludes the thesis and introduces our future perspectives. Figure 1-1 illustrates the thesis organization.

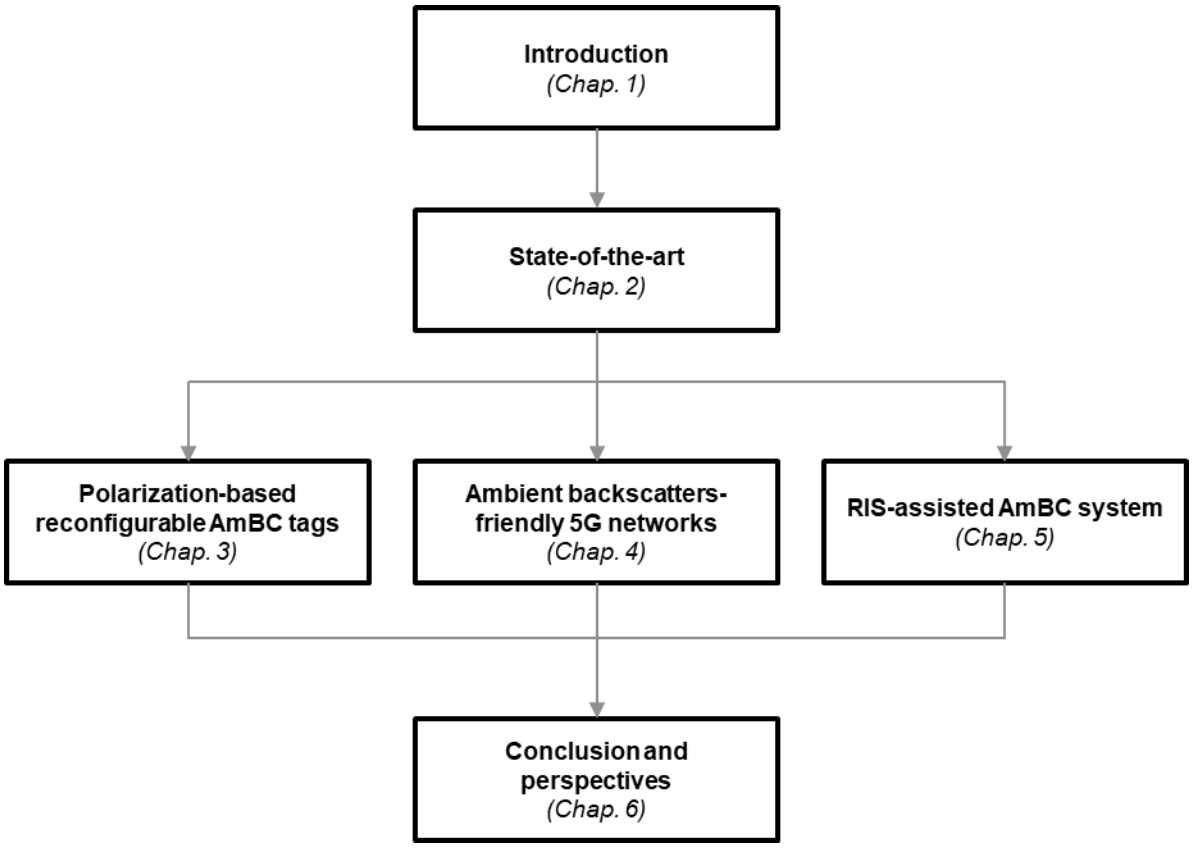

Figure 1-1 Thesis organization.

1.4. LIST OF PUBLICATIONS

Patents

R. Fara, D.-T. Phan-Huy : Procédé de détermination d'au moins un emplacement pour la rétrodiffusion d'un signal ambiant. Submitted as: French Patent (Application No 1906675, application date 20.06.2019).

R. Fara, D.-T. Phan-Huy : Procédé de détermination d'au moins un emplacement pour la réception d'un signal ambiant rétrodiffusé. Submitted as: French Patent (Application No 1907263, application date 01.07.2019).

R. Fara, D.-T. Phan-Huy : Procédé de détermination d'au moins un emplacement pour la réception d'un signal ambiant rétrodiffusé. Submitted as: French Patent (Application No 1907265, application date 01.07.2019).

R. Fara, D.-T. Phan-Huy : Procédé de génération d'au moins une zone pour la rétrodiffusion d'un signal ambiant et /ou pour la réception d'un signal ambiant rétrodiffusé. Submitted as: French Patent (Application No 1908917, application date 02.08.2019).

D.-T. Phan-Huy, R. Fara: Procédé de sélection pour optimiser des communications par rétrodiffusion ambiante, et système associé. Submitted as: French Patent (Application No 1911552, application date 16.10.2019).

Journal

R. Fara, D.-T. Phan-Huy, A. Ourir, Y. Kokar, J.-C. Prévotet, M. Hélard, M. Di Renzo, and J. De Rosny, "Polarization-Based Reconfigurable Tags for Robust Ambient Backscatter Communications," *IEEE Open Journal of the Communications Society*, vol. 1, pp. 1140–1152, 2020,

R. Fara, P. Ratajczak, D.-T. Phan-Huy, A. Ourir, M. Di Renzo, and J. De Rosny, "A Prototype of Reconfigurable Intelligent Surface with Continuous Control of the Reflection Phase," *Submitted to IEEE WCM*, May 2021.

Conference

R. Fara, D.-T. Phan-Huy, and M. Di Renzo, "Ambient backscatters-friendly 5G networks: creating hot spots for tags and good spots for readers," in *2020 IEEE Wireless Communications and Networking Conference (WCNC)*, May 2020, pp. 1–7.

R. Fara, D.-T. Phan-Huy, A. Ourir, M. Di Renzo, and J. de Rosny, "Robust Ambient Backscatter Communications with Polarization Reconfigurable Tags," in *2020 IEEE 31st Annual International Symposium on Personal, Indoor and Mobile Radio Communications*, Aug. 2020, pp. 1–7.

R. Fara, N. Bel-Haj-Maati, D.-T. Phan-Huy, N. Malhouroux, and M. Di Renzo, "First experimental evaluation of ambient backscatter communications with massive MIMO reader," in *2020 IEEE 31st Annual International Symposium on Personal, Indoor and Mobile Radio*

Communications, Aug. 2020, pp. 1–6.

R. Fara, D.-T. Phan-Huy, P. Ratajczak, A. Ourir, M. Di Renzo, and J. de Rosny, "Reconfigurable Intelligent Surface -Assisted Ambient Backscatter Communications -- Experimental Assessment," *IEEE International Conference on Communications Workshop on Reconfigurable Intelligent Surfaces for Future Wireless Communications, 2021,* Apr. 2021

Chapter 2

State-of-the-art

The main objective of this chapter is to present the AmBC and motivate the proposal of the new wireless network techniques presented in the following chapters. We also highlight the challenges one can face in designing an AmBC system. The main contributions of this chapter can be listed as follows:

- Provide definitions and detailed explanations of the backscattering systems,
- Present a general description of the techniques implemented in mobile networks that we developed in our contributions,
- Explain notations, definitions and theorems related to wireless propagation and backscattering principle.

We start by providing the definitions and details on backscatter systems, with a specific overview on AmBCs in Section 2.1. Then we present new wireless network techniques that are used in our contributions, Section 2.2 presents spatial modulation features and similarities with backscattering communications, Section 2.3 gives a general description of 5G and details on MIMO technology, finally Section 2.4 presents promising technology of future 6G networks that could be combined with AmBCs.

2.1. AMBIENT BACKSCATTER COMMUNICATIONS

2.1.1. Backscatter communications

The backscatter communication technology is similar to the heliograph technique that was applied to communicate information by reflecting sunlight before the development of RF technology. The heliograph, illustrated in the Figure 2-1, is a point-to-point reflecting-based communication. On one side an operator controls the reflection of the sunlight by pivoting a

mirror, the transmitter operator generally uses Morse to encode a message. On the other side another operator observe the reflection of the mirror and decode the message. By pivoting the mirror the operator modulates the reflected light, to transmit a message.

Figure 2-1 Heliograph, on the left, composed of a pivoting mirror allowing the transmission of data in Morse code. On the right an operator decoding the message from another heliograph [25].

However, instead of mirrors, backscatter communications take benefit of scatterers, i.e., objects with the ability of scattering the waves. A typical scatterer for an EM wave is made of dielectric or metallic material and its size is smaller or of the order the wavelength. The word backscatter composed of back- and scatter, means, in physics, "*the deflection of radiation or particles through angles greater than 90° to the initial direction of travel*" [26]. The backscattering is the reflection of EM waves in directions opposed to the direction of arrival and is due to waves that meet a scatterer.

Figure 2-2 Illustration of an incident waves (a) transmitted by a source on the left that is scattered in all the directions by an obstacle on the right (b) [27].

Actually rather than the heliograph, the backscattering communication principle is originally based on the RADAR application invented in 1904 [28]. A RADAR transmits an EM wave in a given direction. If an obstacle is located on the wave path, the RADAR detects the part of the incident wave that is reflected back, i.e., backscattered toward it. By processing the time of flight of the signals, the radar is able to determine the distance of the obstacle.

In the same manner, the modulated backscatter communication technique, introduced in 1948 by Stockman, enables communication by backscattering an RF signal [29]. In a backscatter communication system, to transmit information, a backscatter device modulates and backscatters

an RF signal instead of generating a new one as it is done in classical point to point communications. The modulation is generally based on different scattering states in which the device can be configured. These states, correspond to different scattering or absorption strength. This modulated backscatter technique is very well known and is widely used today as it allows low-cost and low-power communications. Technologies such as RFID use this technique extensively [30]. In practice, for the RF waves in the frequency range of 20 kHz to 300 GHz, the loading of an antenna is electronically controlled to tune the antenna scattering, more details on these controllable scattering antennas will be given in the section 2.1.3.

We can separate backscatter technologies into 3 categories, illustrated in Figure 2-3, monostatic backscatter communications (MBC), bistatic backscatter communications (BBC) and AmBCs [31].

A MBC system is composed of a reader and a backscatter device, the reader both generates the RF signal and detects the backscattered signal. The typical example of MBC system is classical RFID technology, where a simple device reads the information encoded by passive devices named tags. This technique is very effective for very short range communications.

In BBC systems, the generation and the detection of the RF signal are performed by two separated devices: the carrier emitter, and the reader, respectively. The carrier emitter location of a BBC system can be optimized to improve the coverage of the system [32][33][34]. BBC systems are also more effective in systems composed of a large number of backscatter devices [35] compared to MBC. However BBC systems are more expensive as they require more complex equipments with a powerful carrier emitter.

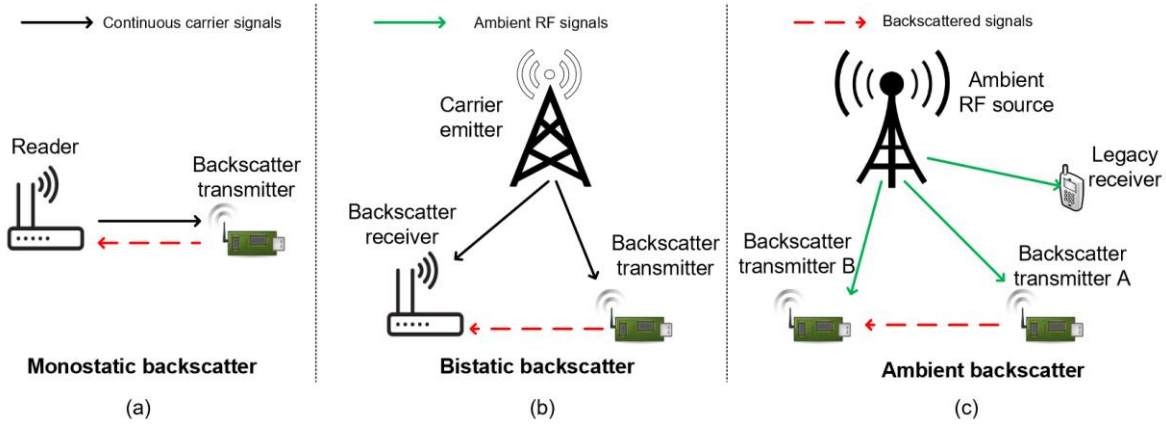

Figure 2-3 Categories of backscatter communication systems [31].

The third category, AmBC, is similar to BBC systems in the way that the RF wave source and the backscatter reader are two separated devices. However, in AmBC the system uses an existing ambient RF source as wave emitter, therefore the incident signal is not a dedicated signal, but it is already modulated and originally addressed to a legacy receiver. For example, signals from a TV broadcast emitter, a Wi-Fi hotspot or a network base station (BS) can be used for AmBCs. These systems have the advantages to be cheaper to deploy compared to BBC systems as RF

sources of signal are already existing in the environment.

2.1.2. Ambient backscatter communications principle

AmBC is a recent promising low-power and low-cost technique enhancing green communications [15][36]. It is based on modulated backscatter technique and uses existing radio-frequency waves in the environment to communicate information. An AmBC system is composed of three equipments:

An ambient radio-frequency **source** (e.g., a TV or radio tower, a Wi-Fi hot-spot, a mobile network base station, a smartphone, etc): the carrier frequency, the bandwidth and the modulation depend on the usage of the source of opportunity. Basically, three families of sources exists. Sources involved in wireless local networks (typically Wi-Fi) and sources used in cellular networks and finally broadcast sources that radiates signal over a large coverage. For example, TV signal can be detected (and backscatter) from several kilometers away.

A backscatter transmitter, also called **tag**, or ambient backscatter transmitter: is a device that backscatters the RF signal generated by the source to communicate information. A tag is composed of a reconfigurable scatterer that can be interpreted as an antenna for which the port connected to a load that is controlled electronically [37], this principle is detailed in the section 2.1.3. Additionally to the modulation of the backscatter signal, the tag requires a coding scheme to encode the data to transmit. Tags in AmBC systems are passive devices, in the way that they do not generate RF signal, therefore tags are very low-power and can harvest energy from the environment to be self-sufficient in terms of energy.

A backscatter receiver, or **reader** is the device that detects the data sent by the tags. The reader is composed of an antenna to receive the ambient signal, and some computation power in order to process the signal, to demodulate and to decode the message according to the coding scheme of the tag. The most important challenge for the reader is to mitigate the interference effects to detect the backscattered signal.

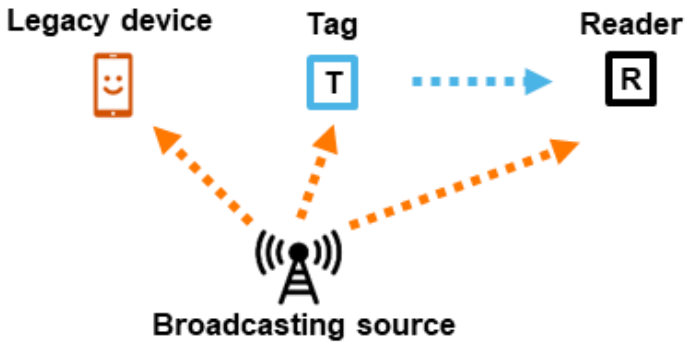

Figure 2-4 Ambient backscatter communication system.

In the literature different kinds of readers have been implemented with different levels of complexity. The simplest reader contains some analogic electronic and detects only the scattering

states of the tag [12], therefore such reader can be very low-power. In the most complex ones, the reader extract the backscattered signal of the tags from the source signal by demodulating the signal from the source [38], or by cancelling interference algorithms [39].

In a backscattering system, as illustrated in the Figure 2-4. the reader receives samples $y[n]$ that is composed of the samples of the direct signal emitted by the source $x[n]$ and the samples of the backscattered signal by the tag, thus we have [12]:

$$y[n] = x[n] + \alpha B[n]x[n] + z[n] \tag{2-1}$$

Where B corresponds to the modulation associated to the bits transmitted by the tag. The complex coefficient α is the complex propagation coefficient of the backscattered signals relative to the ambient signal. In this example the tag has two scattering state, resulting in an on-off keying modulation. This amplitude modulation corresponds to a perfect backscattering state $B = 1$, and to a perfect transparent state $B = 0$ where the tag does not backscatter any signal and is transparent to EM waves.

In this configuration, the reader receives a different level of power depending on the state of the tag, therefore a simple detector can be implemented such as an energy detector.

2.1.3. Antenna and backscattered field

The antenna of the tag is the element that interacts with the EM waves in AmBC system. The scattering theory of antennas has been detailed in 1989 by Hansen [40]. The complex backscattered field $\vec{E}_{scat}$ of the antenna can be expressed theoretically as [41][42] :

$$\vec{E}_{scat}(Z_L) = \vec{E}_{short} + \vec{E}_{ant}(Z_L) \tag{2-2}$$

This backscattered field of an antenna is composed of two terms: $\vec{E}_{short}$ corresponding to the structural mode when the antenna port is shorted and $\vec{E}_{ant}(Z_L)$ the antenna mode that depends on the connected load impedance. The structural mode is independent of the load impedance, however, the antenna mode can be adjusted by selecting different impedance on the port of the antenna.

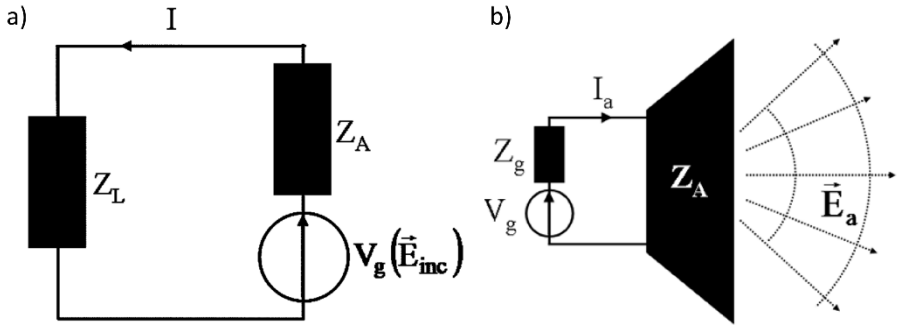

Figure 2-5 a) Equivalent circuit of the tag antenna receiving the ambient signal, b) Transmitting antenna and radiated field. [43].

From an electrical point of view, the antenna with an impedance Z_A backscatters an amount of signal depending on the load impedance connected Z_L, illustrated in the Figure 2-5.a). From a physical point a view the EM waves captured are converted into electrical signal inside the conductive wires of the antenna. The electrical current in the antenna is flowing to the antenna port where the load impedance is connected.

Based on the transmission line theory we can determine the signal reflected by the load that is going to be backscattered. The reflection coefficient Γ at the antenna port is the following:

$$\Gamma = \frac{Z_A - Z_L}{Z_A + Z_L} \ ; \qquad (2\text{-}3)$$

Therefore the signal reflected at the antenna port depends on the connected impedance and the scattered field $\vec{E}_{ant}(Z_L)$ can be determined by applying the superposition theorem [44], we obtain [40][42][43][45] [46]:

$$\vec{E}_{scat}(Z_L) = \vec{E}_{short} - \frac{I_0\big(1 - \Gamma(Z_L)\big)}{2I_a}\vec{E}_a, \qquad (2\text{-}4)$$

Where

- $\vec{E}_{scat}(Z_L)$ is the scattered field when the antenna is loaded by a reference impedance Z_L ;
- I_0 is the current induced by the field $\vec{E}_{inc}$ at the terminals when the antenna is short-circuited;
- $\vec{E}_a$ is the field radiated by the antenna when the current at the terminals is I_a and no external incident wave is applied (Figure 2-5-b)

Table 2-1 Scattered field for various impedance values connected to the antenna.

Z_l	$1 - \Gamma(Z_l)$	$\vec{E}_{scat}(Z_l)$	***Signification***
0	0	$\vec{E}_{short}$	Short-circuited antenna
∞	2	$\vec{E}_{short} - 2\eta\vec{E}_a$	Open-circuited antenna
Z_a	1	$\vec{E}_{short} - \eta\vec{E}_a$	Antenna connected to an impedance

Depending on the load impedance the electromagnetic field backscattered $\vec{E}_{scat}$ can vary from $\vec{E}_{short} - 2\eta\vec{E}_a$ to $\vec{E}_{short}$ with η the constant coefficient of the current ratio.

At the reader the side, a simple non-coherent detector averages and measures the variation of signal to determine the tag state. The contrast amplitude of signal ΔA depends on the impedance of the two states Z_1, Z_2 of the tag.

$$\Delta A = \left| \left| \vec{E}_{scat}(Z_1) \right| - \left| \vec{E}_{scat}(Z_2) \right| \right|, \quad (2\text{-}5)$$

Each state of tag is associated to an impedance, for a two-state tags with Z_1 for the first state and Z_2 for the second we obtain a contrast that depends on each state impedance. The Table 2-2 gives the maximum contrast amplitude for different combinations of impedances:

Table 2-2 Maximum contrast amplitude for different combinations of impedances.

$\boldsymbol{Z_1}$	$\boldsymbol{Z_2}$	$\boldsymbol{max\{\Delta A\}}$
0	∞	$\left\|2\eta\vec{E}_a\right\|$
0	Za^*	$\left\|\eta\vec{E}_a\right\|$
Za^*	∞	$\left\|\eta\vec{E}_a\right\|$

Previous works, [40][43][45] have demonstrated that the optimal choice for the two sates of the tag is the short-circuit and the open circuit state. The result has practical benefits, as it is simple to make tags with these two impedances. With an RF switch, we can approximate by open circuiting or short-circuiting the antenna port, the two optimal values of impedance: $Z_1 = 0$ and $Z_2 = \infty$.

The antenna characteristics (size, substrate, etc.) can be tuned to resonate at the frequency of the corresponding ambient signal. In its simplest implementation, the antenna corresponds to a dipole antenna. In general, a half-wavelength dipole antenna is used in AmBC, it consists of two branches of conductive wires, one quarter of a lambda wavelength each.

2.1.4. Coding scheme

In section 2.1.1, we have seen that the signal received by the reader is the combination of the backscattered signal and the forward signal. Due to the propagation, these signal may combine constructively or destructively, depending on the location of the elements [47] [48]. This can be an important weakness for these systems if it is not handled, the combination of the signals in the presence of the tag, in a backscattering state, does not always correspond to an increase of the signal power. Due to the “constructive” or the “destructive” combination of the backscattered signal with the ambient signal at the reader, the backscattering state of the tag can be either increasing or decreasing the signal level.

Additionally, in the literature, most of the considered readers are using an energy detector for which the detection is based on the level of signal. To mitigate the detection problem, a differential coding is applied on the data sent by the tag to facilitate the detection by the reader.

Different coding schemes have been used such as Manchester coding [49], FM0 or Miller [50]. These coding schemes require twice the bits than original data, yet it ensures reliability on the decoding side.

In FM0 coding scheme, each logic bit is associated to two sequences of 2 bits [50] that corresponds to a FM0 symbol. The FM0 encoding has a memory effect that is why the logic data can be encoded with one of the two symbols associated. The FM0 coding scheme follows two rules, illustrated in the Figure 2-6:

1. The phase of the signal is inverted at the boundary of each symbol.
2. The logic data "0" is represented with an inversion of the phase signal at the mid of the symbol.

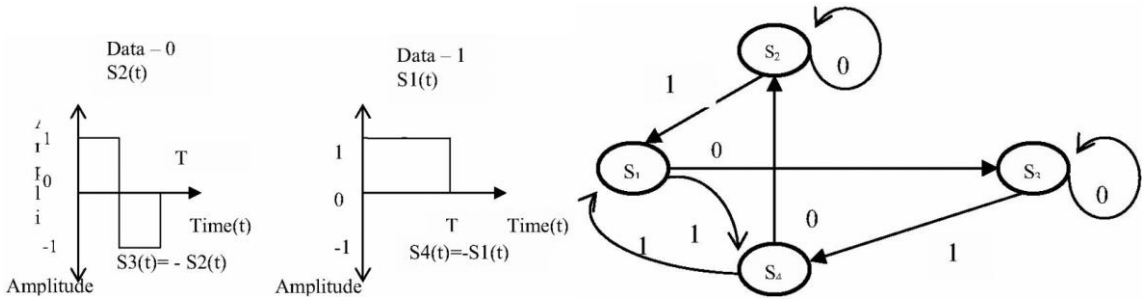

Figure 2-6 FM0 coding scheme, FM0 sequence of logic bits representation and state diagram of the FM0 encoding scheme [50].

For the Miller coding scheme, illustrated in the Figure 2-7, the coding scheme has similar rules:

1. The phase of the signal is inverted at the boundary of the logic data "0"
2. The logic data "1" is represented with an inversion of the phase signal at the mid of the symbol.

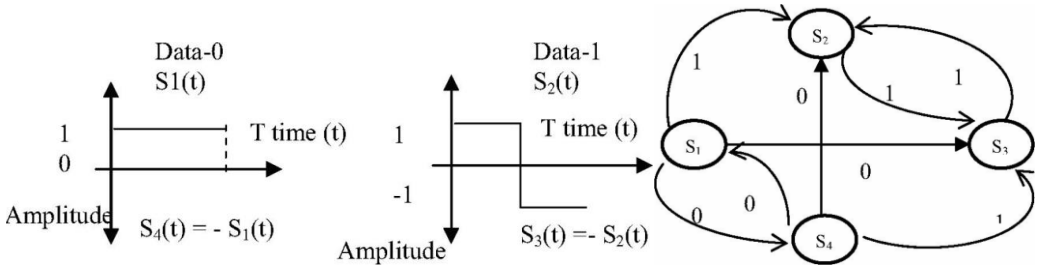

Figure 2-7 Miller coding scheme, Miller sequence of logic bits representation and state diagram of the Miller encoding scheme [50].

These schemes are widely used in backscatter communication field [8] and also for AmBC [12][51], some new schemes have been proposed but they are very similar to the existing solutions and does not provide significant improvement [52].

2.1.5. Energy harvesting

In wireless communications for IoT, usually the radio part is the most consuming part of the connected device. In wireless sensor networks for example, a lot of sensors are deployed to monitor an area, a building, etc. Only few bits are required to be transmitted by each sensor, the

sensing processing part of the node is well optimized for low power consumption, however, the radio transmission consumption can attain more than fifty percent of the total consumption [53]. In this way, the backscattering technic is promising, as it does not use active radio transmission the power consumption is very low.

As the AmBC devices require a small amount of energy to communicate data, the required energy to power-up the tags can be harvested from the environment [54]. In the environment different types of energy can be harvested, from vibration or movement, kinetic or piezoelectric. Energy can also be harvested from electromagnetic waves, by using a solar panel to harvest solar energy [55] or a rectenna to harvest radio electromagnetic wave energy [12][56]. Different techniques can be used to collect energy in order to make the tags self-powered and self-sufficient in energy.

A rectenna is designed to harvest energy from the radio electromagnetic waves, however, usually this technic harvests a very small amount of energy and usually it is not enough to power the entire device. For other applications with active radio transmission, the radio electromagnetic wave energy can be used to power the transmitting device when the system is designed for that purpose, for example in RFID, NFC or in wireless power transfer systems [57].

2.1.6. Detection scheme

In AmBC, different schemes have been used to detect backscatter transmitters. We distinguish them into two categories: coherent and non-coherent detector.

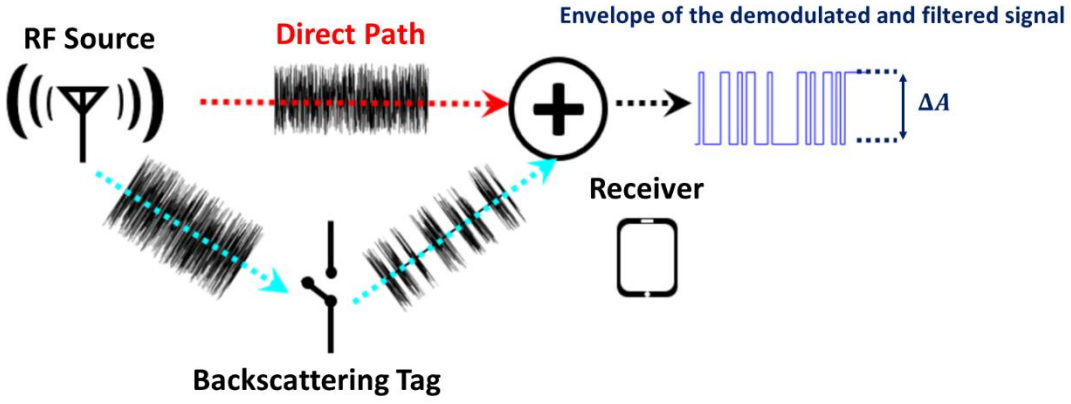

Figure 2-8 AmBC non-coherent detector principle [58].

The non-coherent detectors do not decode the original transmitted symbols. They are very simple and easy to implement, however, they are not very robust to perturbations and do not perform at high rates. For example, a non-coherent energy detector consists in averaging the ambient signal to obtain a value of the signal level of the modulated ambient signal and removing the variations inherent to the ambient signal. Depending on the tag state, the level of the ambient signal changes and the reader can detect the state and decode the message, as illustrated in the

Figure 2-8 [29][59][60] [58].

The performance of such energy detector relies on the variation of the power level between the two states. Therefore it has been demonstrated in [43] that the BER can be expressed as:

$$\mathrm{BER} = \frac{1}{2}\mathrm{erfc}\left(\frac{\Delta A}{\xi}\right), \qquad (2\text{-}6)$$

where ξ is the modulation noise, ΔA is contrast amplitude of signal at the reader.

More states can be used at the tag side in order to improve the data rate, hence the reader will need a better sensitivity to detect the different states and the ambient signal must be stable enough.

Table 2-3 Performance metric for the coherent and non-coherent detectors.

EM field at the reader for a transparent tag	$\vec{E}_r^{OFF}$	
EM field at the reader for a backscattering tag	$\vec{E}_r^{ON}$	
Performance metric	Non coherent	Coherent
	$\Delta A = \left\|\left\|\vec{E}_r^{ON}\right\| - \left\|\vec{E}_r^{OFF}\right\|\right\|$	$\Delta A = \left\|\vec{E}_r^{ON} - \vec{E}_r^{OFF}\right\|$

The coherent detectors, on the other hand, are more complex and require more powerful circuit to be implemented. The coherent detector extracts from the received signal the transmitted symbols by the source and the signal from the tag. The coherent detector requires a prior knowledge of the channel that can be obtain thanks pilot estimation. The performance with such detector is higher compared to non-coherent detector, it is also more robust to environment perturbations [38][61]. The coherent detectors performance depends on the difference of signal at the reader side and the scheme used.

2.1.7. Limitations

Traditional backscatter communication systems like RFID have some limitations. First, it requires that the backscatter transmitter must be placed near their RF source, thereby limiting the coverage area for tags. Second, the RFID reader requires to send RF signal to detect the surrounding tags, thereby it spends a lot of energy by transmitting EM signal.

On the other hand, the AmBC systems mainly suffer from the interference. The ambient signal that is backscattered by the tags is not dedicated to this usage, therefore it is not optimally designed for that purpose. The interference is inherent to AmBC, the principle being based on reusing existing waves, the reader (dedicated to detect ambient backscatter tags) receives at the same time the ambient signal coming directly from the source and the backscattered signal coming from the tag. Due to this principle, ambient backscatter suffers from interference even in line-of-sight (LoS) [48]. In [47] it is shown, by using simulation and experiments, that even in

LoS, the signal contrast experiences deep fades when the tag is located on ellipses that have the source and the reader as foci. These ellipses are regularly spaced by half a wavelength that we observe in the Figure 2-9 showing the experimental of BER depending on the tag location, the source and the reader being fixed

The main challenge for the ambient backscatter system is that the performance is highly dependent on the location of the tag.

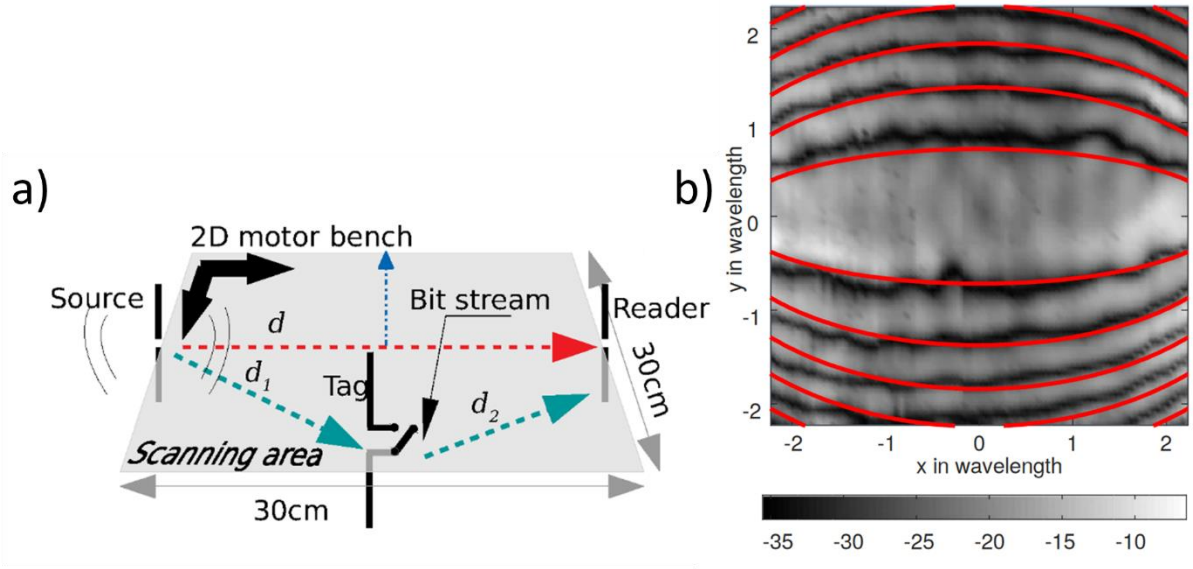

Figure 2-9 (a) Setup of the experiment realized in [47] (b) Map of the BER performance as function of the tag location.

Therefore to develop and improve such AmBC systems, it is required to:

- Improve the signal quality on the tag, by improving the amount of signal power level at the tag, therefore the backscatter signal power will increase.
- Reduce the interference between the ambient signal and the backscattered signal at the reader location.

In the thesis, we aim at proposing and developing improvements to AmBC systems to overcome these limitations, and in the next section, we provide an overview of the basics of the technologies that are studied in the next chapters.

2.2. FROM SPATIAL MODULATION TO AMBIENT BACKSCATTER COMMUNICATIONS

The first technology studied is a recent technology named spatial modulation [16] that has similarities with AmBC, it also exploits the channel propagation to transmit data and improve spectral efficiency. Thanks to similarities it is expected that some techniques applied to this technology could be transposed to AmBC systems.

2.2.1. Principle of spatial modulation

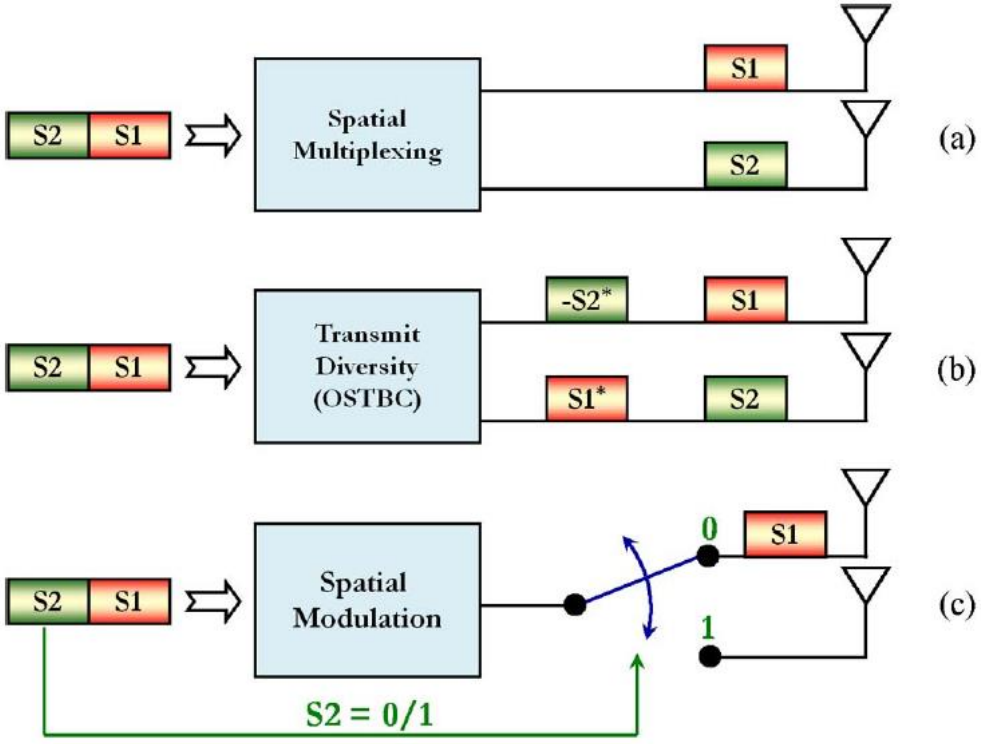

Figure 2-10 Illustration of three MIMO concepts: (a) spatial multiplexing, (b) transmit diversity and (c) SM [62].

Spatial modulation is technique used in a MIMO system to transmit data while exploiting the channel propagation. In a MIMO wireless system, the transmitter is composed of multiple antennas that are used to spatially multiplex the signal or to exploit the channel diversity as illustrated in the Figure 2-10 a), b). The transmitter uses precoding matrix to optimize the signal to transmit on each antenna and multiplex the transmissions. In that case each antenna of a MIMO system requires to be connected to an RF chain that is generating and amplifying the signal to be radiated by the antenna. However, this system is very complex, it requires a lot of processing power and one energy-consuming RF chain per antenna.

In SM, the principle is to improve the data rate by increasing the number of antennas and keeping only one RF chain. The transmitter also exploits the channel diversity but it modulates the transmitted signal by selecting one transmitting antenna among the multiple antennas, as illustrated in the Figure 2-10-c) [62][63][64].

More precisely, in SM one RF chain is used for multiple antennas and by using a switch, the transmitter can successively connect one antenna to the RF chain. The signal is radiated by the selected antenna and on the reader side, thanks to signal processing, the reader is able to detect

which antenna of the transmitter has been used. This principle exploits advantageously the complex propagation channel: the more complex the propagation channel, the more the channels between each transmitter antenna and the receiver are uncorrelated and the easier it is for the receiver to distinguish the "signature" of the transmitting antenna.

In SM communication, during a first step the transmitter sends pilots to allow the reader to estimate the channel. The channel estimation is done for each antenna of the transmitter and the receiver store the channel estimations of each transmitter antenna. A binary sequence is associated to each antenna of the transmitter, corresponding to the spatially modulated data. For each regular symbol transmission, the transmitter selects the antenna to be connected to the RF chain resulting in the transmission of the conventional symbol and the spatially modulated data.

This method improves the spectral efficiency by transmitting more bits without requiring additional RF chains [65]. An RF chain compared to a single antenna is complex and expensive, it is made of powerful electronics compared to an antenna that is very simple and cheap to produce, mainly composed of conductive material and substrate. Therefore, spatial modulation compared to MIMO is much easier and cheaper to implement.

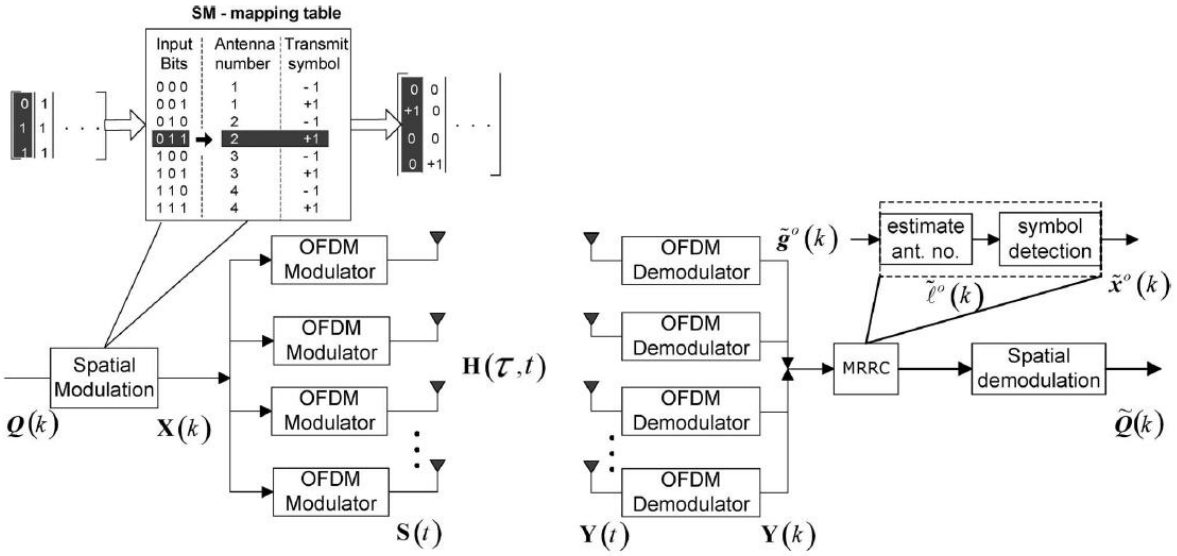

Figure 2-11 Spatial Modulation - Orthogonal Frequency Division Multiplexing (OFDM) system [16].

An example of a spatial modulation system is illustrated in the Figure 2-11 based on [16], the transmitter and the receiver are composed of N_t and N_r antennas. For a given constellation diagram used to encode conventional data with M_c constellation points, the number of bits transmitted per sample with the conventional modulation is $\log_2(M_c)$. With spatial modulation the transmitter and the reader share a mapping table that associates a bit sequence to the active antenna. As the reader uses a complex detection algorithm like LSE or maximum likelihood, it is able to determine the active transmitter antenna and decode the spatially modulated bits. The total number of transmitted bits for SM-MIMO is then $\log_2(N_t) + \log_2(M_c)$ [16][66].

In this example the performance of the spatial modulation has been compared with other configurations: Alamouti and V-BLAST schemes [67]. The performance of the configurations, using $N_t \times N_r$ antennas, is illustrated on the Figure 2-12 and show that the SM technique outperforms the other considered schemes. For the same spectral efficiency between the different schemes, the BER of the different schemes is approximatively the same at low signal-to-noise ratio (SNR), yet for high SNR the BER of the SM is lower than the other schemes.

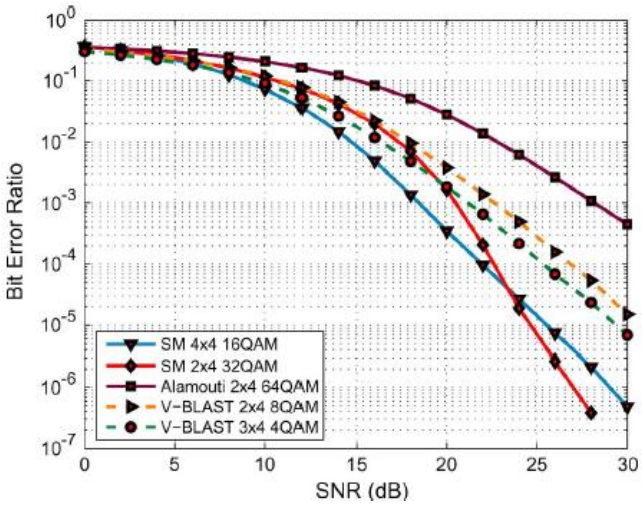

Figure 2-12 BER versus SNR for 6 bits/s/Hz transmission [16].

We also notice that SM allows to use less complex constellations to achieve the same rate. In [68], it has also been demonstrated that for the same data rate spatial modulation uses a less complex constellations and is therefore more robust than an equivalent more complex constellation.

Spatial modulation technique is a very interesting possibility to improve the spectral efficiency. Hence, even if only one RF chain is required the number of antennas is significant and is not compact enough to be implemented in IoT devices, therefore new type of antennas, detailed in section 2.2.2 have been developed to achieve SM in a compact manner.

2.2.2. Reconfigurable antenna

In spatial modulation the transmitter exploits the channel diversity by transmitting the signal from one of its antennas. This requires that the transmitter is equipped with multiple antennas connected successively to the RF chains with a switch controlling the transmitting antenna. To achieve spatial modulation, the transmitter requires multiple antennas and the more antennas the higher the data rate. In IoT applications, the goal is the same: to improve the data rate without improving the energy consumption considerably, therefore SM can be a good solution to improve the performance. The main drawback of the SM for IoT systems is the compactness, in order to have sufficient channel diversity and to correctly detect the active transmitting antenna the spacing between the transmitter antennas must be higher than half of the wavelength, to have

uncorrelated enough patterns. For small IoT objects, even at high frequency the spacing can be difficult to obtain and the IoT devices will loose in compactness.

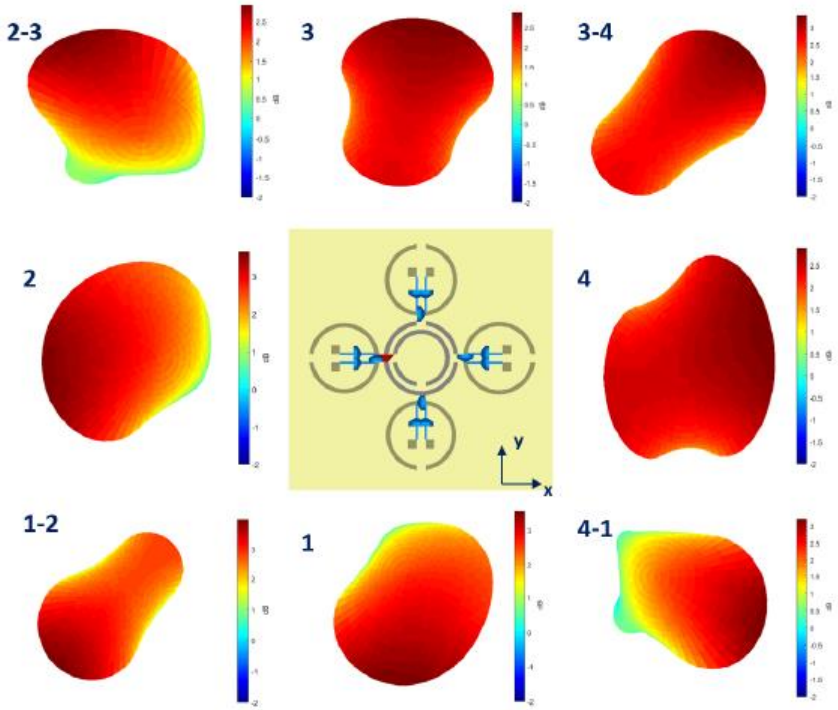

Fig. 7: *8 Radiation Patterns in gain at 2.45 GHz at 2.45 GHz*

Figure 2-13 Radiation patterns of a reconfigurable antenna [69].

To overcome this problem, reconfigurable antennas have been introduced for SM in [62]. This method uses only one antenna usually larger than a regular antenna but this antenna can be reconfigured in order to modify the radiation pattern. If the different radiation patterns are uncorrelated enough, the reader may be able to distinguish each of them [70]. The large number of antenna on the transmitter side can be replaced with a single reconfigurable antenna with uncorrelated radiation patterns. An example of reconfigurable antenna from [69] is illustrated in the Figure 2-13 that shows the antenna and the different radiation patterns.

Practically, the reconfigurable antenna is designed to radiate at a specify frequency. The modification of the radiation pattern is obtained by creating resonance and changing the circulation of the current on radiating conductive part of the antenna. Electronic components such as diodes or switches can be used create short or open circuit on the conductive areas.

The combination of the SM technique and reconfigurable antenna has been experimentally validated in [68] where an IoT device uses a compact reconfigurable antenna to transmit data with spatial modulation, which is improving the data rate while keeping the device compact. In this example the compact reconfigurable antenna achieves eight different states while using four positive intrinsic negative (PIN) diodes [69].

2.2.3. From active transmission to passive backscattering communication

In SM, the transmitter successively changes the radiating antenna, either by choosing one of the multiple antennas to transmit the signal or by changing the radiation pattern of a reconfigurable antenna. The transmitter exploits the channel diversity that allows the detection of the transmitting antenna at the reader side based on the channel estimation. On the receiver side, thanks to signal processing, the data associated to the radiating antenna are decoded and the spatially modulated bits can be recovered.

This technology, combined with reconfigurable antennas, is then very interesting for IoT devices as it allows a high data rate without increasing the power consumption. Recently, research has been further, in [71], it has been demonstrated that the receiver is able to detect the change of state of the reconfigurable antenna without transmitting any RF signal with the reconfigurable antenna. In the same manner as AmBC, if the SM transmitter is not transmitting RF signal, but illuminated by an ambient signal the receiver can detect the variation of signal while the reconfigurable antenna is being reconfigured. Therefore AmBCs have been successfully achieved with a reconfigurable antenna designed for spatial modulation [71][72].

This technique requires a coherent detector on the reader side in order to detect the state of the reconfigurable antenna. A reconfigurable antenna with a large number of reconfigurable states can enhance AmBC by increasing the data rate of the passive transmitter.

Therefore, this technology from spatial modulation can be used at the tag side of AmBC system to improve the performance. Yet, it requires that the reader use multiple antennas to exploit channel diversity. Thankfully MIMO systems are being deployed with the fifth generation of mobile networks. Indeed, one of the key features of the 5G is the mMIMO that is currently being deployed. Massive MIMO is also an interesting technology that could improve the performance of AmBC systems independently to the reconfigurable antennas.

2.3. AMBIENT BACKSCATTER COMMUNICATIONS IN A 5G NETWORKS

2.3.1. 5G network features

The 5G network has started being deployed in 2019 and the 5G network is still growing around the world. The development of 5G has been guided to ensure three key points, illustrated in the Figure 2-14:

- The capacity enhancement: more user equipments (UEs) can be connected to the network with more throughput,
- The reliability and the latency, for critical applications, like industrial and vehicular automation,

- The massive machine type communications, mainly to provide connectivity to IoT devices.

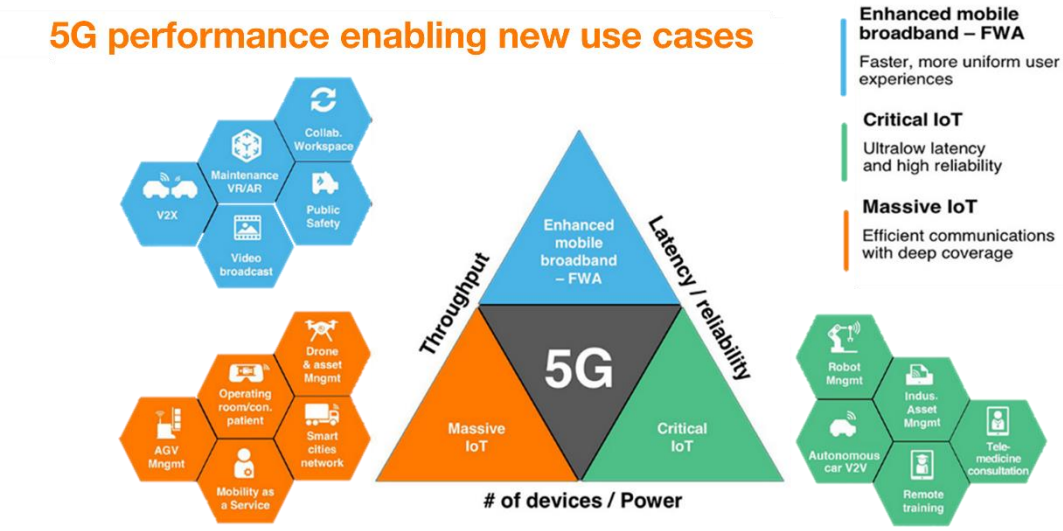

Figure 2-14 5G features [73].

To ensure these key points the 5G network relies on new features [74][75]: new spectrum in the 3.4-3.8GHz band for the first development phase, new low-density parity-check channel coding (LDPC) [76], and new equipments like mMIMO [17]. All these technical aspects of the 5G are studied and evaluated in 3rd Generation Partnership Project (3GPP) meeting, it results in specifications release, based on the meeting discussions, to determine the characteristics of the 5G equipment.

One of the major innovations introduced in the 5G networks is the MIMO technology. A MIMO system is using multiple antennas on the transmitter and on the receiver side of a mobile communication to improve the performance and the robustness of the network [77].

MIMO technique is a technological breakthrough, thanks to the large number of elements the signal quality can be improved. The performance enhancement relies on three main features: spatial diversity, spatial multiplexing and beamforming capability.

- Spatial diversity encoding: a single stream is transmitted on each of the antenna and a coding scheme exploits the independent fading in the multiple antenna links ,
- Spatial Multiplexing: the signal is splitted in multiple streams to serve different users at the same time. The different channels must be uncorrelated,
- Beamforming: the array of antennas is used to orientate and to control the beam or the radio waves.

In previous mobile generation the number of antenna elements was limited, a maximum of eight has been experimentally tested in 4G [78]. With the new generation of mMIMO antenna,

tens of radiating elements are allowed to be deployed per base station. Massive MIMO is the evolution of MIMO system with a very high number of antenna elements on the base station side, larger than the number of users in the cell [79][80]. In MIMO, each radiating element is connected to an RF chain with a power amplifier, meaning that the radiated signal is independently controlled for each of the elements.

Massive MIMO technology has shown very important improvement, yet implementation of mMIMO is possible only in base stations that can be equipped with a large number of antennas without any compactness or power consumption problematics. It is much more complicated to integrate MIMO antennas in UEs due to their limited size.

For the second deployment phase of the 5G network, the frequency of the dedicated spectrum is higher around 26 GHz corresponding to millimeter wavelengths (mmWave). In that frequency band the small wavelength makes the integration of multiple antennas in a mobile facilitated. In that case MIMO technology can be enhanced, with a larger number of elements on the UE side.

The multiplexing increases performance with the number of transmitting or receiving antennas. Massive MIMO thanks to its large number of antennas performs better and its capabilities are improved.

Practically, in a MIMO system the UE can send pilots signal in order to estimate the channel at the BS side. By considering channel reciprocity, the estimation is used for the uplink and the downlink channel. Therefore when the BS transmits data, it uses the estimation of the channel to create the precoding matrix. In that case the BS can optimize the signal on each of the antenna element to enhance the performance of the communication [81]. This relies on the condition that the channel is stable enough during a sufficient time interval named coherence time longer than the estimation and the transmission time. For a large number of antennas the channel at the BS side can be considered stable for a long time interval thanks to channel hardening [82][83][84].

2.3.2. MIMO antenna for AmBC systems

The MIMO technique has been studied for backscattering systems like RFID to enhance the system performance. It has been demonstrated experimentally [85] and by simulation [86] that MIMO improves the bit rate and the range of the RFID communications. The Figure 2-15 illustrates the improvement brought by a MIMO system, where M, L, N is the number of source, tag and reader antennas, respectively.

Thanks to the spatial diversity the signal detection from the RFID devices can be improved.

In AmBC systems, MIMO technology has been used to improve the signal quality and the detection of the tags. Multiple antennas can be implemented on each element of the AmBC system. A MIMO source can use the spatial multiplexing and the beamforming features to improve the ambient signal quality. A multi-antenna tag can also be better detected, as the backscattering tags are passive they are difficult to detect, hence multi-antenna tags can exploit

channel diversity to be better detected [87]. A multi-antenna reader can also be used to improve the detection of the AmBC tags [88][89].

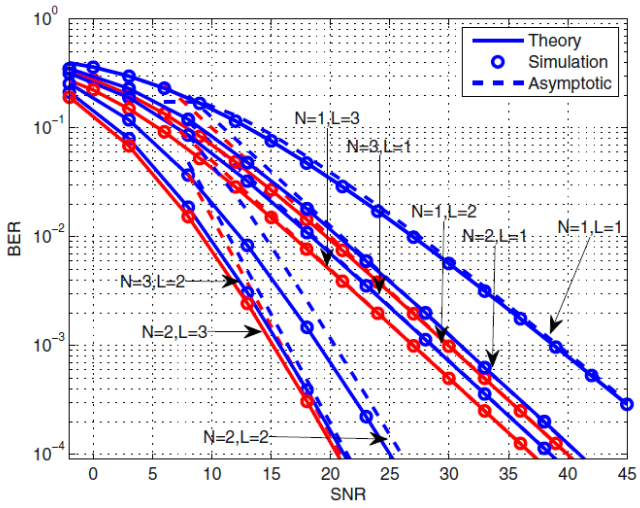

Figure 2-15 BER performances of a MIMO RFID system using M=1 source antennas, L tag antennas and N receiver antennas [86].

Considering the 5G signal as ambient signal for AmBC, the BS and UE can be considered in two different scenarios as the source of signal depending on the type of 5G transmission: uplink or downlink. For the downlink scenario, the tags can backscatter the signal from the BS to transmit data to the UE, in this case the source of signal, the BS, is equipped with mMIMO antenna. For the uplink scenario the tag can backscatter the signal emitted by the UE to transmit data to the BS, in this scenario the reader (BS) is equipped with mMIMO antenna.

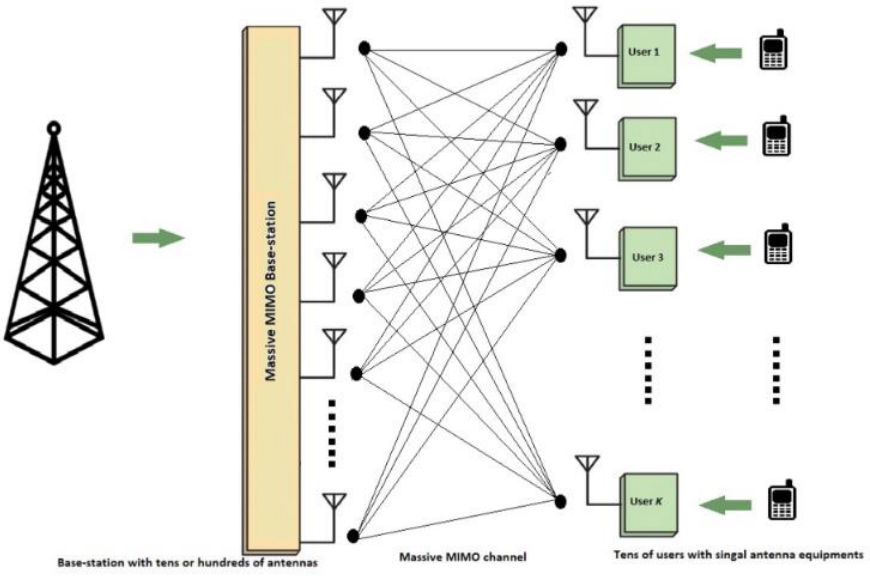

Figure 2-16 Wireless system composed of a mMIMO with a large number of antennas on the BS side and K users to serve.

In each scenario, the BS equipped with mMIMO antenna has better capabilities than classical

MIMO AmBC systems studied previously, the BS can either be considered as the source to assist the tag with the emission of a very good quality signal on the tag or considered as the reader to detect the tag with a better diversity.

2.3.3. Downlink configuration

We first consider a system with an ambient source equipped with multiple antenna elements, corresponding to the downlink scenario in 5G. Therefore, in this subsection, we analyze the principles and the features of a transmitting equipment with multiple antenna elements toward a UE receiving the signal with one antenna, as illustrated in Figure 2-16 considering a downlink configuration. We present the precoding and beamforming capabilities of such multiple antenna elements transmitter.

In this downlink example, the system is composed of a BS equipped with M antenna elements and each element can be controlled independently. The channel between the transmitting BS and the receiver R equipped with one antenna is denoted $\mathbf{H} \in \mathbb{R}^{1\times M}$, we have the received symbol $y \in \mathbb{R}$ at the receiver antenna defined by:

$$y = \mathbf{H}\mathbf{x} + n, \tag{2-7}$$

where $\mathbf{x} \in \mathbb{R}^{M\times 1}$ is the symbol transmitted and n the noise vector.

The precoding technique can be used to increase the SNR at the receiver side. The precoding consists in multiplying the symbol to transmit by a precoding matrix P to improve the signal quality at the receiver side by exploiting the spatial diversity.

Therefore, the vector x becomes:

$$\mathbf{x} = \mathbf{P}s, \tag{2-8}$$

where s is the normalized data symbol and P is the linear precoding vector.

Different kinds of precoding can be used with different purposes, for example the maximum ratio transmission (MRT) aims to maximize the signal power at the receiver side [90][91]. The Zero Forcing (ZF) is another kind of precoder for multi-user, the ZF precoder aims to transmit multi-stream at the same time without interference at each user [92].

For example, in the MRT case and for the previously given channel $\mathbf{H}$, the precoding vector is $\mathbf{P} = a\mathbf{H}^H$, where a is the normalization factor and $(\cdot)^H$ the Hermitian function. At the receiver side, it is received after simplification $y = as$ [91].

Generally, the precoding technique requires a prior knowledge of the channel state information (CSI) that can be obtained from channel estimation based on pilots. This channel knowledge is used at the source side to create the matrix $\mathbf{P}$. In wireless networks, the precoding technique

enables to maximize the signal power at the receiver output.

However, if the channel state information is not known at the transmitter side, the signal power at the receiver can be improved by beamforming the transmitted signal. The transmitter can transmit signal in specific directions by creating a directive beam. The beamforming is a spatial filtering obtained for a transmitter with multiple antennas. This technique improve the directivity of the global antenna the more antennas the more the signal is directed and the beam is narrow. The transmitter can successively steer the beam into different directions to make sure that wherever the receiver is, it will receive a stronger signal. For the beamforming feature, the transmitter needs to apply specific phase shift coefficients depending on the location of the transmitting antennas [93][94]. The precoding vector can be calculated with a phase-shifting law for a given direction to target.

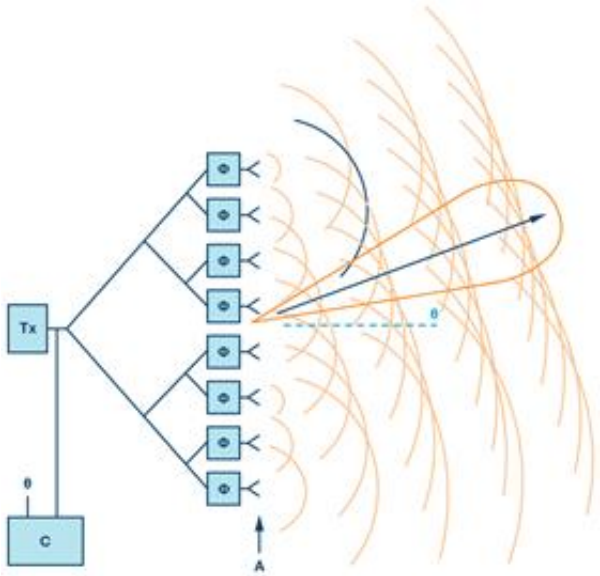

Figure 2-17 Beamforming principle with a multi-antenna base station [94].

2.3.4. Uplink configuration

In a second scenario, the tag can use as ambient signal the signal emitted by a UE (transmitter) intended to a BS (receiver), corresponding to an uplink transmission. In that case the transmitter is equipped with one antenna while the receiver is equipped with multiple antenna elements.

In that case the receiver has an important sensitivity and is capable of detecting small changes in the channel, a mMIMO receiver has an important diversity gain [95]. Additionally, a base station has an important processing power that permits to implement complicated detection scheme. A mMIMO BS is therefore able to process the received signal, perform channel estimation and apply algorithms such as a LSE detector [96], a minimum mean square error (MMSE) detector [97] or a maximum likelihood detector.

For example, in the least square detector, the principle is to globally minimize the error. In a

first step the channel is estimated by the receiver while the transmitter sends pilots, the receiver stores the estimator for the next detection step. For the detection phase the receiver globally compares the received signals $\mathbf{y} \in \mathbb{R}^{N\times 1}$ to the ones received during the estimation phase $\bar{\mathbf{y}}$ and minimize the error to determine the estimated symbol $\hat{s}$, the detector perform:

$$\{\hat{s}\} = \arg\ \min\{\|\bar{\mathbf{y}} - \mathbf{y}\|^2\}, \tag{2-9}$$

It has been demonstrated for different algorithm schemes that the performance of the detection increase with the number of antennas at the receiver side [80]. Thanks to the number of antennas, the global estimation is more precise and the minimization of the error is reduced.

In AmBC system using multiple antennas at the reader side, allows the reader to reduce interference from the ambient signal, hence provide higher bit rates. More precisely, in [89], a non-coherent detector decodes without phase information the backscattered signal by performing matrix inversion on a digital representation of the received signal. The multi-antenna receiving detection, illustrated in Figure 2-18, is designed for a low-power reader and show significant improvement. Therefore, with a more powerful reader like a multi-antenna BS more complex schemes can be implemented that should additionally improve the performance of the detection.

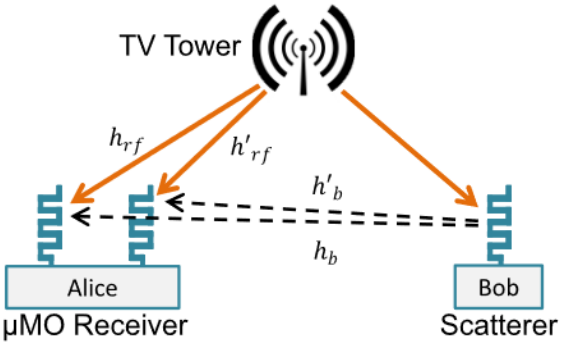

Figure 2-18 Multiple antenna reader designed for AmBC [89].

We have seen that by considering 5G networks and the mMIMO deployed equipments, the performance of the AmBC can potentially be improved. In the next section we will see that the AmBC systems can also take advantages of the next generation of mobile networks thanks to a new RIS technology.

2.4. 6G FUTURE MOBILE NETWORKS

The deployment of 5G enables a lot of new possibilities and new applications thanks to the large capacity or the low latency. At the same time, new research challenges have emerged and new requirements have been identified for 6G. New technologies have been proposed to face them for this new generation, in the continuity with the previous generations, the capacity and the latency of the network should be improved. One of the new challenge to face is to control the channel within the network, the propagation channel separating the transmitters and receivers has

inherently been perceived as not controllable, yet the network performance is highly dependent on the quality of this propagation channel. The control of the channel allows to boost the quality of the signal to the intended user while limiting the electromagnetic field exposure of the non-intended users [18]. Recently, RISs has shown a significant interest as it enables to partially control the propagation of the EM waves [98][99][100].

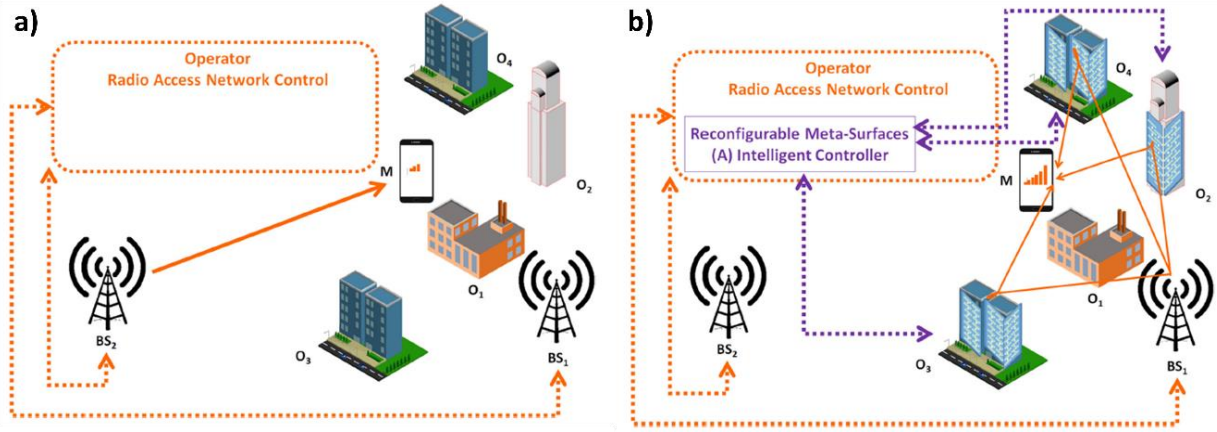

Figure 2-19 a) Current operation of wireless networks: communications, b) Smart radio environments: communications [98].

An RIS is an electronically controlled surface composed of passive reflecting cells, which can reflect RF waves. Deployed in a wireless network, RISs allow operators to improve the efficiency and the coverage of their network, without requiring any network densification [101]. For example, as illustrated in the Figure 2-19 a), within a current deployed network if the link between the base station BS_1 and the mobile M is blocked by an object O_1, the mobile is served by BS_2. Yet, the signal received by M is not strong enough for high-data rate transmission due to the large distance between BS_2 and M

In a smart network, as shown in Figure 2-19.b), the RISs can be largely deployed on buildings to improve the reflection and the control of the propagation environment. RISs on buildings can reflect the signal to avoid blockage and improve the signal at the receiver. In this scenario the channel propagation can be partially control to be considered as a "smart radio environment" [98][102].

2.4.1. RIS model

A RIS is composed of a large number of cells, the cells are mainly passive: the incident signal is scattered by the cell without amplification of the EM signal. The RIS does not require any power amplifiers, some energy is used to power the smart controller that tune the RIS. Each cell can modify the signal and depending on its design, the phase-shift, the amplitude or even the polarization of the incident signal can be tuned [103].

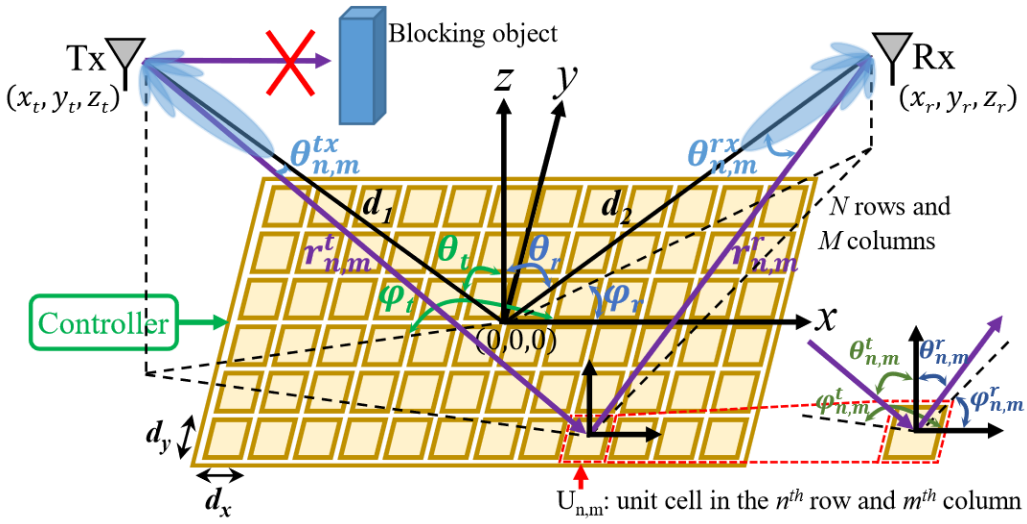

Figure 2-20 RIS-assisted wireless communication with a blockage between the transmitter and the receiver [103].

Different experimental prototypes have been proposed in the literature, in [104], a transparent RIS is presented with three modes: full penetration of incident RF waves, partial reflection of incident RF waves and full reflection of all RF waves. In [105], a large RIS is presented where each cell can be controlled to reflect or not the incident signal. Depending on the design the RIS features are different and the model should be different, to go further in details about RIS models we focus on an example [106], illustrated in the Figure 2-20. In this example, the wireless communication between a transmitter (Tx) and a receiver (Rx) is considered where the line-of-sight path is blocked by an obstacle. Each cell of the RIS is identical, hence the electric field at the receiver corresponds to the superposition of the electric field reflected by all unit cells toward the receiver. For an RIS of N rows by M columns of elementary cell, the signal power at the receiver can be expressed as [106]:

$$P_r = P_t \frac{G_r G_t G d_x d_y \lambda^2}{64\pi^3} \left| \sum_{m=1-\frac{M}{2}}^{\frac{M}{2}} \sum_{n=1-\frac{N}{2}}^{\frac{N}{2}} \frac{\sqrt{F^{combine}_{n,m}}\,\Gamma_{n,m}}{r^t_{n,m} r^r_{n,m}} e^{\frac{-j2\pi(r^t_{n,m}+r^r_{n,m})}{\lambda}} \right|^2, \qquad (2\text{-}10)$$

Where

- G_r, G_t, G are the gain of the reader antenna, the transmitter, the unit cell, respectively,
- $\Gamma_{n,m}$ is the reflection coefficient of the cell in the nth row and mth column,
- d_x, d_y are the size of each unit cell along the x axis and y axis respectively,
- $F^{combine}_{n,m}$ corresponds to the effect of the normalized power radiation patterns on the received signal power.

- $r_{n,m}^{t}, r_{n,m}^{r}$, represents the distance between the transmitter and the cell, and the distance between the cell and the receiver.

The signal at the receiver corresponds to the sum of all the contributions of the elements. Thanks to the signal reflection of the RIS, the reader is able to receive signal from the transmitter. Deployed in a wireless network, this kind of devices can extend the coverage to non-line-of sight location of the base station.

In this example, the reflection coefficient $\Gamma_{n,m}$ models the phase-shifting and amplitude modulation capabilities of the RIS. As the reflection coefficients of the cells can be tuned independently, the RIS can combine all the reflected signals to partially control the propagation channel. Therefore, the RIS can be tuned to achieve passive reflection beamforming and similarly to beamforming weights of mMIMO antennas a "precoder" of reflection coefficients can be calculated to passively reflect the signal toward a privileged direction.

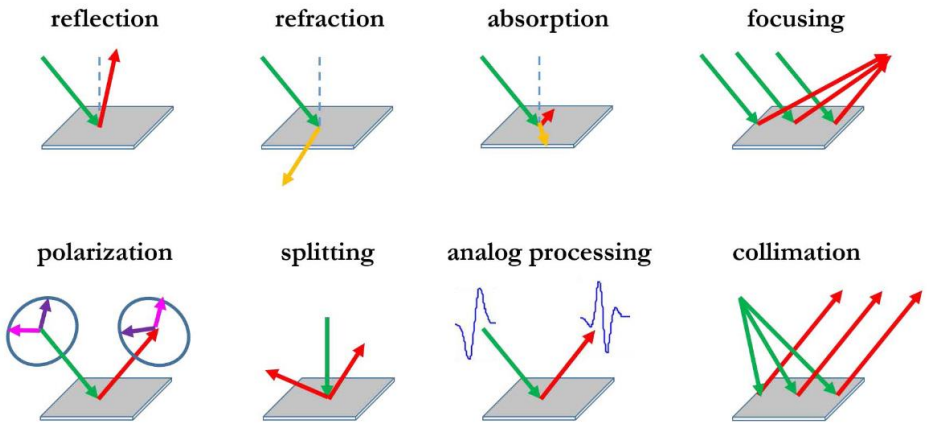

Figure 2-21 Function of the unitary cell [103].

Depending on the structure and the reconfigurability of the elementary elements, RISs can achieve different functions illustrated on the Figure 2-21.

2.4.2. Implementation and optimization

From a theoretical point of view, a precise and independent control of the reflection coefficients allows to perfectly beamform or focus the reflected signal. However, on a practical side, the RIS controls the reflection coefficients by adjusting the impedance of the elements. Therefore, it is much more complicated to achieve a complete control of the phase shift and the amplitude of the RIS elementary cells.

In the literature, different structures have been used to electronically adjust the impedance and to control the phase shift of RIS cells:

- PIN Diodes [107], they allow a two-state control, the diode can be configured in

reverse or forward direction to control the flow of the current. In this case, the elementary cell is a complex structure where the diodes connect or disconnect some part of the cell. The elementary cell is designed such that depending on the state of the five diodes (ON or OFF) the currents on the surface of the cell will flow in different directions. It results in a discontinuous control of the phase shift applied to the reflected signal. As illustrated in the Figure 2-22 the cell can be design with multiple PIN diode to control the current paths. In the Table 2-4 we observe the phase-shift and the magnitude response for the four possible configurations of this elementary cell.

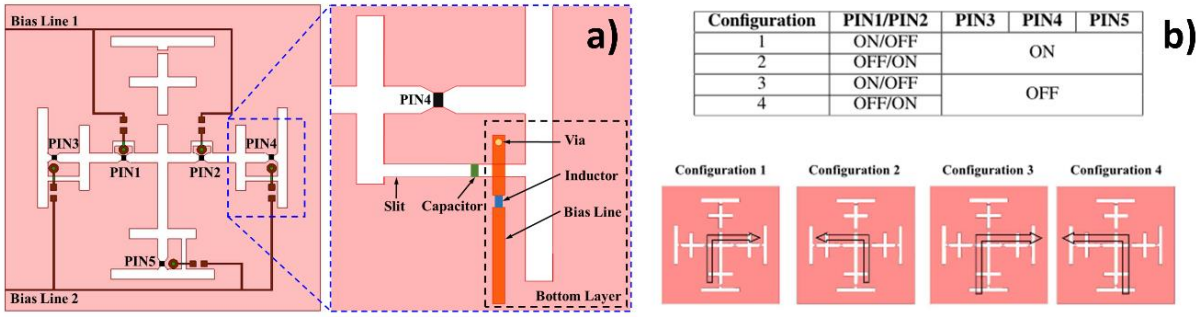

Configuration	PIN1/PIN2	PIN3	PIN4	PIN5
1	ON/OFF	ON		
2	OFF/ON			
3	ON/OFF	OFF		
4	OFF/ON			

Figure 2-22 a) Elementary cell structure with PIN diodes b) RF current path for different configurations of the cell [107].

Table 2-4 Phase-shift and amplitude of the reflection coefficient for different configurations of the cell [107].

Configuration	Phase Shift	Magnitude Response
1	$-205.5°$	-1.1 dB
2	$-383.2°$	-1.2 dB
3	$-290.2°$	-0.8 dB
4	$-110.3°$	-0.8 dB

- Varactor Diodes [108][106]: they allow a continuous control of the phase-shift. The capacitance of a varactor varies as function of the continuous (DC) voltage applied between its terminals. In [108], varactors are also located on the surface and connecting two areas of the cell. As the impedance of the varactors is changing, it modifies the total impedance of the cell resulting in modification of the behaviour of the cell. Mainly by tuning the varactors, we can control the phase shift of the reflected cell in a continuous manner. However the range of the phase shift may be limited and the amplitude of the reflection can also be varying as we observe in the Figure 2-23.

In a network environment, the RIS reflection coefficients must be configured by taking into account the phase shifting possibilities allowed by the RIS. The significant challenge is to find the optimal reflection coefficient to apply to the cells, different strategies can be envisaged for that purpose.

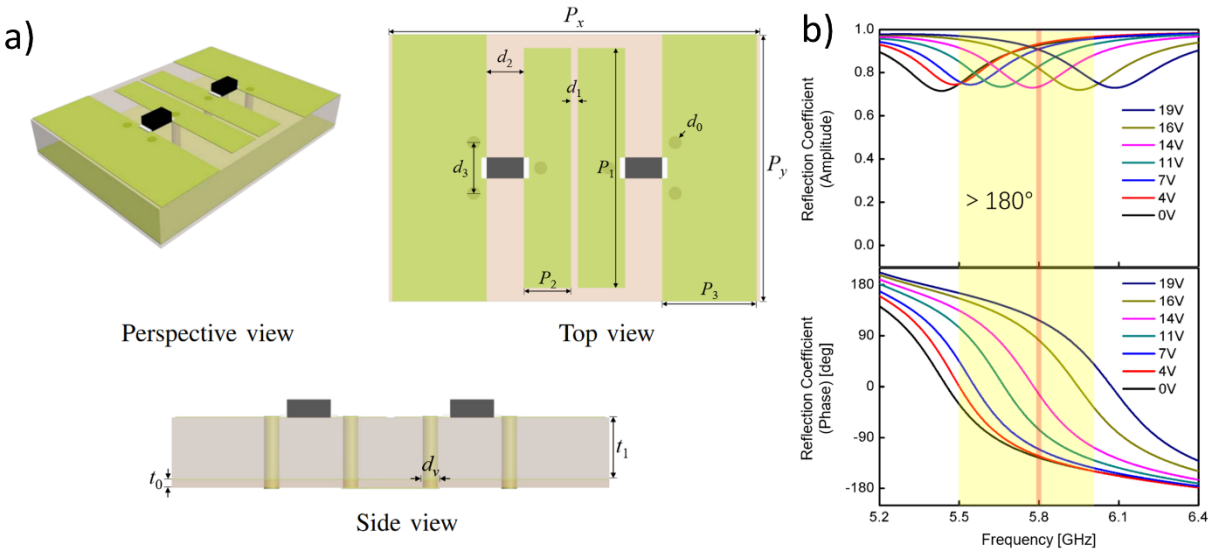

Figure 2-23 a) Elementary cell structure with varactors diodes b) Phase-shift and amplitude of the reflection coefficient for different voltage configurations of the varactors [108].

The reflection coefficient can be optimized based on the knowledge of the propagation channel thanks to channel estimation. This is a significant difficulty for a fully passive RIS that has no radio resources and no signal processing capability to send or receive pilots. Yet the channel estimation can be realized at the transmitter and/or receiver side. In [109] the channel estimation is developed based on a MMSE, and thanks to the estimated channels, the phase shifts of the RIS are optimized by using a gradient ascent algorithm. Various other channel estimation protocols have been proposed for RIS without radio processing capability, and based on cascaded channels, training sequences, joint optimization, etc. [110].

Another way to optimize the reflection coefficients of the RIS is to use machine learning (ML) algorithms. ML is a very useful technique performing in the case where the mathematical models are too complex. Recently lot of research proposed to applied ML algorithms to wireless communication, like in mMIMO optimization, scheduling, etc. [111][112][113]. ML can also be used to optimize the phase shift of the RIS, it has been demonstrated that a trained neural networks can perform better than conventional approaches [114]. Another neural network approach is detailed in [Huang] and show the possibility to focus the signal. ML is considered to be a potential enabler for smart networks using RIS.

The RIS technology shows a good potential to enhance wireless networks, therefore thanks to its capabilities RISs could be use in AmBC systems to improve the signal quality on the tags an reduce interference on the reader.

2.5. CONCLUSION

In this chapter we have presented, the backscattering communication principle and we detailed the specifications of the AmBC systems. Such systems are composed of a ambient source of

signal generating a signal originally intended to legacy receiver of a wireless network, a tag transmitting data by modulating the backscattering of the ambient signal and a reader that is detecting and decoding the signal from the tag. Ambient backscatter tags transmit information without generating additional waves, by recycling EM waves from their environment, thus this technique enables very low power communication.

In this chapter we have seen that the AmBC systems have promising capabilities and face multiple challenges. Indeed, some limitations remain and need to be overcome, mainly due to interferences and due to the low power feature. Hence we will proposed in the next chapter to improve AmBC systems thanks to recent technologies that are used in actual networks or that are envisaged for future networks. In this state-of-the art we have seen that three recent technologies can be investigated for AmBC system enhancement.

First we propose to implement reconfigurable antennas used in SM system to improve the performance of AmBC systems without increasing the tag compactness. Such antennas can be used to improve the reliability and the data rate of the system.

Secondly, we propose the mMIMO technique that is used in 5G networks. The mMIMO technology exploits the channel diversity and enables multi-stream transmission, beamforming or complex decoding algorithm. This technique can be implemented to increase the signal quality and to improve the detection in AmBC systems.

Finally, we propose to investigate RISs that are promising and that are a potential candidate for future 6G networks. RISs deployed in a network, can enhance the radio propagation environment, thanks to the reconfigurability of the elementary elements, the signal quality can be improved and blockages can be avoided. This RISs deployed in the environment could be used to improve the performance of AmBC systems.

Chapter 3

Polarization-Based Reconfigurable Tags for Robust Ambient Backscatter Communications

The main objective of this chapter is to study the improvement brought by the polarization effect of reconfigurable antennas on AmBC tags. We develop an analytical method to improve AmBCs by optimizing the polarization match between the source, the tag and the reader. We formulate an analytical solution to the optimization problem, and we evaluate the benefit of this approach by simulation based on the MoM. Finally, we experimentally validate the polarization reconfigurable tag principle and we show a significant performance improvement.

3.1. INTRODUCTION

Although AmBC is a promising low-power technology, we have seen in 2.1.7 that it suffers from different limitations. Indeed, for some locations due to interference effects between the source-to-reader direct path and the backscattered path, the signal contrast is weak and the energy detector performance is poor. Such deep fades locations of the signal contrast also occur in scattering environments. In addition, even if the tag is not at such locations, the contrast level may not be good enough if the polarizations of the tag, reader, and source are not matched [31]. Channel polarization is an important aspect that has been studied for RFID tags and RFID readers in [115]. To guarantee a minimum polarization match, a circular polarized antenna at the reader side has been proposed in [116], however, this solution is not optimal.

More recently, a tag based on a compact reconfigurable antenna has been proposed to achieve higher data rates for application to AmBC systems [71]. The antenna switches between four radiation patterns with distinct dominant linear polarizations. Such compact polarization-based reconfigurable (PR) antennas have been proposed for spatial modulation application [69][70]. These PR antennas are used in [69] and [70] to spatially modulate the transmitted signal thanks to different patterns with low inter-correlation. In this chapter, we propose to use these PR antennas to backscatter the ambient signal and to improve the robustness of AmBC systems as

well.

To perform the detection of tags equipped with such antenna some solutions based on the minimum mean square error can be implemented, instead of the conventional energy detector [88]. Because these solutions are highly complex, we propose to study the lower complexity least square error estimator.

We introduce a PR tag to improve the robustness of the tag-to-reader link against the source-to-reader direct interference. In Figure 3-1, we consider a PR tag embedded in a rich scattering environment. Instead of using the PR tag to increase the spectral efficiency and the data rate of the tag-to-reader link [71], we use it to improve the robustness of the tag-to-reader link against noise and source-to-reader interference.

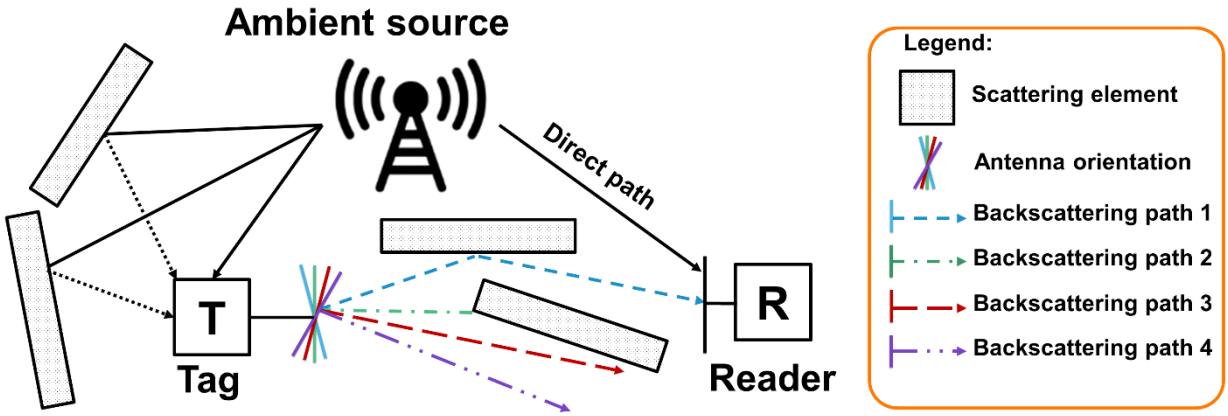

Figure 3-1 Tag with different polarizations that is illuminated by an ambient signal in a rich scattering environment, and that backscatters its message to the reader.

In this chapter, we consider and compare two different coding schemes that exploit polarization diversity to improve the performance. In the first one, the tag, as any standard two-state tag, sends its message by switching its operation between a backscattering state and a "transparent" state. In practice, this is realized by switching the antenna between two different load impedances. This coding scheme is referred to as "Backscattering/Transparent Scheme" (BTS). With this approach, the tag sends the same message several times, but using a different configured radiation pattern (and corresponding different polarization) at each transmission time. The rationale of this approach lies in the possibility of receiving a good quality signal over at least one polarization state.

To make an initial assessment of the benefits of the proposed tag, we introduce a simple model of the tag that can be studied theoretically and numerically with the aid of an electromagnetics-based simulation software (NEC2) based on the MoM, and that can be tested experimentally by using dipole antennas. We model the tag as a device that can switch between N_{pol} polarizations. This is obtained by rotating a dipole antenna across N_{pol} different orientations. The dipole is connected to a load impedance with two different values in order to create the backscattering and

the transparent transmission states.

In addition, we introduce a second coding scheme, according to which the tag backscatters ambient signals with different polarization patterns. The information bits are encoded by switching among a subset of available patterns, according to the spatial modulation principle [66][62][117][118][119][120][121]. This coding scheme is referred to as "Polarization Coding Scheme" (PCS). Similar to the BTS scheme, we expect that an appropriate (optimized) choice of a subset of polarization states will improve the system performance. The proposed implementation is assessed experimentally by using a compact reconfigurable antenna that is made of a split ring resonator antenna and a cross-polarization antenna.

The rest of this chapter is organized as follows: Section 3.2 introduces the system model and the methodology for performance evaluation. Section 3.3 reports a theoretical and simulation-based performance analysis of the BTS coding scheme. In particular, the best direction of polarization is identified under LOS propagation conditions. Section 3.4 reports the simulation and experimental validation of the proposed approach under a rich scattering propagation environment. Section 3.5 focuses on a performance comparison between an energy detector and a least square error receiver. Section 3.6 presents simulation and experimental results that compare different compact reconfigurable antennas. Finally, Section 3.7 concludes this chapter.

3.2. System Model And Methodology Of Analysis

3.2.1. System Model

We consider a system composed of a source, a tag and a reader. The source radiates an ambient signal at the carrier frequency f corresponding to a wavelength λ. The source and reader are equipped with a half-wavelength linearly polarized dipole antenna of length $l^D = \lambda/2$. The radius of the conductors is assumed to be much smaller compared to all other dimensions (thin-wire approximation).

The Cartesian coordinates of the center of the dipole antennas of the source, the tag, and the reader are denoted by (x^S, y^S, z^S), (x^T, y^T, z^T) and (x^R, y^R, z^R), respectively. The orientation angles of the dipole antennas of the source and reader are denoted by (ϕ^S, θ^S) and (ϕ^R, θ^R), respectively.

The antenna of the tag can switch among N_{pol} radiation patterns with distinct dominant polarization states. The complex signal received by the reader antenna is $y \in \mathbb{C}$:

$$y = (h^{SR} + \gamma h^{ST} h^{TR})\sqrt{P^{Tx}} + v, \tag{3-1}$$

where $h^{\mathrm{SR}} \in \mathbb{C}$, $h^{\mathrm{ST}} \in \mathbb{C}$, $h^{\mathrm{TR}} \in \mathbb{C}$ and are the channel coefficients of : the direct path between the source and the reader, the path between the source and the tag, the path between the

tag and the reader. The complex number γ is the modulation factor that corresponds to the state of the tag (i.e., "transparent" state or backscattering state), $v \in \mathbb{C}$ is the Gaussian noise at the reader and P^{Tx} is the power transmitted by the source. By introducing the aggregated channel $g = h^{SR} + \gamma h^{ST} h^{TR}$, with $g \in \mathbb{C}$, the received signal can be rewritten as follows:

$$y = g\sqrt{P^{Tx}} + v \tag{3-2}$$

Let $P^{noise} = E[\|\mathbf{v}\|^2]$ denote the received noise power. The signal-to-noise ratio, denoted by SNR^{Tx}, is defined as the ratio between the power transmitted by the source and the noise power at the reader:

$$SNR^{Tx} = \frac{P^{Tx}}{P^{noise}} \tag{3-3}$$

To allow a fair comparison between different types of tags, the transmitted power and the noise power are assumed to be fixed. Hence, SNR^{Tx} is assumed to be fixed. Also, we introduce $SNR^{captured}$ to denote the average the signal-to-noise ratio SNR, which is given by the ratio of the power captured by the reader (P^{Rx}) when the tag operates in the transparent mode and the noise power at the reader:

$$SNR^{captured} = \frac{P^{Rx}}{P^{noise}} \tag{3-4}$$

We consider a sequence of R bits $\mathrm{b} = b_1 \dots b_r \dots b_R$ sent by the tag and we denote $\hat{\mathrm{b}} = \hat{\mathrm{b}}_1 \dots \hat{\mathrm{b}}_r \dots \hat{\mathrm{b}}_R$ the sequence of R bits detected by the reader. The BER is defined as follows:

$$BER = \frac{\sum_{r=1}^{R} \left|\hat{\mathrm{b}}_r - \mathrm{b}_r\right|^2}{R}, \tag{3-5}$$

We consider that the quality of service is met by the tag-to-reader link when a given BER^{target} is achieved. The outage probability is hence defined, for given values of SNR^{Tx} or $SNR^{captured}$, as the probability of the event such as $BER < BER^{target}$.

3.2.2. Propagation environment

Different propagation environments are analyzed.

a) LOS. The LOS environment corresponds to a free space propagation environment between the source, the tag, and the reader.

b) Scattering Environment. In this case, we consider different elements including scatterers and reflectors. A scatterer is modelled as a conductive line defined by its length l^{SC}. The number of scatterers is denoted by N^{SC}. Reflectors are modelled as reflective planes, such as the ground plane and their number are denoted by N^{RP}. Each scatterer is randomly positioned but the distance between any dipole antenna and the scatterer is $D^{SC-X} > \lambda$. The distance from each

randomly distributed scatterer and the reader is constrained to be $D^{SC-R} < 10\lambda$. Dipoles antennas are spaced at least half of the wavelength apart.

3.2.3. Reconfigurable Antennas for the Tag

In order to implement the tag, we consider three types of reconfigurable antennas.

a) Rotating Dipole Antenna. The tag is a half-wavelength dipole antenna with linear polarization which is rotated mechanically. The polarization is controlled by changing the orientation of the antenna. This implementation allows us to have an antenna that is "continuously" reconfigurable in polarization. More specifically, three types of tags are considered: 1) an "ideal" polarization reconfigurable (IPR) tag that is able to be configured for any directions of polarization; 2) a more realistic 4-polarization reconfigurable (4PR) tag that can realize four directions of polarization; and 3) a non-reconfigurable (NR) tag with a fixed polarization. As an illustrative example, Figure 3-2 shows the orientation angles of a tag. The angles are denoted by (ϕ^T, θ^T).

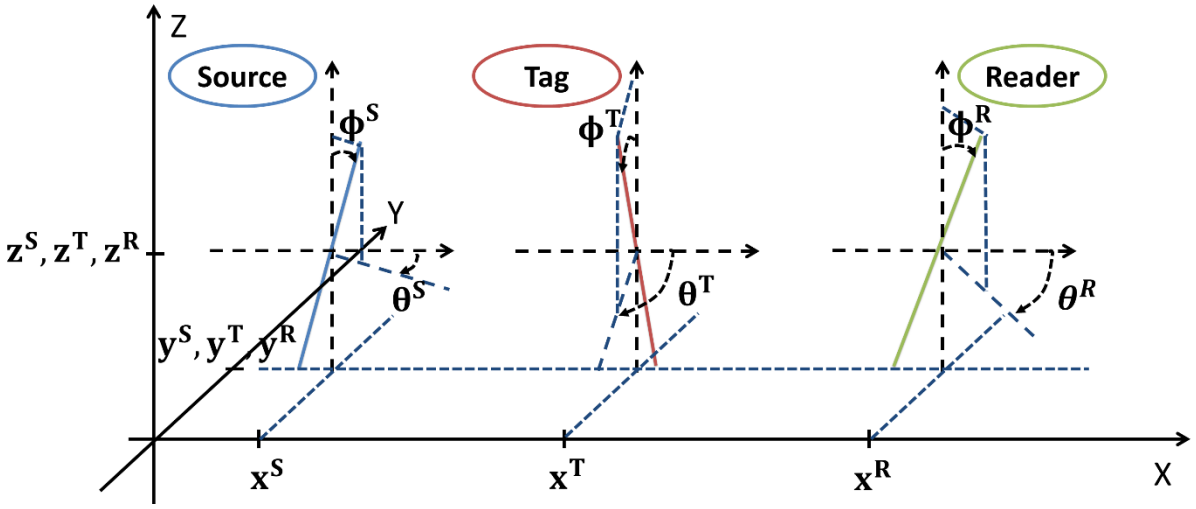

Figure 3-2 3D model of the system for a dipole tag.

b) Split Ring Resonators (SRR). Antenna. In this case, the tag is realized by using split ring resonators (SRR) [71] [69]. More precisely, the tag is composed of four resonators and four PIN diodes. By controlling the PIN diodes, one can connect or disconnect the resonators and, hence, change the polarization pattern of the SRR antenna. In this chapter, we consider only four patterns in order to compare the SRR antenna with the 4PR rotating dipole antenna. For performance optimization, the four patterns are those that provide the most distinguishable polarization states. The polarization patters are provided in Section 3.6 (Figure 3-16).

c) Cross-Polarization Antenna (XPOL). In this case, the tag is realized by using a cross-polarization antenna [10]. The polarization state is changed by using PIN diodes. In particular, only four polarization states of the eight possible polarization states are considered [71]. The polarization patters are provided in Section 3.6 (Figure 3-17).

3.2.4. Coding scheme

As explained, to transmit in a reliable manner the R bits from the tag to the reader, two coding schemes are analyzed.

a) Backscattering/Transparent Scheme (BTS). The tag sends its message, for a given polarization of the antenna, by switching between two states corresponding to different load impedances connected to the antenna. The two states are: (i) the backscattering state that is obtained by short-circuiting the dipole antenna strands; and (ii) the transparent state that is obtained by open-circuiting the dipole antenna strands.

The two different states are used to encode the bits. Basically, in (3-1), the backscattering state corresponds to a modulation factor $\gamma^{(1)} = 1$, i.e., $g^{(1)} = h^{SR} + h^{ST}h^{TR}$, and the transparent state corresponds to a modulation factor $\gamma^{(0)} = 0$, i.e., $g^{(0)} = h^{SR}$. According to the BTS coding scheme, the tag repeats the message several times by using a different radiation pattern and polarization at each transmission instance in order to make the transmission more robust and reliable. It is expected, in fact, that at least one polarization pattern is more reliably detected by the reader.

b) Polarization Coding Scheme (PCS). The tag sends the message by switching between two polarization patterns of a pair of patterns (among several available pairs of patterns) and each pattern corresponds to a different bit. Similar to SM, the reader is able to determine the polarization pattern used by the tag. In this coding scheme, tag is always backscattering but with different polarization patterns, so the modulation factor is equal to 1. In particular, bit 1 is encoded by one polarization pattern and bit 0 is encoded by a different polarization pattern. In (3-1), the bit 1 corresponds to $g^{(1)} = h^{SR} + h^{ST}h^{\mathrm{TR}(1)}$, and the bit 0 corresponds to $g^{(0)} = h^{\mathrm{SR}} + h^{ST}h^{\mathrm{TR}(0)}$. Here $h^{\mathrm{TR(i)}}$ stands for channel between the tag and the reader while considering the i-th radiation pattern. It is expected this scheme to be quite performant if the detector can easily distinct the two states of the tag, since it takes advantage of uncorrelated polarization patterns.

3.2.5. Detectors

At the reader side, two different detectors are analyzed.

a) Energy Detector (ED). An ED measures the voltage at the port of the dipole antenna, which is induced by the total received signal. The ED, in particular, determines whether the received average power is above or below a threshold level in order to detect that transmitted bits. The voltages measured at the dipole antenna port of the reader when the tag is backscattering and when the tag is transparent are denoted by V^{ON} and $\mathrm{V}^{\mathrm{OFF}}$ respectively. From the measured voltages, the corresponding signal amplitudes ($|\mathrm{V}|$) A^{ON} and $\mathrm{A}^{\mathrm{OFF}}$ can be deduced for each state. The signal contrast $\Delta\mathrm{A}$ is defined as the difference of the received signals between the two states

of the tag:

$$\Delta A = |A^{ON} - A^{OFF}|. \quad (3\text{-}6)$$

The noise amplitude level is denoted by A^{noise}. Using this notation, the BER is defined as follows [47] :

$$BER = 0.5 erfc\left(\frac{\Delta A}{A^{noise}}\right) \quad (3\text{-}7)$$

where $erfc()$ denotes the complementary error function.

b) *Least Square Error (LSE) Detector.* This detector operates in two phases. First it estimates the channel for the states of the tag based on the coding scheme. Then, during the transmission of the tag, the transmitted bits are detected. The output of the detector can be formulated as follows:

$$\hat{y} = arg\ min\{\|z - y\|^2\} \text{ with } z \in \{g^{(0)}, g^{(1)}\}, \quad (3\text{-}8)$$

where $\hat{y} \in \mathbb{C}$ is the estimate of y. For each bit b_r, the reader calculates $\hat{y}$ for the two states $g^{(0)}$ and $g^{(1)}$ that correspond to bit 0 and bit 1, respectively. The estimated bit $\hat{b}_r$ corresponds to the smallest $\hat{y}$.

3.2.6. Channel Modeling

Three different channel models are considered, and are analyzed analytically, and by using simulations and experiments.

a) *Analytical Model.* In order to assess the performance of the considered backscattering system, we introduce a model for the polarization-based dipole antenna in a LOS propagation environment. This is discussed in Section 3.3.

b) Numerical Electromagnetic Code (NEC) Simulator. The dipole antennas are studied by using the NEC2 simulation software. NEC2 is a software based on the MoM. By using NEC2, it is possible to model and configure the dipole antennas, the source, the tag, the reader, the N^{SC} scatterers, a ground plane, the load impedances, and the physical characteristics of the dipole antennas. In particular, this tool allows us to (i) configure the state of the tag (transparent or backscattering), by changing the load impedance; and (ii) to measure the resulting voltage at the reader port.

c) *Experiments.* Besides analysis and simulations, we perform measurements to estimate the channels. The obtained empirical channels are used to validate the analytical model and the simulations.

3.2.7. Summary of Case Studies Analyzed

Table 3-1 lists all systems and performance evaluation methodologies considered in this

chapter. We note that the XPOL and SRR antennas radiation patterns are complex to be modeled analytically and through the MoM software. Therefore, these cases are analyzed only through experiments.

Table 3-1 Case Studies and evaluation methodologies.

Section	***Environment***	***Antenna***	***Coding Scheme***	***Detector***	***Channel modeling***
3.3	LOS	Rotating Dipole	BTS	ED	Analytical
3.4.1and 3.4.2					4NEC2
3.4.1 and 3.4.2 3.5.1 and 3.5.2	Scattering				
3.4.4					Experiments
3.5.1 and 3.5.2				LSE	4NEC2
3.6.2			PCS		
3.6.2		SRR			Experiments
3.6.2		XPOL			

3.3. ANALYSIS IN LOS ENVIRONMENTS

In this section, we consider a LOS propagation environment, i.e. N^{SC} and N^{RP} equal to zero. Only the source, the tag and the reader are considered. We consider a rotating dipole antenna, a BTS coding scheme, and an ED detector. The carrier frequency f is set to 2.4 GHz. We limit the study to an IPR tag in order to find the best polarization for the tag and some upper bound performance.

3.3.1. Selection of the Optimal Polarization

In this section, we propose an approach to find the orientation of the linear polarization that maximizes ΔA. We assume that the source, the tag and the reader have a perfect linear polarization. Under these assumptions, the direction of the electric field is given by the orientation of the dipole antennas. Let $\vec{\mathbf{S}}$ be the normalized incident electric field vector and let $\vec{\mathbf{T}}$ and $\vec{\mathbf{R}}$ be the unitary vectors that determine the orientations of the dipoles of the tag and the reader, respectively. Each path contribution is proportional to a polarization factor that lies between 0 and 1. For a given position and orientations of the dipole antennas, the polarization factor of the direct source-to-reader path S^{direct} is given by the projection of $\vec{\mathbf{S}}$ over $\vec{\mathbf{R}}$. As for the source-to-tag-to-reader polarization factor (S^{back}), it is approximated as the projection of $\vec{\mathbf{S}}$ over $\vec{\mathbf{T}}$, then on $\vec{\mathbf{R}}$:

$$S^{direct} = \left|\vec{\mathbf{S}} \cdot \vec{\mathbf{R}}\right|, \tag{3-9}$$

$$S^{back} = \left|(\vec{\mathbf{S}} \cdot \vec{\mathbf{T}})(\vec{\mathbf{T}} \cdot \vec{\mathbf{R}})\right| \tag{3-10}$$

where $\cdot$ is the inner product. The objective is to maximize the polarization factor of the

backscattering path S^{back} while limiting the polarization factor of the direct path S^{direct}. For a fixed vertically polarized source ($\phi^S = 0$), we obtain the following optimal solution:

$$\begin{cases} \theta^T = \theta^R \ [2\pi] \\ \phi^T = \dfrac{\phi^R}{2} \ [2\pi] \end{cases} \tag{3-11}$$

From (3-11), we conclude that there exists an optimal orientation for the tag. Therefore, an IPR tag is expected to outperform an NR tag. The derived optimum orientation of the tag can be interpreted as follows: the best orientation of the IPR tag is obtained when the tag simultaneously maximizes the received signal from the source and maximizes the backscattered signal to the reader. This is obtained when the angle between the source and the tag is equal to the angle between the tag and reader.

3.3.2. 4NEC2-based Validation

We validate the proposed analytical result by using simulations. The 4NEC2 simulation tool takes into account the following elements that are not taken into account in the analytical model: the wire length, the coupling between the elements, the LOS propagation, and the radiation diagram. For a given set of source, tag and reader locations and for a given set of reader orientations, we determine by simulation, through an exhaustive search, the orientation of the tag that maximizes ΔA. The numerical search is performed over a reduced number of angles due to the symmetry: (ϕ^R, θ^R) in $([0,10,\dots,90],[0,10,\dots,90])$ and (ϕ^T, θ^T) in $([0,10,\dots,90],[0,10,\dots,180])$ degrees. For a given reader orientation, once the optimal tag orientation is found, we compare two unitary vectors giving the best orientation of the tag according to two different methods:

- $\vec{\mathbf{T}}^{best-th}$ obtained through the analytical method;
- $\vec{\mathbf{T}}^{best-simu}$ obtained through exhaustive search.

Figure 3-3 illustrates the inner product between $\vec{\mathbf{T}}^{best-th}$ and $\vec{\mathbf{T}}^{best-simu}$. A high inner product (close to 1) means that the polarization found with the analytical model matches the polarization obtained by exhaustive search. Figure 3-3 shows that the optimal polarizations match for more than 80% for reader orientation $\theta^R > 50°$ or $\phi^R < 45°$. The analytical approach is, therefore, valid in most cases. The cases where the model is not valid correspond to the source being out of the "donut" diagram of the reader dipole and are therefore of low interest.

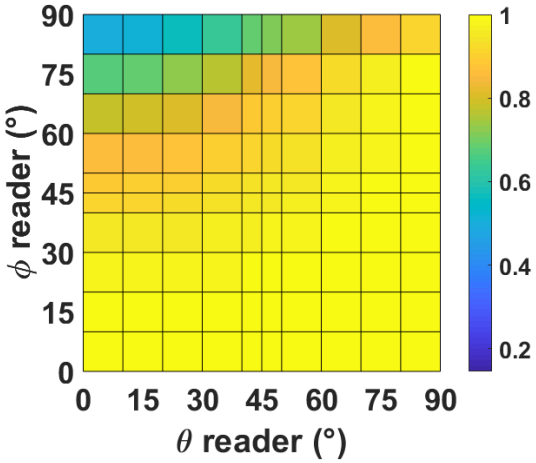

Figure 3-3 Comparison of the best orientation obtained by using the model and an exhaustive search (inner product of $\vec{T}^{best-th}$ and $\vec{T}^{best-simu}$).

3.3.3. Takeaway Messages from the Analysis

Based on our analysis, we conclude that, in a LOS propagation environment, the optimal orientation of the IPR tag corresponds to the average between the orientation of the source and the orientation of the reader.

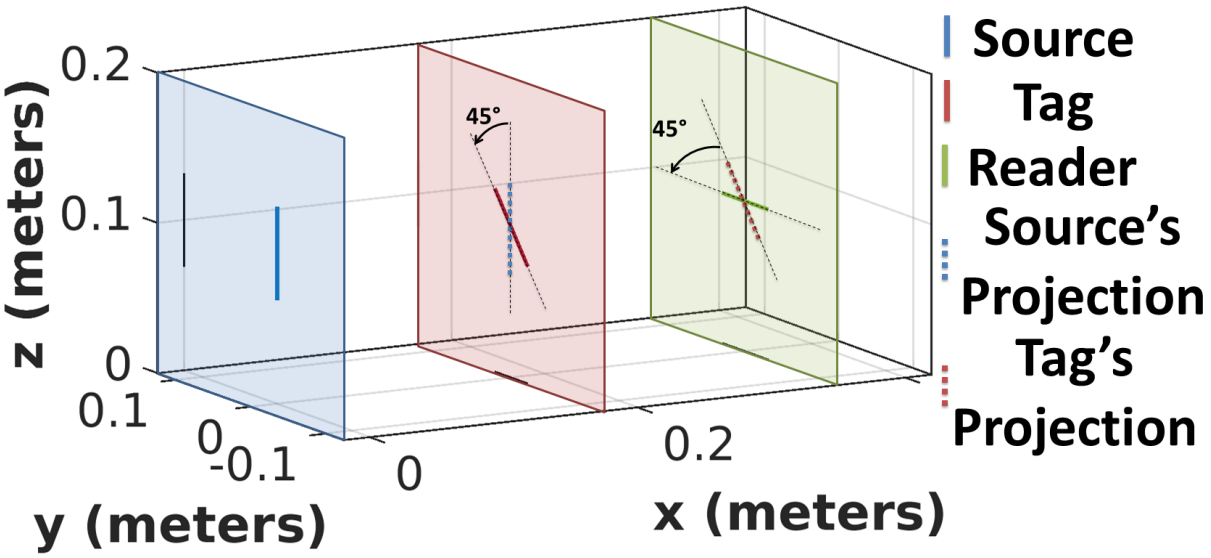

Figure 3-4 Example of optimal angle for a given source $(\phi^S, \theta^S) = (0°, 0°)$ and reader $(\phi^R, \theta^R) = (90°, 90°)$ configuration.

The advantage of a PR tag is in the worst case scenario, i.e., the source and the reader are orthogonal to each other, i.e. the source is 90° from the reader. In this case, the reader cannot receive any signal from the source. The current study shows that the IPR tag is better detected by the reader, when it is transmitting its message, with the direction of its linear polarization being at 45° from the source and 45° from the reader, as shown in Figure 3-4.

In a real environment, in addition to the LOS propagation path studied in this section, additional propagation paths exist (due to scatterers and reflectors). This is studied in the next section.

3.4. Analysis In A Rich Scattering Environment

In this section, we consider a rich scattering environment, with a large number of scatterers and a few reflective planes. We consider rotating dipole antennas, the BTS coding scheme, and an ED detector.

Table 3-2 System model parameters.

Parameters	***Definition***	***Value***	***Units***
(x^S, y^S, z^S)	Source localization	$(0, 0, 0.3)$	m
(ϕ^S, θ^S)	Source orientation	$(0, 0)$	deg
(x^R, y^R, z^R)	Reader localization	$(100, 0, 0.3)$	m
(ϕ^R, θ^R)	Reader orientation	$(90, 90)$	deg
(x^T, y^T, z^T)	Tag localization	$(x^T, y^T, 0.3)$	m
l^{SC}	Length of scatterers	$\lambda/2$	m
Z^{R}	Reader load impedance	50	Ω
BER^{target}	Target bit error rate	10^{-2}	

The carrier frequency f is set to 2.4 GHz. We consider the three different types of tags. As mentioned, the 4PR and NR tags have $N_{pol} = 4$ and $N_{pol} = 1$, respectively. The IPR tag has $N_{pol} = 81$. The considered simulation environment accounts for $N^{SC} = 20$ scatterers and one ground plane ($N^{RP} = 1$). The waves travel from the source to the reader through the LOS path and through multiple non-line-of-sight (NLOS) paths due to presence of the scatterers in proximity of the reader and the ground plane. Whereas the linear polarization of the wave remains unchanged along the LOS path, it may change on the NLOS paths. Hence, at the reader side, the source-to-reader signal results from the combination of incident waves with distinct linear polarizations. It is expected, however, that the linear polarization of the LOS path is dominant.

3.4.1. Numerical analysis of Polarization and Performance

In this section, we illustrate the best linear polarization of the tag by using NEC2 simulations. Source and reader orientations are fixed and orthogonal to each other, as it is a worst case scenario in terms of received SNR. We analyze the performance of the communication link as a function of tag's coordinates (x^T, y^T), i.e., we illustrate 2D spatial maps of the BER. Other simulation parameters are detailed in Table 3-2. We study the three types of tag for different configurations of their orientation and for different environments (LOS or with scattering). Figure 3-5 illustrates BER maps of some of the configurations in Table 3-3 by assuming $SNR^{Tx} = 116\ dB$. The spatial maps of the BER show the locations where the tag can be detected by the reader with the target

QoS ($BER < BER^{\text{target}}$). Light colors (yellow or red) indicate where QoS can be achieved and dark colors (blue) indicate locations where QoS cannot be reached. Each subfigure of Figure 3-5 is accompanied by a "velvet carpet" illustrating the tag's best orientation depending on the tag's location. Each position on the velvet carpet corresponds to a tested position of the tag. The thread of the carpet at a given position illustrates the best orientation of the tag for the considered position. The velvet carpet illustrations in Figure 3-5-a,c,d) show that the orientation is uniform for NR tags and Figure 3-5-b,e,f) show that the orientation is non-uniform for PR tags.

Table 3-3 Tag and environment configurations.

	LOS	***Scattering***
NR tag in the worst orientation	LOS-NR-Worst	SCAT-NR-Worst
NR tag in the best orientation	LOS-NR-Best	SCAT-NR-Best
4PR tag	LOS-4PR	SCAT-4PR
IPR tag	LOS-IPR	SCAT-IPR

In Figure 3-5-a) and in Figure 3-5-b), we show the results obtained for the configuration in a LOS environment. Figure 3-5-a) illustrates the BER for the optimum orientation in LOS: $\theta^T = 90°$ and $\phi^T = 45°$. Figure 3-5-b) shows the contrast map in a LOS environment for the IPR tag. We observe that a PR tag has limited effects in a LOS channel if the source and the reader have a cross-polarization.

The following rotating dipole antenna tags are compared in a scattering environment.

- **NR Tag**: We study the performance of the NR tag when its fixed orientation is, on average, the optimal one. We determine numerically this best orientation. We observe that even in a scattering environment (Figure 3-5-c)), we obtain the same best orientation as in a LOS environment. Indeed, the optimum orientation in LOS, obtained by applying (3-6) to the parameters listed in Table 3-2, is $\theta^T = 90°$ and $\phi^T = 45°$. This is due to the fact that our studied scattering environment is close to a LOS environment. For comparison, Figure 3-5-d) illustrates the performance of the NR tag when its fixed orientation is, on average, the worst ($\theta^T = 90°$ and $\phi^T = 90°$), i.e., for which a very small amount of backscattered signal can be detected by the reader.
- **4PR tag**: The compact reconfigurable antennas presented in [71] have four patterns with distinct dominant linear polarization directions. The 4PR tag is a simplified model of such existing antennas. The angles of the 4 polarizations are set to $(\mathrm{x}^{\mathrm{T}}, \mathrm{y}^{\mathrm{T}}) = \{(0, 90), (45, 90), (90, 90), (135, 90)\}$ and correspond to the main polarization directions of one of the antennas from [71]. The SNR contrast maps are computed for the 4 polarizations of the tag.
- **IPR tag**: We consider an IPR tag with $N_{pol} = 81$. The orientations of the IPR tag

(x^T, y^T) are uniformly distributed in $([0,180],[0,180])$ degrees. We compute the BER maps for each of N_{pol}polarizations.

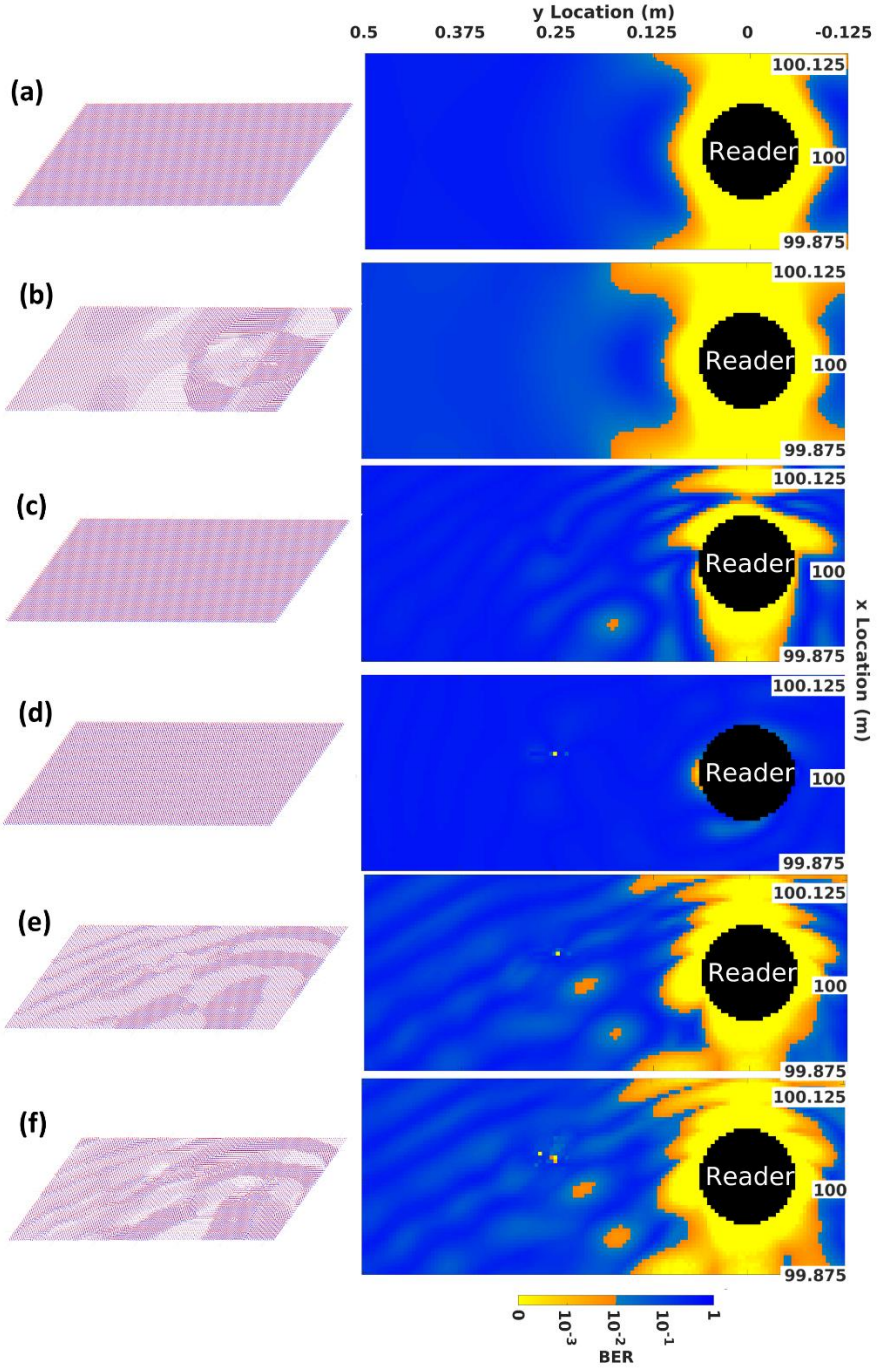

Figure 3-5 BER maps showing the tag location that guarantees QoS (in orange) for the configurations : (a) LOS-NR-Best, (b) LOS-IPR, (c) SCAT-NR-Best, (d) SCAT-NR-Worst, (e) SCAT-4PR, (f) SCAT-IPR. On the left of each subfigure, the tag orientation map (i.e. the velvet carpet) is illustrated.

As for the IPR and 4PR tags, we determine the polarization of the tag that minimizes the BER for every location of the tag based on the N_{pol} computed maps of each tag. We obtain the

corresponding optimal BER maps as illustrated in the Figure 3-5-e,f). As expected, Figure 3-5 shows that the IPR tag outperforms all types of tags. We also observe that the more realistic 4PR tag, with 20 times fewer available polarizations than the IPR tag, offers performance that is close to the IPR tag. The 4PR tag outperforms the NR tag, even if the NR tag employs the optimal orientation of the LOS system. Compared to the NR tag, the 4PR tag is more robust to the impact of scatterers and polarization mismatch.

In the next sub-section, we study the performance of the tags as a function of SNR^{Tx}.

3.4.2. Outage probability analysis

In the previous section, we have shown that a PR tag can improve the performance of an AmBC system in terms of BER. In this section, we numerically evaluate the outage probability for each configuration listed in Table 3-3. The outage probability is computed over a target coverage area, i.e., over tag's locations (in meters) defined by $D^{T-R} \in [0.5\lambda, 3\lambda]$, where D^{T-R} corresponds to the Euclidian distance between the tag and the reader. The BER is calculated as a function of SNR^{Tx}, for every tag location and orientation and for a given environment configuration of the source, the reader, the scatterers and the reflective planes. We compute the outage probability, based on (3-6), for the three types of tags.

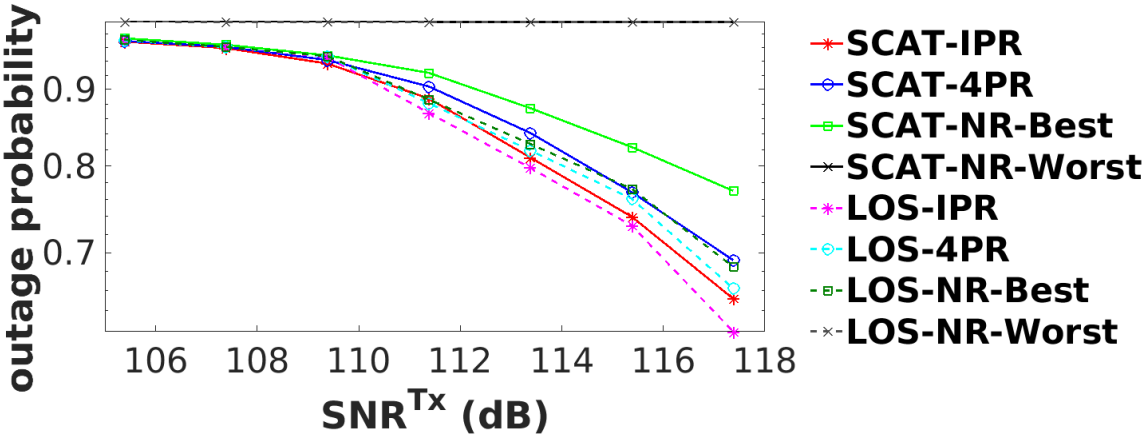

Figure 3-6 Outage probability simulated as a function of SNR^{Tx}.

Figure 3-6 shows that the IPR tag attains the best performance. It provides the lower bound performance for this environment configuration. The NR tag, even configured to operate at the optimal orientation, has a low outage probability, since it is not robust to scattering. Figure 3-7 shows the average captured SNR for each configuration as a function of SNR^{Tx}. In LOS, the amount of received power corresponds to the power backscattered by the tag, which depends on the tag polarization. However, as expected, in scattering environment, the $SNR^{captured}$ does not depend on the tag polarization (as it is measured when the tag is transparent) and only depends on the scattering. In the LOS-NR-Worst configuration, the NR tag and the reader are orthogonal to the source, thus the reader receives close to zero signal from the source and from the tag. We

observe that the increasing the number of reconfigurable polarizations N_{pol} of the tag improves the system performance. In addition, this improvement is boosted by the presence of scatterers. Finally, we observe that, even with a limited number of polarization orientations ($N_{pol} = 4$), the performance of the 4PR tag is close to the IPR tag.

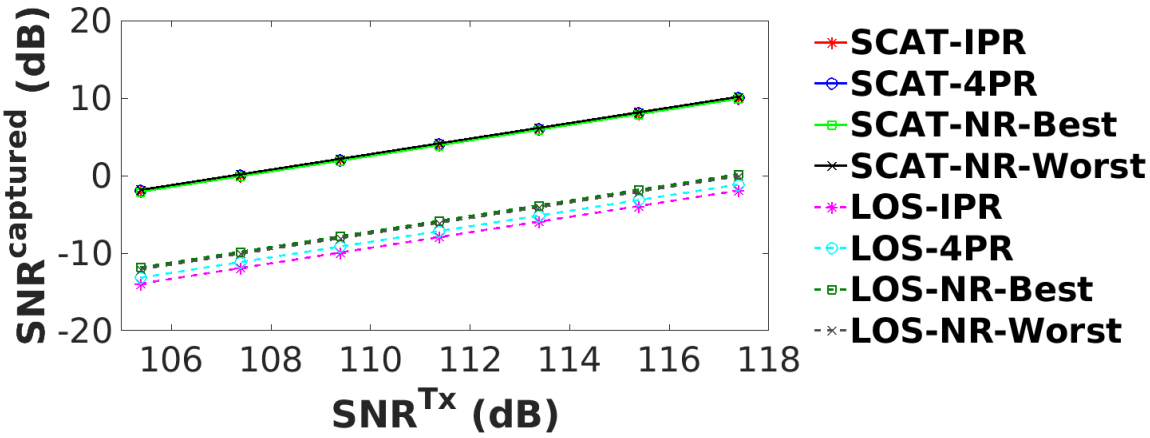

Figure 3-7 $SNR^{captured}$ *by the reader as function of the* SNR^{Tx}.

3.4.3. Impact of the scatterers

Figure 3-8 illustrates the amplitude of the signal A^{OFF}, respectively A^{ON}, received by the reader when the tag is transparent, respectively backscattering, as a function of the position of the tag in space, for two different propagation environments (LOS and with scattering), for two different tags (NR-Best and IPR), and for the ED detector. As the presence of scatterers results in additional paths in the source-to-reader propagation channel (in addition to the LOS path), the amplitude of the signal A^{OFF} , when the tag is in the transparent state, is much higher in scattering condition compared to the received signal A^{OFF} in LOS condition. As a consequence, in the scattering condition, the additional path due to the tag being in backscattering state is much less visible by the reader, compared to the LOS condition.

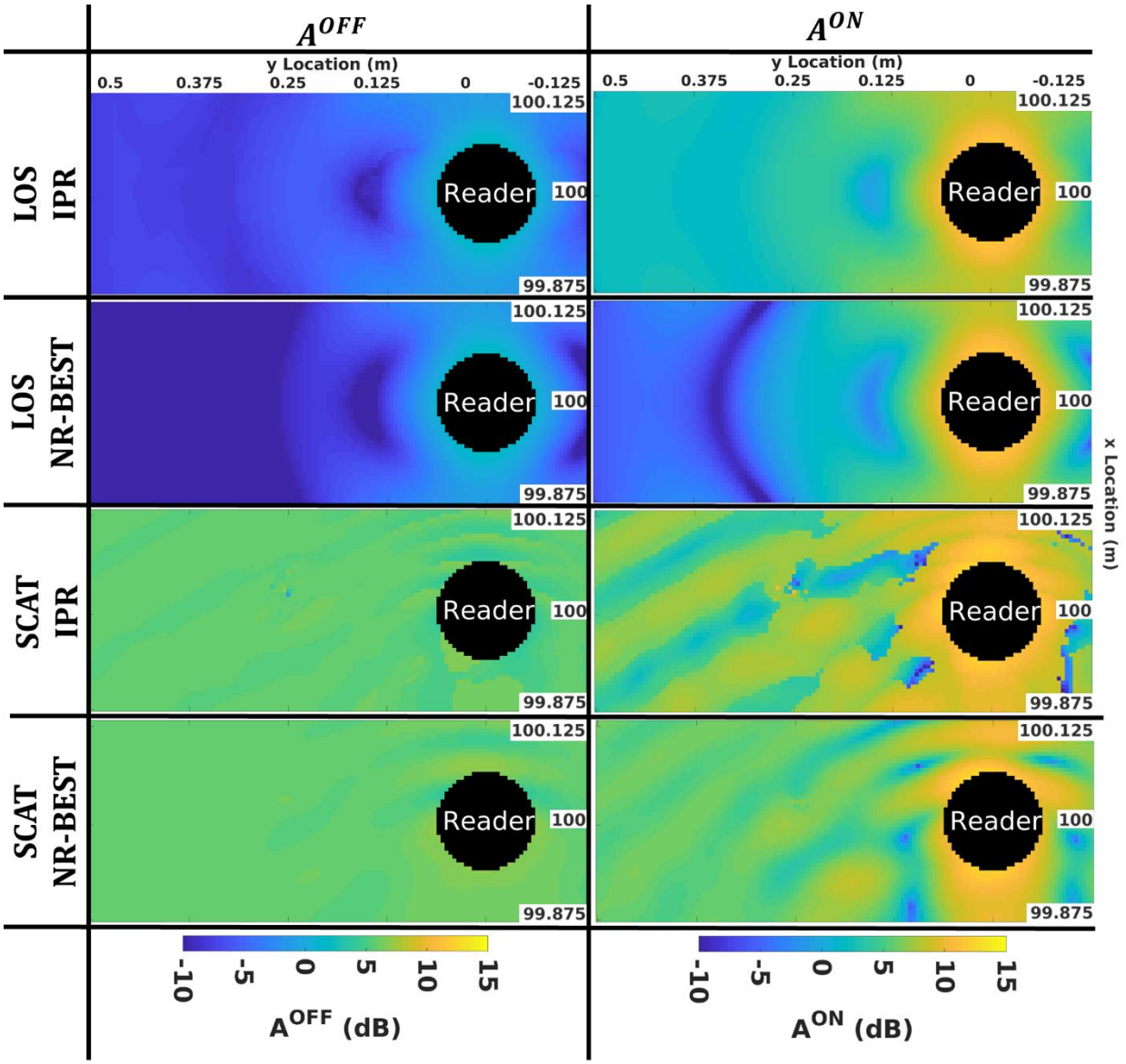

Figure 3-8 Amplitude maps for the transparent and backscattering state of the IPR and NR tags in scattering and LOS environment.

3.4.4. Experimental Verification

In the previous section, we have shown, with the aid of simulation, that a PR tag outperforms an NR tag. In this section, we validate this observation through experiments conducted in a semi-anechoic chamber. In our experimental set-up, we reproduced, as closely as possible, the conditions modeled in the simulation environment. Instead of scatterers made of conductive lines, we deploy reflective planes in the environment ($N^{SC} = 0, N^{SC} = 6$). Each of them has a different surface area and is placed randomly around the system, with different orientations and locations, as illustrated in Figure 3-9 and Figure 3-10. The source is located at a shorter distance from the tag and the reader (0.35m) as compared with the simulation results (100m). This is necessary

because of the limited size of the semi-anechoic chamber. To measure the signal contrast maps experimentally, the source and the reader are installed at fixed locations. The mechanically rotating dipole antenna of the tag is mounted on two motorized rails whose length is 0.3m.

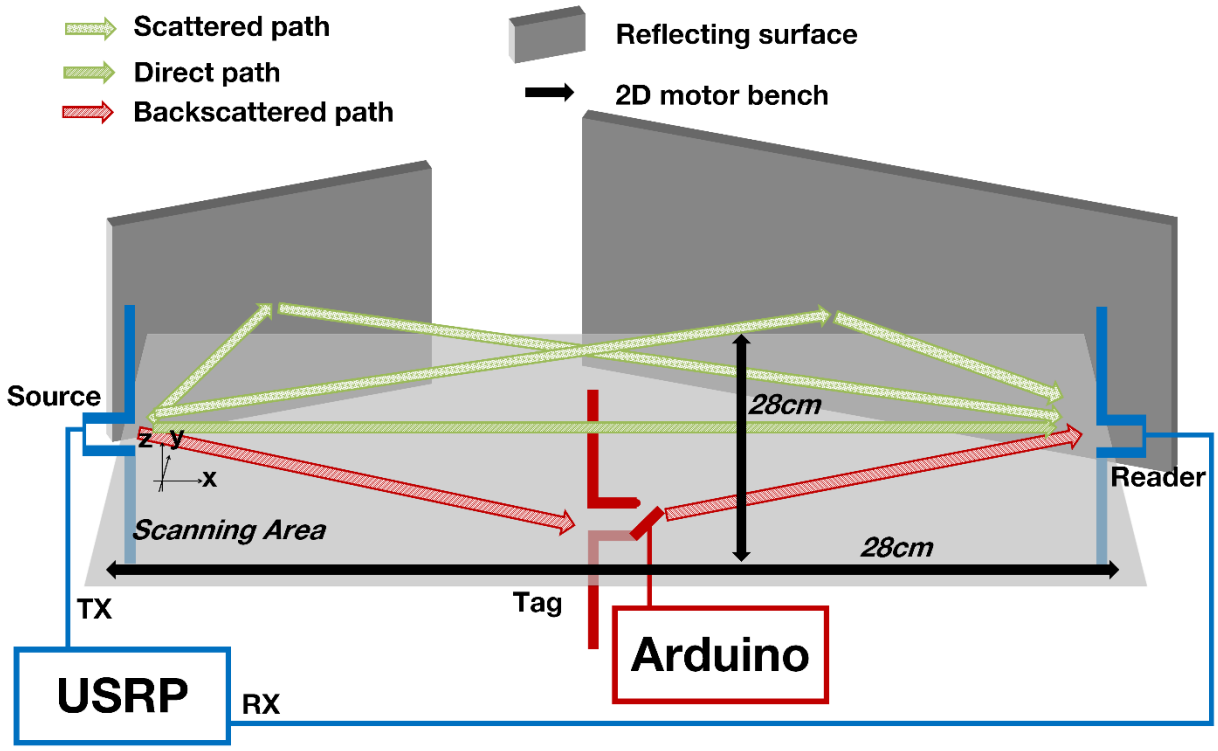

Figure 3-9 Experimental setup.

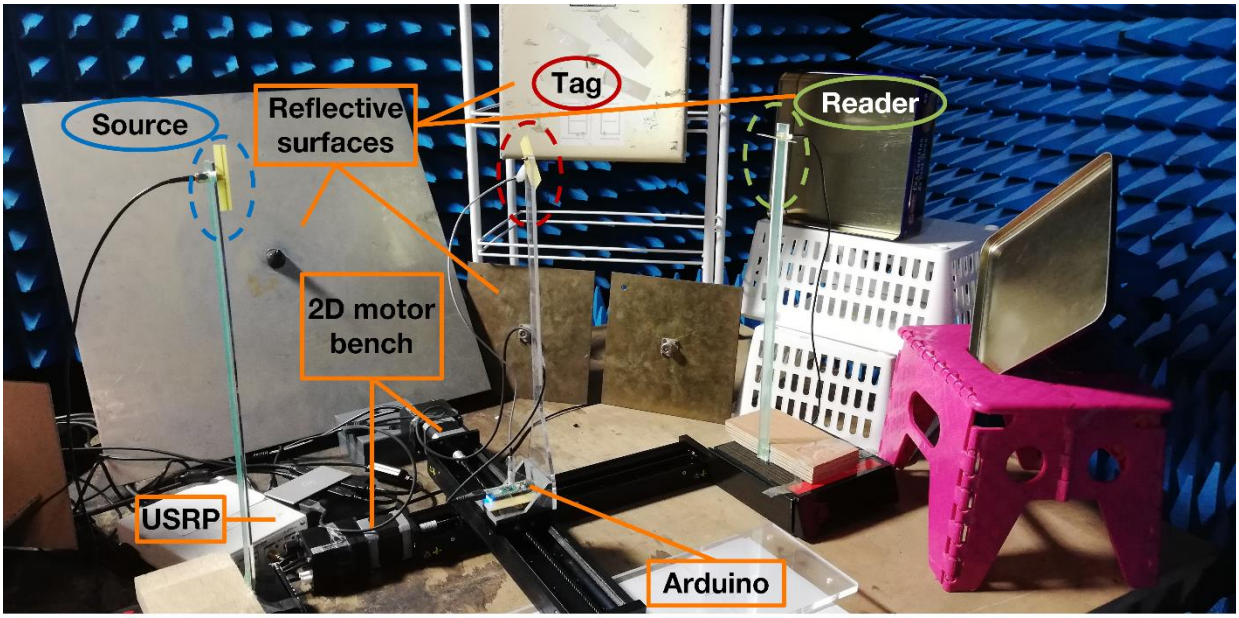

Figure 3-10 Photo of the experimental setup.

Each element is composed of a dipole antenna made of two strands with a total length of 6.25 cm. We connect the source and the reader to two different ports of a USRP B210. We use GNU

Radio to control the USRP and process the source and received signals. The tag's antenna is connected to an Arduino platform that controls the impedance connected to the two strands using a PIN diode.

We place the source at the origin of the axis, $(x^S, y^S, z^S) = (0,0,0)$, with a vertical orientation $(\phi^S, \theta^S) = (0,0)$. The reader is placed at position $(x^R, y^R, z^R) = (0.35,0,0)$ and is in cross-polarization with the source $(\phi^R, \theta^R) = (90,90)$. The tag is moved along a linear trajectory perpendicular to the line connecting the source and the reader, such that $x^T = xmin + nx \times step$ and $y^T = ymin + ny \times step$. We define $xmin = 0.03m$ and $ymin = -0.15m$ so that the tag scans the area between the source and the reader, given the limited range of 28 cm. The step of the tag displacement is $step = 0.01m$ along the x and y axis and $nx, ny \in [0,1,\dots,28]$.

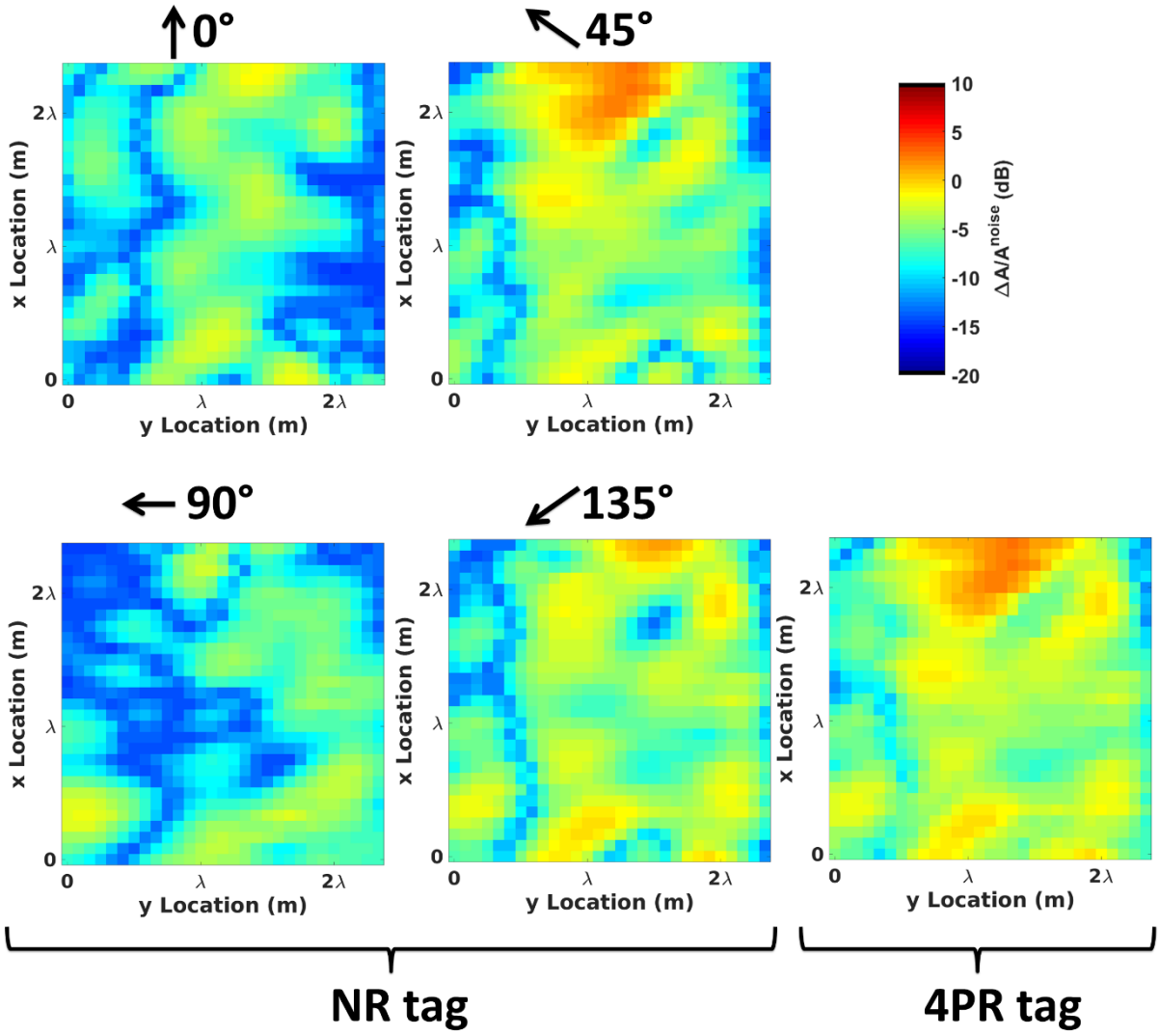

Figure 3-11 Experimental maps for four fixed orientations of the NR dipole tag ($\phi^T = 0°, 45°, 90°, 135°, \theta^T = 90°$) and the map for the 4PR tag: the optimum signal contrast map obtained after selection of the best polarization among the 4 available ones.

We measure the maps for the power of the backscattering and transparent states, P^{ON}, P^{OFF},

respectively, the noise power P^{noise}, and then calculate the $\frac{\Delta A}{A^{noise}}$ maps. We measure the signal contrast maps for each angle of the 4PR tag. We obtain 4 maps for signal contrast as shown in Figure 3-11.

We process these maps to determine the map with the best signal contrast. Experimental results show that selecting among four polarization orientations improves the performance of an AmBC system (Figure 3-11). Even though the experiment is not a perfect replica of the simulations, experimental and simulation results are consistent: both show that, in a complex environment, the maps depend on the orientation of the polarization of the tag, and that a PR tag is more robust.

3.4.5. Takeaway Message from the Analysis

Based on our study which relies on simulations and experiments, we conclude that the use of a PR tag improves the performance of an AmBC system in a rich scattering environment and that a simple 4PR tag provides good performance similar to an ideal tag.

3.5. IMPACT OF THE READER DETECTION SCHEME

In this section, we compare the performance of the ED and LSE detectors. We consider rotating dipole antennas, the BTS coding scheme, and a scattering environment. The configuration of the system is given in Table 3-3. We evaluate the BER maps for locations of the tag around the reader. The three dipole tags IPR, 4PR and NR are considered. The map is shown for a fixed $SNR^{captured} = 12\ dB$, which is equivalent to $SNR^{Tx} = 116\ dB$ in the scattering configuration.

3.5.1. Visualization of the Polarization and the Performance

Figure 3-12 shows the BER map for the three tags and for the two detectors. Similar to the previous section, the IPR tag provides the best performance for both detectors. The LSE detector, however, yields better BER performance and a larger coverage area. Even the NR tag that uses the best polarization orientation and the uses the LSE detector provides better performance than an IPR tag that uses an ED detector. The LSE detector has better performance than an ED as it compares the amplitude and the phase of the received signal with the estimated channel.

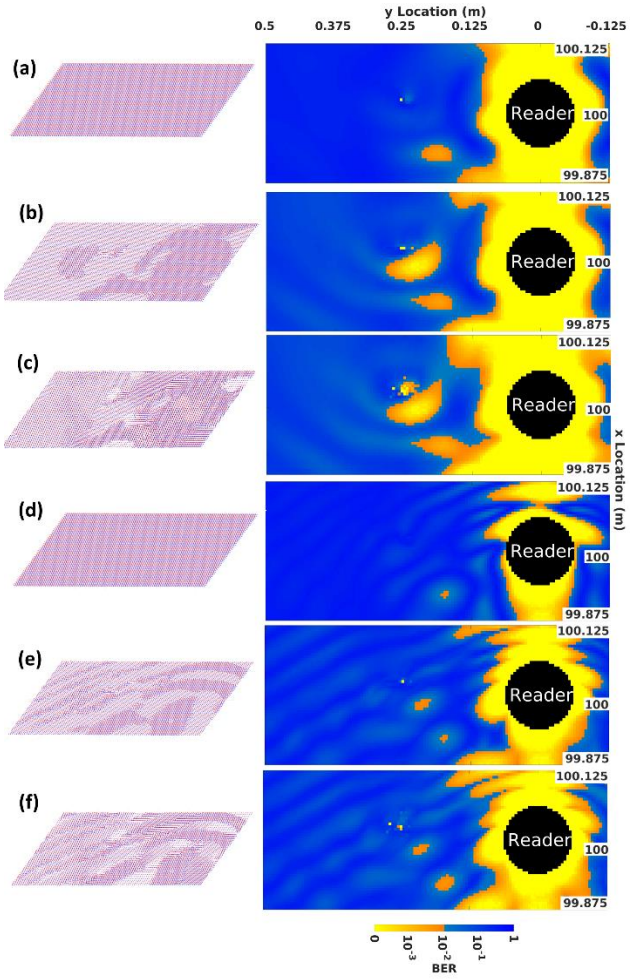

Figure 3-12 BER maps showing the tag location that guarantees QoS (in orange) for the configurations : (a) LSE-NR-Best, (b) LSE-4PR, (c) LSE-IPR, (d) ED-NR-Best, (e) ED-4PR, (f) ED-IPR. On the left of each subfigure, the tag orientation map is illustrated.

3.5.2. Outage Probability Analysis

In this section, we numerically evaluate the outage probability for each configuration setup reported in Table 3-3. The outage probability is computed over a target coverage area, defined such as the Euclidean distance D^{T-R} between the tag and the reader lies in the range $0.5\lambda < D^{T-R} < 3\lambda$. The BER is calculated as a function of $SNR^{captured}$ for every tag location and orientation and for a given configuration of the source, the reader, the scatterers and the reflective planes.

In Figure 3-13, we observe that the LSE detector improves the performance compared with ED detector. The IPR tag combined with the LSE detector outperforms the IPR tag combined with the ED detector. The 4PR has good performance that is close to the IPR tag. In conclusion, the LSE detector strongly outperforms the ED, and the 4PR tag with LSE provides close to ideal performance.

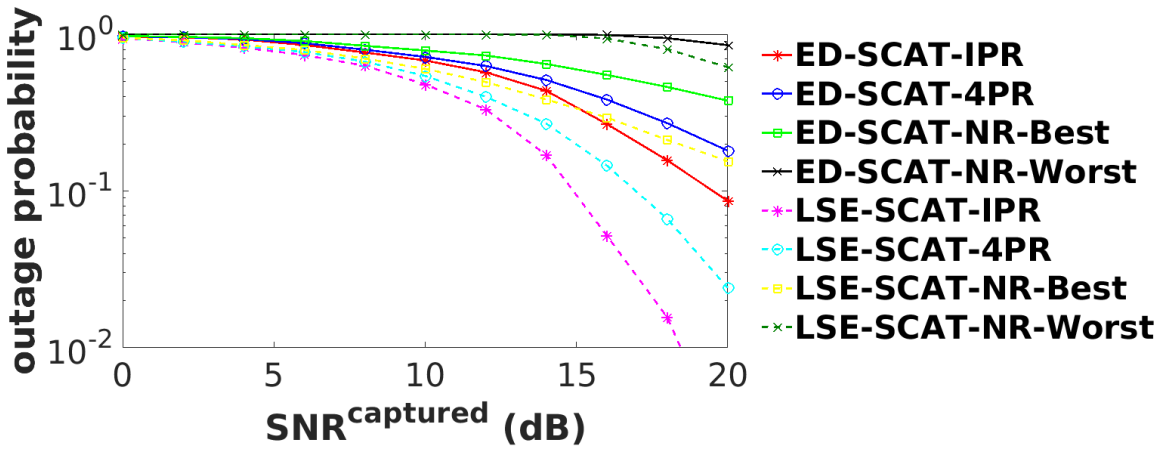

Figure 3-13 BER simulated for the ED and LSE detectors as a function of the SNR

3.6. IMPACT OF THE ANTENNA RADIATION PATTERN

In this section we compare the performance of the SSR antenna, the XPOL antenna, and the 4PR rotating dipole antenna. We consider a PCS coding scheme and an LSE detector.

3.6.1. Experimental Setup

Table 3-4 Antenna configurations.

Antenna	***Coding Scheme***	***Channel Modeling***	***Number of receiving antenna***
SRR	PCS	Experimental	3
CrossPolar	PCS	Experimental	3
Dipole 4PR	PCS	Simulation	1

The configuration setups studied in this section are reported in Table 3-4. The propagation channel is extracted from measurements conducted in a reverberation chamber. The reverberation chamber has the advantage to provide a time invariant environment and multipath.

Figure 3-14 and Figure 3-15 illustrate the experimental setup of the system for the two compact reconfigurable antennas. For each antenna we consider 4 polarization patterns as depicted in Figure 3-16, Figure 3-17, Figure 3-18. Based on the PCS coding scheme, the tag switch between two polarization patterns in order to transmit bit 1 and 0. We evaluate the performance depending on the two chosen patterns for each antenna.

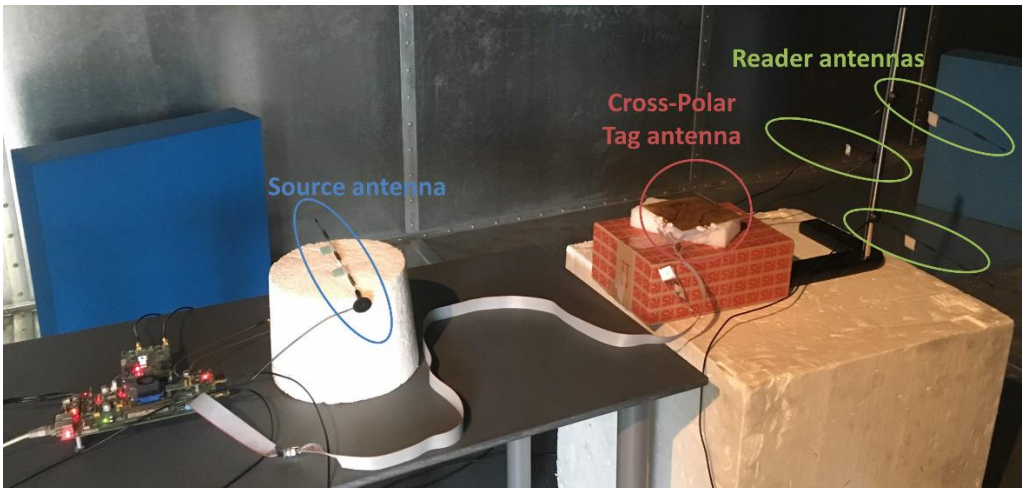

Figure 3-14 Experimental setup for the XPOL antenna.

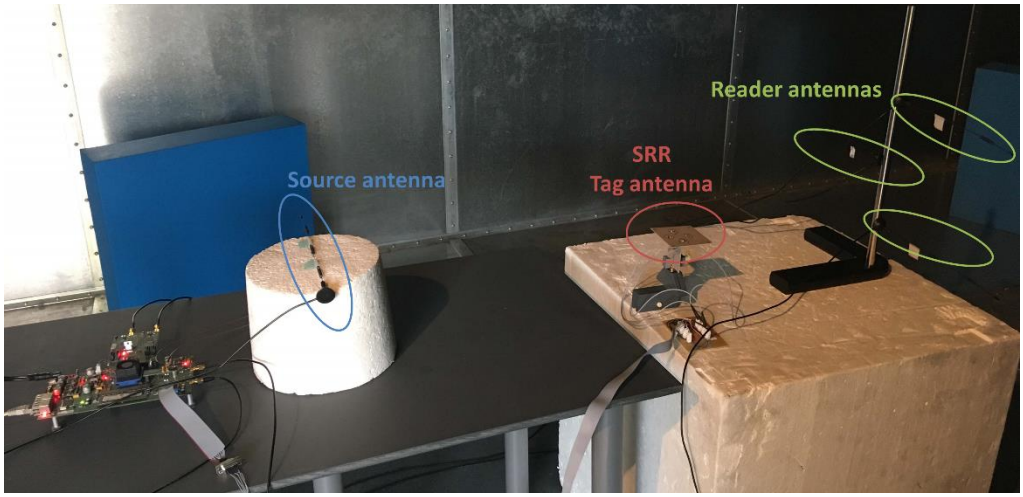

Figure 3-15 Experimental setup for the SRR antenna.

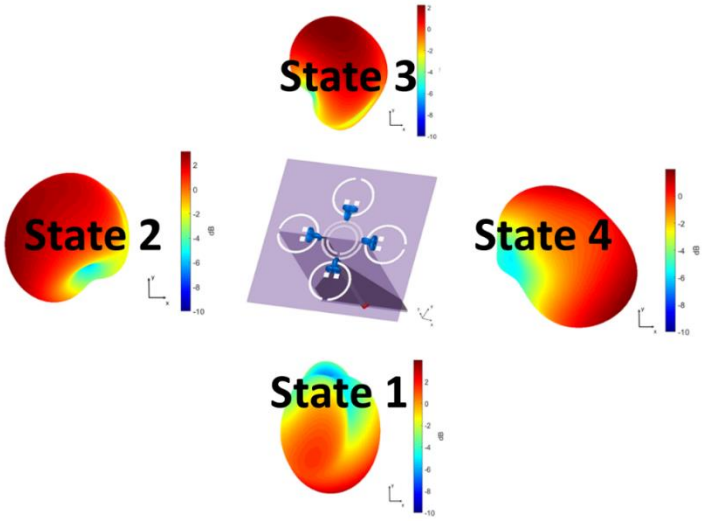

Figure 3-16 SRR polarization patterns according to the state number.

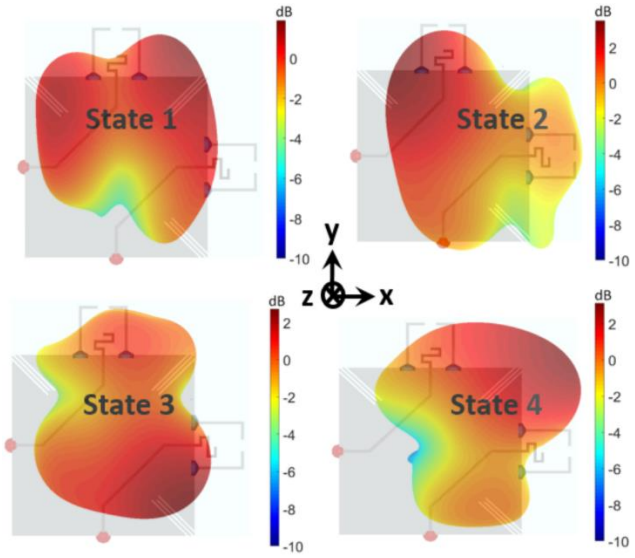

Figure 3-17 XPOL polarization patterns according to the state number.

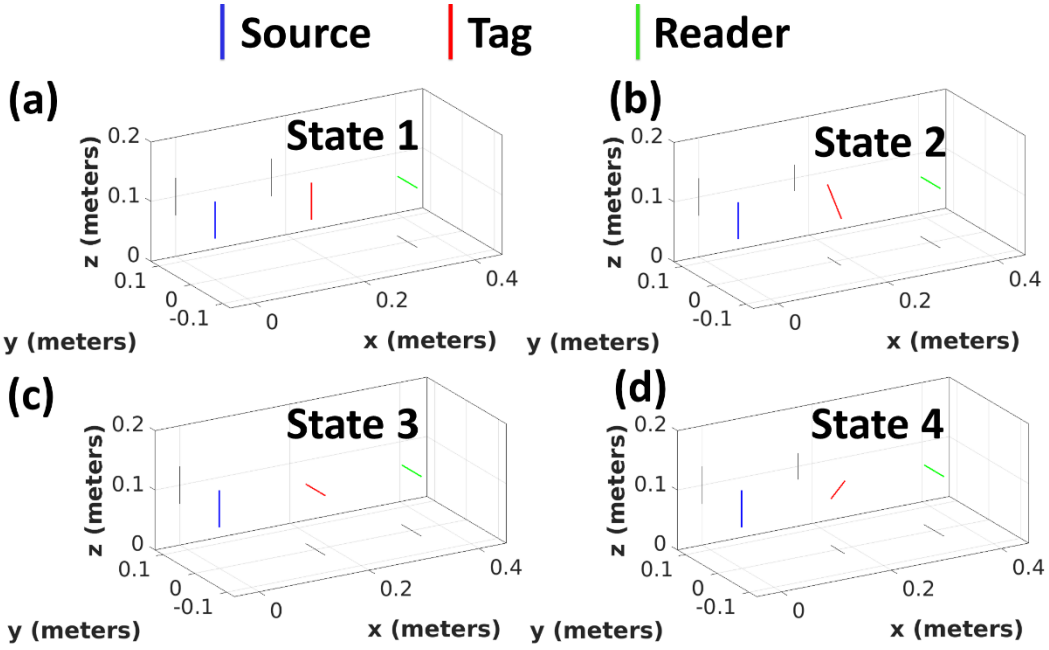

Figure 3-18 4PR polarization orientation according to the state ($\phi^T = 0°, 45°, 90°, 135°$, $\theta^T = 90°$).

Table 3-5 Configuration of the PCS based on the state of the antenna.

Configuration	**2:1**	**3:1**	**4:1**	**3:2**	**4:2**	**4:3**
Bit 1	State 2	State 3	State 4	State 3	State 4	State 4
Bit 0	State 1	State 1	State 1	State 2	State 2	State 3

3.6.2. Results

In this section, we evaluate numerically the BER as a function of the $SNR^{captured}$. The results are reported in Figure 3-19,Figure 3-20, Figure 3-21.

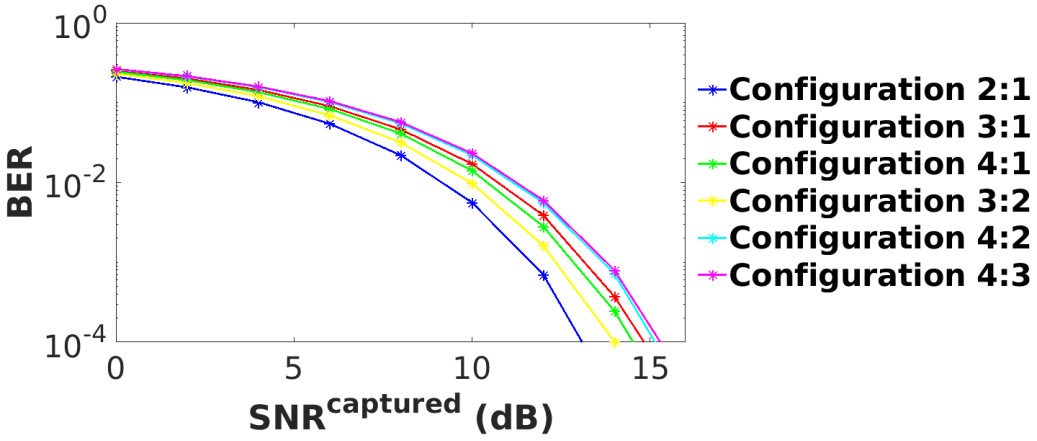

Figure 3-19 BER rate for a the different configurations of the PCS of the SRR antenna.

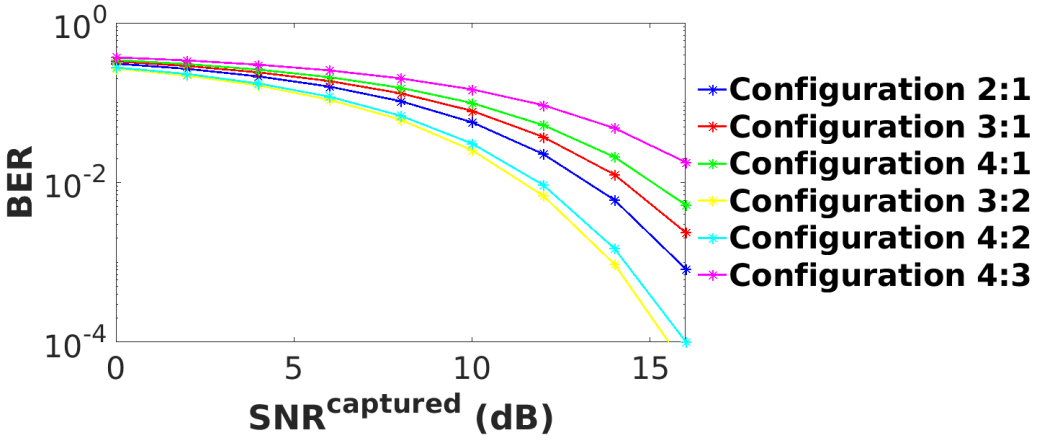

Figure 3-20 BER rate for a the different configurations of the PCS of the XPOL antenna.

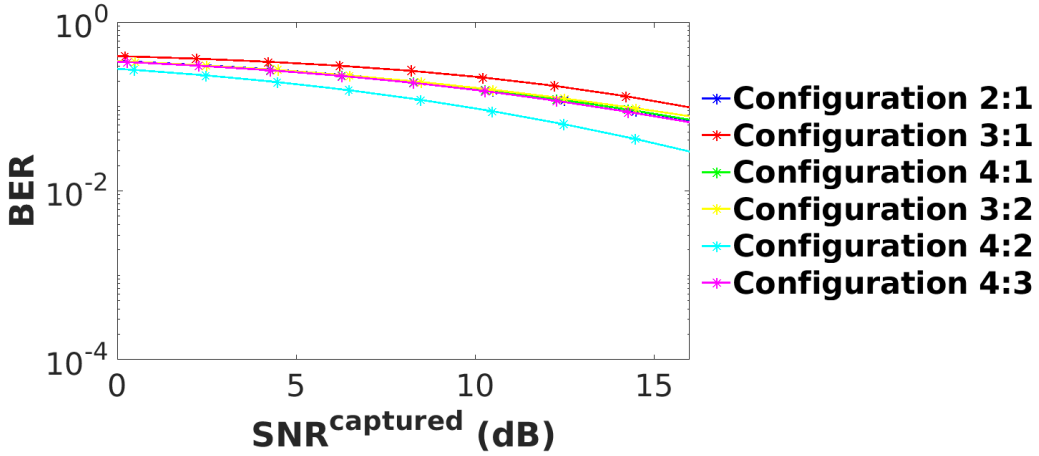

Figure 3-21 BER rate for the different configurations of the PCS of the 4PR antenna.

From the figures, we evince that the performance depends on the selected polarization patterns. For example, it is easier for the LSE detector to detect the bits if the two patterns are uncorrelated.

From Figure 3-19, we observe that the best configuration for the SRR corresponds to the states 2 and 1, which have an envelope correlation coefficient lower than 0.1 [69]. Also, the configuration with the states 3 and 2 is one of the worst and has a correlation coefficient close to 0.5 [69].

From Figure 3-20, we observe that the BER performance of the XPOL depends on the configuration of the chosen states. The best configuration is obtained for the states 3 and 2, and for the states 4 and 2. In both cases, we observe that these states have completely opposed pattern directions (see Figure 3-17). This property, in fact, reduces the correlation between the patterns and the states are more easily detectable.

From Figure 3-21, we observe that the performance of the 4PR tag is worse compared to the XPOL and the SRR tags. This can be explained by the fact that the patterns of the dipole antennas are more correlated. We can note that the configuration with the states 4 and 2 has the best performance because these two states correspond to the best orientations of the dipole (see Section 3.3.1 and because these states are cross-polarized (Figure 3-18).

In conclusion, our analysis shows that the SRR antenna is the best antenna, thanks its low inter-patterns correlation properties

3.7. CONCLUSION

In this chapter, we have shown the advantages of using a polarization reconfigurable tag in AmBC systems. Such a tag takes advantages of different polarizations in order to improve the robustness of the communication against direct source-to-reader interference. In this preliminary study, we proposed to use a very simple model of polarization reconfigurable tag to focus our study on polarization. In our model, the compact reconfigurable antenna is modelled by a rotating dipole. We have proposed a simple method to determine the tag orientation that maximizes the performance in a LOS sight environment. We have made a first numerical assessment of the improvement in terms of outage probability, obtained with a polarization reconfigurable tag in both a LOS and richly scattering environments, by simulation and experiments. With the aid of analysis, simulations, and experiments, we have shown that a realistic 4-polarization reconfigurable tag provides performance that is similar to an ideal tag having 20x polarization states.

Chapter 4

Ambient backscatter-friendly 5G networks

In this chapter, we propose to study the AmBC systems within the 5G network. More specifically we propose to improve the performance of the ambient backscatter system by using 5G mMIMO equipment. We consider the uplink and downlink configuration of 5G communication, where the ambient source of signal can be either the base station (downlink) or the smartphone (uplink).

In the section 4.1, we consider a downlink scenario and we propose to use the base station as the source to beamform the ambient signal to create “hot spots for tags” with very high power and “good reception spots for readers”. We assess the performance of the system for three different precoders each having a different impact on the backscattering signal.

Secondly in section 4.2, we investigate the uplink configuration where the mMIMO antenna is used as the reader to enhance the detection of the backscattered message from the tag. We exploit the channel spatial diversity with a reader equipped of 64 antenna elements. Experimentally, we assess the AmBC in an uplink scenario in an anechoic chamber. We evaluate the performance of the system using a least square error estimator to detect the state of the tag.

4.1. CREATING HOT SPOTS FOR TAGS AND GOOD SPOTS FOR READERS

4.1.1. Introduction

In this section we consider a downlink scenario, where the source of signal is a mMIMO antenna. In the literature, such multi-antenna source have been envisaged and to overcome the limitations of AmBC, [122] proposes to use transmit beamforming at the source side and a joint-detection of the source and the tag signals at the reader side. In [122], it is assumed that the source perfectly knows the three channels: the tag-to-reader, the source-to-tag and the source-to-reader channel. Then, the source computes a beamformer that optimizes the detection of the tag, under a constrain (a target detection probability of the source signal). The limit of this technique is that the reader is highly complex and the acquisitions of the three channel state information at the

source side, seems very difficult in practice, especially, with an energy harvesting tag.

5G base stations can perform beamforming thanks to mMIMO antennas composed of several dozens, to a few hundreds of antenna elements [123],[124]. In the field trials conducted in [124], sounding reference signals (SRS) [125] are sent by the mobile device in the uplink direction to enable the BS to acquire the channel state information at the transmission (CSIT) side, channel reciprocity is exploited to perform beamforming.

In this section, we propose to use 5G networks and devices to create "hot spots for tags" with very high RF power and "good reception spots for readers" with a four-step approach. We consider two types of good reception spots: a "quiet spot" with very weak source-to-reader interference; and a "coherent spot" with source-to-reader interference, this interference being built to be coherent (i.e. in phase) with the backscattered signal. During a first step illustrated in Figure 4-1-a), the locations of the spots are indicated by visual signs such as panels or stickers. During a second step, illustrated in Figure 4-1-b), 5G "training devices" send SRS to the network to enable the network to acquire the CSIT . During a third step, illustrated in Figure 4-1-c), the network performs MRT beamforming (to create a hot spot for the tag) or ZF beamforming (to create a hot spot for the tag and a quiet spot for the reader simultaneously) [126], or a new coherent combining (CC) beamforming (to create a hot spot for the tag and a coherent spot for the reader). Once the hot spot and the good reception spot are created, the 5G devices can be withdrawn and replaced by a tag and a reader, respectively, during a fourth step illustrated in Figure 4-1-d) and Figure 4-1-e), for ZF and CC, respectively. The tag is then strongly illuminated by the 5G source and better detected by the reader. In the case where the reader is on a quiet spot, the tag-to-reader signal is free of direct 5G source interference. In the case where the reader is on a coherent spot, the tag-to-reader signal coherently combines with the direct 5G source interference. In this latter case the source must transmit successively different phase shifted beams and the reader must analyze the received signal for each beam and feedback the beam index, which maximizes the performance, to the source. Thanks to these methods, the tag and reader remain advantageously simple, low cost and low power (for the tag at least), as they do not need to send SRS or to make complex joint detection. The reader can remain a simple energy detector and performance depends on the difference of power between the backscattering and transparent states. Even in the case of CC beamforming, the reader only needs to feed back a beam index.

There are two important requirements though. First, such scheme requires the channel to be stable between the time when the smartphone performs the sounding and the time when the tag and reader communicates with each other. Such stability has been observed experimentally for mMIMO channels in [83][84]. Secondly, the channel must be highly richly scattering with strong angular. This assumption ensures that applying the ZF, MRT or CC precoder does not reduce the broadcast signal power received by legacy devices, and that the beamforming gain is important.

The section is organized as follows: sub-section 4.1.2 presents our system model, sub-section

4.1.3 presents simulation results in a richly scattering environment (with a Rayleigh channel model) and section 4.1.4 concludes this study.

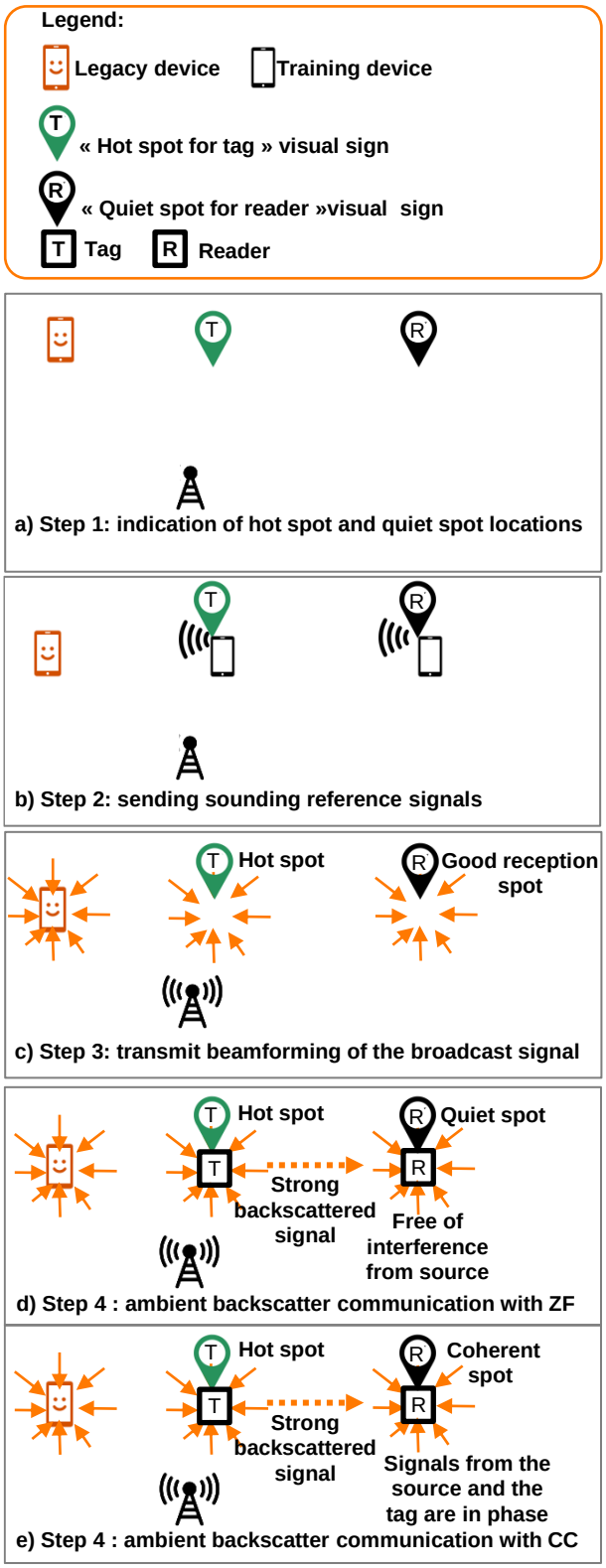

Figure 4-1 Proposed system.

4.1.2. System Model

4.1.2.1. *Spatially correlated channel model including backscattering*

As shown in Figure 4-2, we consider a system composed of a source (S), a tag (T), a reader (R) and a legacy device (D). The variable d^{SR} (respectively $d^{\mathrm{ST}}, d^{\mathrm{TR}}$) defines the distance between S and R (respectively S and T, T and R).

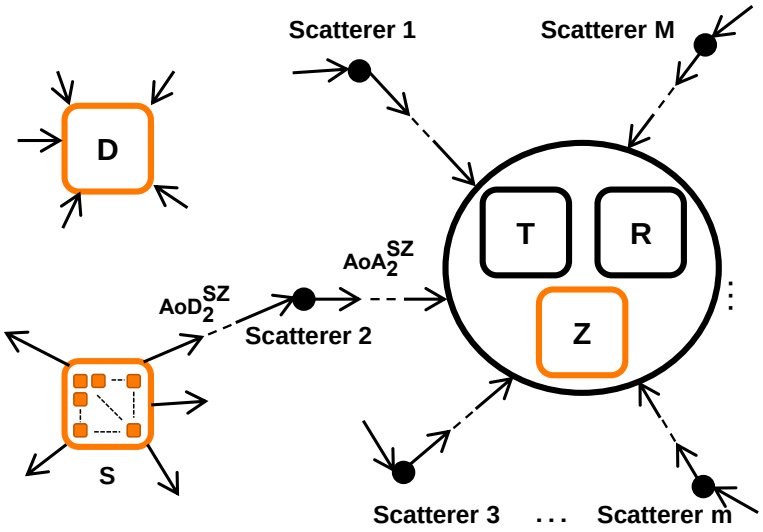

Figure 4-2 Propagation model.

The source is equipped with a mMIMO antenna composed of K transmit antennas. A uniform planar antenna array (with $k^{(1)}$ lines, $k^{(2)}$ columns and $k^{(1)}k^{(2)} = K$) is considered. The source illuminates the tag and the reader through a complex multipath propagation environment due to scatterers.

As illustrated by Figure 4-2, we assume that the source is located far from the tag, the reader and the device. In the model we consider that the tag and the reader are closed to each other and experience a spatially correlated channel. On the contrary, we consider that the legacy device is very far from the tag and the reader. As a consequence, the source-to-legacy-device channel is assumed to be uncorrelated with the source-to-reader and source-to-tag channels.

We consider a multi-carrier waveform as in 5G standard [125]. We assume that the channel is frequency flat on a subcarrier and therefore study the system on a subcarrier basis. With this assumption, the channel can be modeled by a complex coefficient. Let $\mathbf{h}^{\mathrm{SZ}} \in \mathbb{C}^{1\times K}$ be the vector of the K coefficients of the small scale fading channels between an arbitrary point in space Z (in the proximity of the tag and the reader) and the K antennas of the source. We model the channel by a Rayleigh channel model with M paths. For each path $m \in [1, \dots, M]$, a planar wave leaves the source with a random angle of departure AoD_m^{ST}, is scattered by the scatterer m, and finally hits the point Z with a random angle of arrival AoA_m^{ST}. The wave has a random initial phase ϕ_m and a normalized Gaussian complex gain α_m. AoD_m^{ST}, AoA_m^{ST} and ϕ_m are uniformly distributed

in [0, 2π] and $\mathrm{E}[|\alpha_m|^2] = \frac{1}{M}$. With these assumptions, the expression of $\mathbf{h}_k^{\mathrm{SZ}}$, the k[th] element of $\mathbf{h}^{\mathrm{SZ}}$, is given by:

$$\mathbf{h}_k^{\mathrm{SZ}} = \sum_{m=1}^{M} \alpha_m \mathrm{e}^{-\mathrm{j}\frac{2\pi f \theta_{k,m}}{c} + \phi_m} \tag{4-1}$$

where, c is the light velocity, f is the carrier frequency, $(x_{\mathrm{k}}^{\mathrm{S}}, y_k^{\mathrm{S}})$ are the Cartesian coordinates of the source antenna k, $(x^{\mathrm{Z}}, y^{\mathrm{Z}})$ are the Cartesian coordinates of the point Z relatively to a position in the area including the tag and reader, and $\theta_{k,m}$ is a path difference given by: $\theta_{k,m} = (x_k^{\mathrm{S}} - x_1^{\mathrm{S}})\cos(AoD_m^{\mathrm{SZ}}) + (y_k^{\mathrm{S}} - y_1^{\mathrm{S}})\sin(AoD_m^{\mathrm{SZ}}) + x^{\mathrm{Z}}\cos(AoA_m^{\mathrm{SZ}}) + y^{\mathrm{Z}}\sin(AoA_m^{\mathrm{SZ}})$.

From equation (4-1), we can deduce the vectors $\mathbf{h}^{\mathrm{SR}}, \mathbf{h}^{\mathrm{ST}} \in \mathbb{C}^{1\times \mathrm{K}}$, of the source-to-reader and the source-to-tag small-scale fadings, respectively, by replacing Z by R and T, respectively.

Free space propagation is considered between T and R and modeled with the Friis Formula as T and the R are supposed to be closed to each other. With these assumptions, the tag-to-reader channel $h^{\mathrm{TR}} \in \mathbb{C}$ is given by:

$$h^{\mathrm{TR}} = \frac{\lambda}{4\pi d^{\mathrm{TR}}} \mathrm{e}^{-\mathrm{j}\frac{2\pi d^{\mathrm{TR}}}{\lambda}} \tag{4-2}$$

The total signal received by the reader is the sum of the direct signal from the source and the signal from the source backscattered by tag. We obtain the following expression of the equivalent channel $\mathbf{h}^{\mathrm{eq}} \in \mathbb{C}^{1\times K}$ between S and R (after propagation, including backscattering):

$$\mathbf{h}^{\mathrm{eq}} = \sqrt{G}(\gamma h^{\mathrm{TR}} \mathbf{h}^{\mathrm{ST}} + \mathbf{h}^{\mathrm{SR}}) \tag{4-3}$$

where, $G \in \mathbb{R}^+$ is the long-term average propagation gain due to slow shadow fading and the distance. This term also includes the antenna gains, differential cross sections and impedances of the system that remain constant in the model. γ corresponds to the modulation factor of the tag. $\gamma \in [0,1]$ takes two distinct values: γ^{ON} when the tag is backscattering and γ^{OFF} when the tag is transparent.

4.1.2.2. *Precoders*

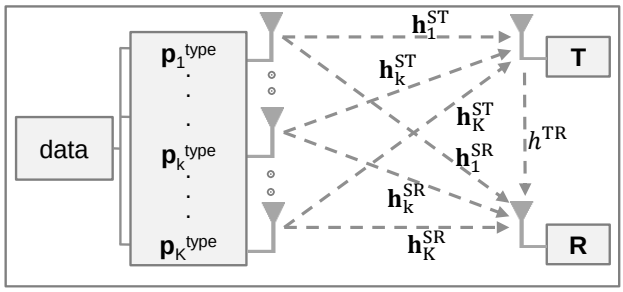

Figure 4-3 Precoder principle.

As introduced in I, we propose to use precoders exploiting the knowledge of the channels $\mathbf{h}^{\mathrm{SR}}$

and $\mathbf{h}^{\mathrm{ST}}$ (estimated by the source thanks to pilots sent by the training device), to improve the ΔSNR metric. We emphasize that in our proposed schemes, $\mathbf{h}^{\mathrm{TR}}$ remains unknown, contrary to the solution given in [122].

As illustrated in Figure 4-3, we consider and compare the following four different types of precoder $\mathbf{p} \in \mathbb{C}^{\mathrm{K}\times 1}$:

- the reference precoder $\mathbf{p}^{\mathrm{REF}}$ (no precoding);
- the MRT precoder $\mathbf{p}^{\mathrm{MRT}}$;
- the ZF precoder $\mathbf{p}^{\mathrm{ZF}}$;
- the CC precoder $\mathbf{p}^{\mathrm{CC}}$.

The reference (REF) precoder is defined by $\mathbf{p}_1^{\mathrm{REF}} = 1$, with $K = 1$ antenna.

For all next precoders, $K > 1$ is considered.

The expression of the MRT precoder is given by $\mathbf{p}^{\mathrm{MRT}} = \alpha^{\mathrm{MRT}}(\mathbf{h}^{\mathrm{ST}})^{\dagger}$, where $(.)^{\dagger}$ is hermitian operation and α^{MRT} is a normalizing factor such that $\|\mathbf{p}^{\mathrm{MRT}}\|^2 = 1$, where $\|.\|^2$ is the Frobenius norm. The precoder $\mathbf{p}^{\mathrm{MRT}}$ creates a maximum of power or "hot spot" on the tag.

The ZF precoder $\mathbf{p}^{\mathrm{ZF}}$ is determined in several steps. First the channel matrix $\mathbf{H} \in \mathbb{C}^{2\times \mathrm{K}}$ is defined as follows:

$$\mathbf{H} = \begin{bmatrix} \mathbf{h}_1^{\mathrm{ST}} & \dots & \mathbf{h}_K^{\mathrm{ST}} \\ \mathbf{h}_1^{\mathrm{SR}} & \dots & \mathbf{h}_K^{\mathrm{SR}} \end{bmatrix}$$

Then, the following zero forcing matrix is computed:

$$\mathbf{Q} = \mathbf{H}^{\dagger}(\mathbf{H}\,\mathbf{H}^{\dagger})^{-1} \tag{4-4}$$

Finally, $\mathbf{p}^{\mathrm{ZF}}$ is extracted from $\mathbf{Q}$ as follows: $\mathbf{p}_k^{\mathrm{ZF}} = \alpha^{\mathrm{ZF}}\mathbf{Q}_{k,1}$ for $k = 1 \dots K$, with α^{ZF} is a normalizing factor such that $\|\mathbf{p}^{\mathrm{ZF}}\|^2 = 1$. The precoder $\mathbf{p}^{\mathrm{ZF}}$ creates a maximum of power or "hot spot" on the tag and a zero of power or "quiet spot" on the reader.

The CC precoder $\mathbf{p}^{\mathrm{CC}}$ is based on ZF precoder to which we apply a phasing matrix $\mathbf{T}$, a power allocation matrix $\mathbf{D}$ and combining matrix $\mathbf{S}$:

$$\mathbf{p}^{\mathrm{CC}} = \alpha^{\mathrm{CC}} \times \mathbf{Q} \times \mathbf{T} \times \mathbf{D} \times \mathbf{S} \tag{4-5}$$

With, $\mathbf{T} = \begin{bmatrix} 1 & 0 \\ 0 & e^{j\varphi} \end{bmatrix}$, $\mathbf{D} = \begin{bmatrix} \delta & 0 \\ 0 & \sqrt{1-\delta^2} \end{bmatrix}$ and $\mathbf{S} = \begin{bmatrix} 1 \\ 1 \end{bmatrix}$

α^{CC} is a normalizing such that $\|\boldsymbol{p}^{CC}\|^2 = 1$. The precoder $\boldsymbol{p}^{CC}$ creates a hot spot on the tag and another hot spot on the reader. The signal on the reader is phased-shifted in order to combine coherently source and tag signals at the reader location. As the power is shared between the two hot spots, we use $\boldsymbol{D}$ matrix to optimally allocate this power and maximize the performance. Optimal precoder is determined by optimizing the phase-shift variable φ and the power allocation

variable δ.

4.1.2.3. *Performance metrics*

The amplitude of the signal received by the reader is given by:

$$A(\gamma) = |\mathbf{h}^{\mathrm{eq}}\mathbf{p}|\sqrt{P_u} = \left|(\gamma h^{\mathrm{TR}}\mathbf{h}^{\mathrm{ST}} + \mathbf{h}^{\mathrm{SR}})\mathbf{p}\right|\sqrt{P_u} \tag{4-6}$$

where P_u is the transmit power of the source. We define P_{noise} as the receiver noise power at the reader side and $SNR^{\mathrm{illum}} = \frac{GP_u}{P_{noise}}$ the "illumination" signal to noise ratio. SNR^{illum} reflects the average amount of illumination in the area located around T and R, from the source (independently from precoding and small-scale fading effects).

The BER metric of the energy detector depends on the amplitude contrast ΔA between the state when the tag is backscattering and the state when the tag is transparent as follows:

$$BER = \frac{1}{2}erfc\left(\frac{\Delta A}{\sqrt{P_{noise}}}\right) \tag{4-7}$$

where,

$$\Delta A = \left|A^{\mathrm{ON}} - A^{\mathrm{OFF}}\right| \tag{4-8}$$

and A^{ON} (A^{OFF}, respectively) is the value of the signal amplitude $A(\gamma)$ at the reader, when $\gamma = \gamma^{\mathrm{ON}}$ ($\gamma = \gamma^{\mathrm{OFF}}$, respectively), i.e. when the tag is backscattering (transparent, respectively). In the rest of the chapter we consider $\gamma^{\mathrm{ON}} = 1$ and $\gamma^{\mathrm{OFF}} = 0$, then the expression of the amplitude contrast is:

$$\Delta A = \left|\left|(h^{\mathrm{TR}}\mathbf{h}^{\mathrm{ST}} + \mathbf{h}^{\mathrm{SR}})\mathbf{p}\right| - \left|\mathbf{h}^{\mathrm{SR}}\mathbf{p}\right|\right|\sqrt{P_u} \tag{4-9}$$

In the case of CC, to obtain the optimal matrix **T** and **D**, the BS determines the phase-shift φ^{max} and the power allocation δ^{max} that maximize ΔA, in two steps. First, the BS transmits successively pilots with different $\mathbf{p}^{\mathrm{CC}}$ precoders based on different φ and δ values and the reader measures the corresponding ΔA. Second, the reader feeds back the index of the optimal precoder to the BS. Finally the BS transmits with the optimal precoder indicated by the reader.

To meet a given target quality of service (QoS) associated to a given target BER, BER^{target}, ΔA must verify: $\Delta A > \Delta A^{\mathrm{target}}$ where $\Delta A^{\mathrm{target}} = (erfc)^{-1}(2BER)$ is the target amplitude difference between the two states.

4.1.2.4. *Metric measuring the impact on legacy device*

Regarding the legacy device D, we assume that the legacy D is uncorrelated and far from R and T. The coefficients of the vector $\mathbf{h}^{\mathrm{D}} \in \mathbb{C}^{1\times K}$ of the source-to-device channel are hence generated as a Rayleigh channel model, independently from $\mathbf{h}^{\mathrm{SR}}$ and $\mathbf{h}^{\mathrm{ST}}$.We assume that the legacy device D under the average radio conditions (or illumination by the source) as T and R.

With these assumptions, the received SNR at the device side is given by:

$$SNR^{\mathrm{D}} = \left|\sqrt{G}\mathbf{h}^{\mathrm{D}}\mathbf{p}^{type}\right|^2 \frac{P_u}{P_{noise}} = |\mathbf{h}^{\mathrm{D}}\mathbf{p}^{type}|^2 SNR^{\mathrm{illum}} \quad (4\text{-}10)$$

4.1.3. Simulation Results

This section presents simulation results based on the model depicted in II, with the parameter setting given in Table 4-1.

Table 4-1 Simulation Parameters.

Parameters	***Details***	***Value***	***Units***
M	Number of Taps	100	
$k^{(1)}$	Number antenna elements per line	8	
$k^{(2)}$	Number antenna elements per colums	8	
K	Number of antenna elements	64	
f	Frequency	2.4	GHz
SNR^{illum}	Average amount of illumination received from the source	24	dB
BER^{target}	Target Bit Error Rate	10^{-3}	

We first present some visual results for a determined model and then more in depth and general statistical results.

4.1.3.1. *Visualisation of "hot spot" for tag and "quiet spot" for reader thanks to spatial maps of SNR metrics*

In this section, we consider fixed locations of the source, the reader and the tag, one sample of the random propagation channel model and a fixed average illumination SNR^{illum} of 24dB (as defined in section 4.1.2.

We then compute, the SNR metrics defined in section 4.1.2, as functions of the (x,y) coordinates of the point Z and visualize them into spatial maps, for each precoder (REF, MRT, ZF and CC, namely) . Figure 4-4 illustrates the spatial maps of $\frac{A^{\mathrm{OFF}}}{\sqrt{P_{noise}}}$ and shows to which extent the tag and its surrounding area is illuminated by the source relatively to the noise. Figure 4-5 illustrates the spatial maps of $\frac{A^{\mathrm{TR}}}{\sqrt{P_{noise}}} = \left|h^{\mathrm{TR}}\mathbf{h}^{\mathrm{ST}}\mathbf{p}^{type}\right| \frac{\sqrt{P_u}}{\sqrt{P_{noise}}}$ and shows the amplitude level of signal backscattered by tag. Finally, Figure 4-6 illustrates the spatial maps of $\frac{\Delta A}{\sqrt{P_{noise}}}$ maps and shows the locations where the reader can detect the tag with the target QoS (these are locations where $\Delta A > \Delta A^{target}$). $\frac{\Delta A^{target}}{\sqrt{P_{noise}}}$ is represented as the level where the scale color changes. Dark colors (blue) indicate locations where the target QoS cannot be reached and light colors (yellow or red) where QoS can be achieved.

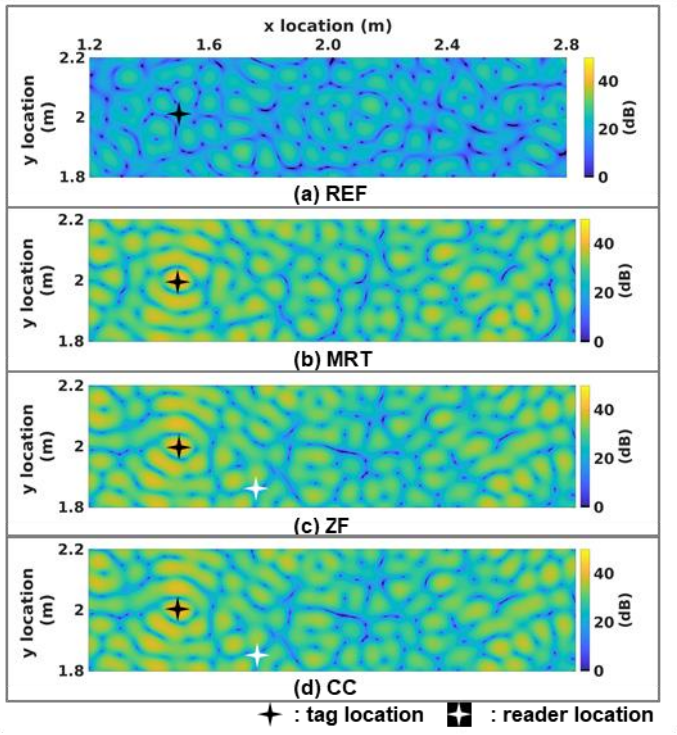

Figure 4-4 Maps of $\frac{A^{ON}}{\sqrt{P_{noise}}}$.

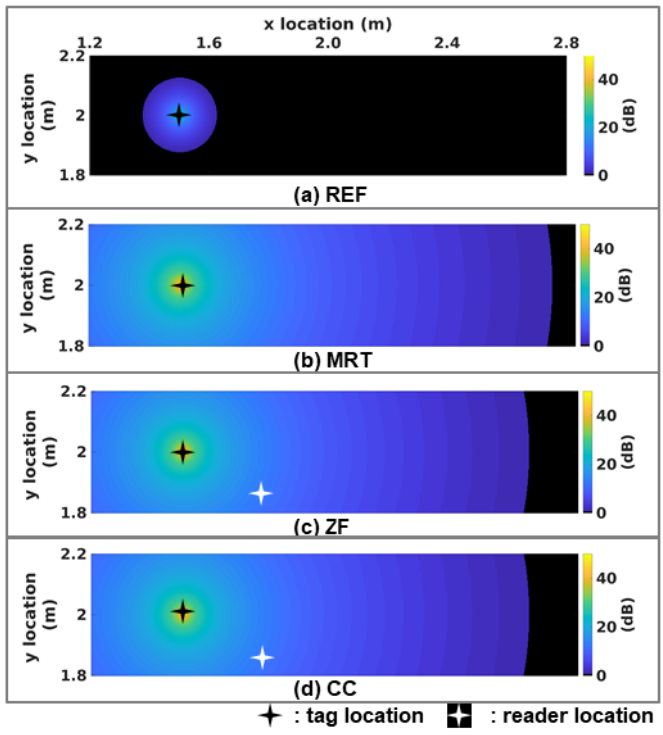

Figure 4-5 Maps of $\frac{A^{TR}}{\sqrt{P_{noise}}}$.

Thanks to Figure 4-4, Figure 4-5 and Figure 4-6 we can make a first comparison between the four considered precoders. With REF, due to the weak illumination of the tag observed in Figure

4-4-a), the backscattered signal observed in Figure 4-5-a) is weak, and consequently, the locations observed in Figure 4-6-a) where the reader can detect the tag are very rare. With MRT, thanks to the strong illumination (the "hot spot") of the tag observed in Figure 4-4-b), the backscattered signal observed in Figure 4-5-b) has a large coverage. However, the locations observed in Figure 4-6-b), where the reader can detect the tag, are randomly distributed. At a particular target location of the reader, the target ΔA is not guaranteed.

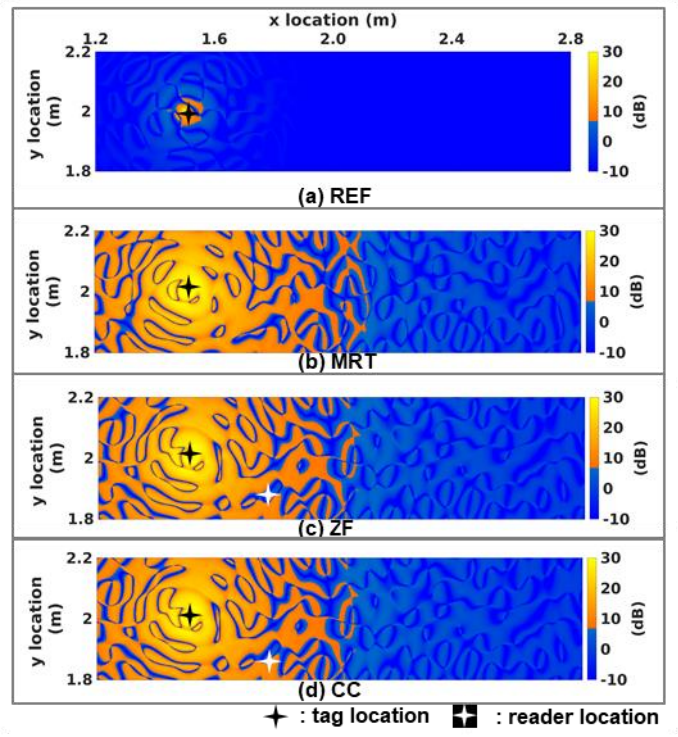

Figure 4-6 Maps of $\frac{\Delta A}{\sqrt{P_{noise}}}$.

With ZF, the "hot spot" on the tag observed in Figure 4-4-c) is very slightly weaker than in MRT. Hence, the coverage of the backscattered signal observed in Figure 4-5-c) is also slightly weaker than in MRT. This is due to the fact that ZF spends some of its power to cancel the source signal on the reader location. However, thanks to this "quiet spot" for reader that can be observed Figure 4-4-c), the target ΔA is met at the target location of the reader as illustrated in Figure 4-6-c). Finally with CC, we have plotted the maps for $\varphi = \varphi^{max}$ and $\delta = \delta^{max}$ the phase-shift and the power allocation that maximizes ΔA at the reader location. In Figure 4-4-d), the spot of the tag and the reader are coherent. As the source-reader signal is phased-shifted, the backscattered signal combines with the source signal and improves the detection. We observed in Figure 4-6-d) a good detection spot where the reader can easily detect the tag.

The previous results have been obtained for a given random sample of the Rayleigh channel model. To get a more general insight on the performance, we propose to visualize statistics over 100 random samples of model parameters. SNR^{illum}, the locations of the source and the tag still remain fixed. However, the location of the reader is variable and the ZF and CC beamforming

"good reception spot" is adapted to the location of the reader. For each location of the reader, given by the Cartesian coordinates $(x^{\mathrm{R}}, y^{\mathrm{R}})$, we define $F^{\mathrm{O}}(x^{\mathrm{R}}, y^{\mathrm{R}})$, as the probability that $\Delta SNR > \Delta SNR^{\mathrm{target}}$, i.e. that the reader detects the tag with the target QoS. Figure 4-7 illustrates F^{O} (in percentage) as a function of $(x^{\mathrm{R}}, y^{\mathrm{R}})$.

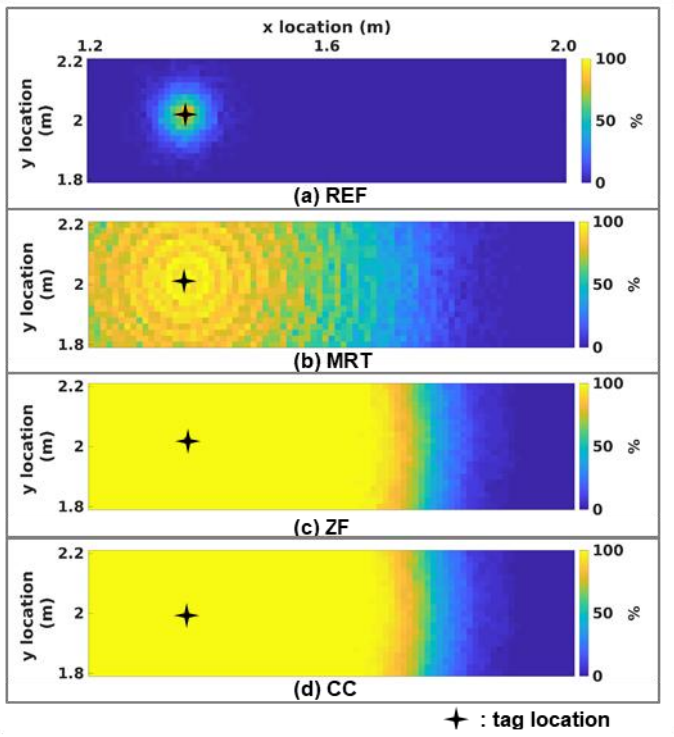

Figure 4-7 Statistical maps, evaluating the condition $\Delta A > \Delta A^{target}$ for 100 random samples of the Rayleigh channel model.

As expected, the reference case is the worst. MRT provides a good coverage, however, coverage the target contrast cannot be guaranteed. ZF and CC guaranty a continuous coverage inside a given range thanks to the quiet spot or coherent combining of the backscattered signal at the reader side.

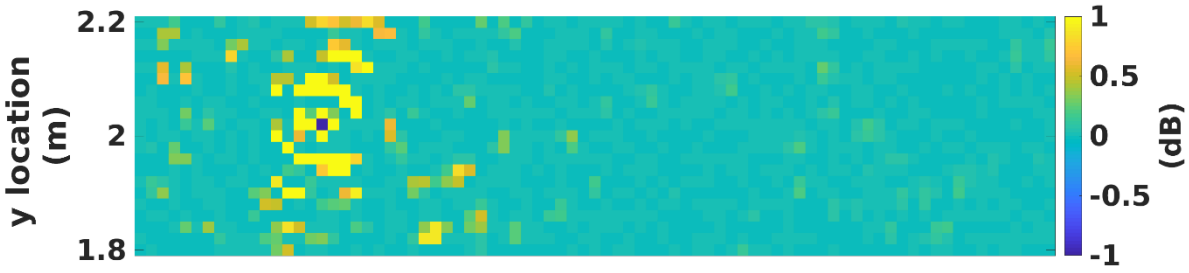

Figure 4-8 Map of $\Delta A^{cc} - \Delta A^{ZF}$

The CC is very close to the ZF in terms of performance. We observe in the Figure 4-8 the difference of contrast between the ZF and the CC precoders for one of the set of random samples We observe that CC slightly outperforms the ZF, the contrast of the CC precoding is better than

the ZF contrast. Thanks to the phase shift and the power allocation that are tuned, the CC precoding is more optimized, yet it is more complex to implement as it requires a feedback from the reader.

4.1.3.2. *Impact on the legacy device*

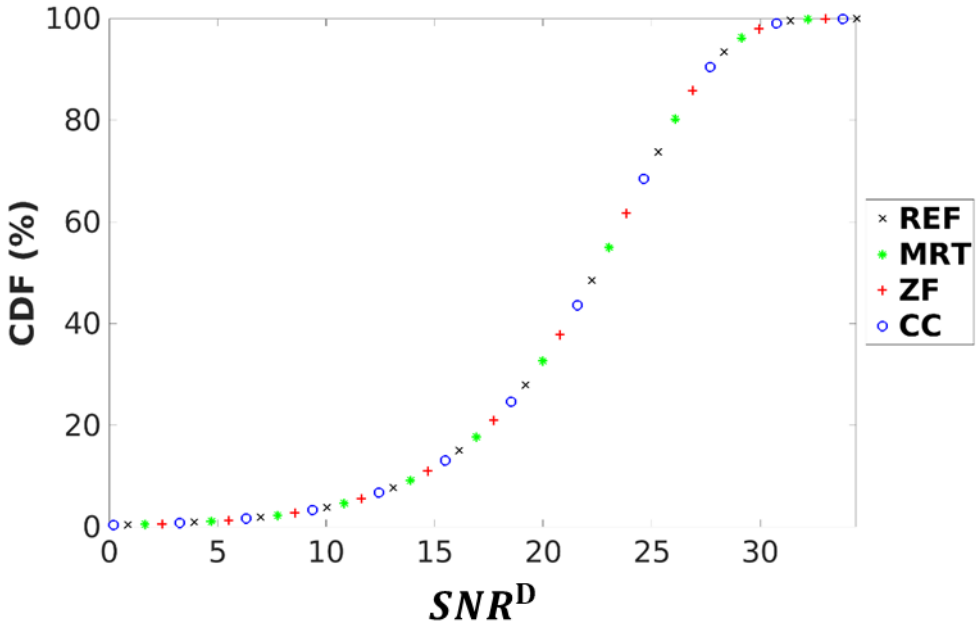

Figure 4-9 CDF of the signal received by the legacy.

Furthermore, Figure 4-9 illustrates the cumulative distribution function (CDF) of the SNR^{D} at the legacy device side in four cases: when REF, MRT, ZF and CC precoders are used by the source. No significant difference between the four curves is observed, which means that legacy device is not impacted by the precoder, at least under Rayleigh propagation. In other terms, a backscatter-friendly network that precodes its signals (initially intended towards legacy devices) to help backscatter communications, does not degrade its legacy communications.

4.1.4. Conclusion

In this section, we have shown a practical method that could be implemented to improve backscatter communications in 5G networks considering a downlink scenario with a mMIMO antenna. This method improves the tag-to-reader range and the detection probability. Helped by training devices, the mMIMO base station acquires a partial knowledge of the channel (only the source-to-tag and the source-to-reader channels) and creates a hot spot to be later used by a tag and a quiet spot to be later used by a reader. We have shown that MRT precoder improve the tag-to-reader communication distances, however the detection probability target is reduced. ZF precoder ensures a good of detection probability of the tag, with the target quality of service, for a given tag-to-reader distances by creating a hot spot on the tag and a quiet spot on the reader. CC similarly to ZF, ensures the QoS for a given tag-to-reader distance thanks to the coherent

combining of the backscattered signal with the source signal. Moreover we have also shown that precoding has no impact on legacy devices communicating with the 5G network, in Rayleigh environment at least.

4.2. EXPERIMENTAL EVALUATION OF AMBC WITH A 5G MMIMO READER

4.2.1. Introduction

A 5G mMIMO antenna has been proposed as a smart source for AmBC communications in the previous section. In downlink configuration, the source can beamform the signal to create a hot spot on the tag and to avoid interference at the reader side. These promising results were obtained through simulations with simple models. In this system the reader was composed of one antenna and was not exploiting the receive diversity to detect the tag.

In this section, we propose to evaluate experimentally an AmBC system using a mMIMO base station as reader. As illustrated in Figure 4-10, we consider an uplink transmission scenario in an anechoic chamber. First, a device, considered as source in the AmBC system, sends pilots to the reader. The ambient backscatter tag, in the environment, impacts the propagation channel between the device and the reader. The considered tag has two states: a backscattering state in which the dipole antenna is short-circuited (null impedance) and a transparent state in which the antenna is open-circuited (infinite impedance). The propagation channel between the device and the reader depends on the tag state. The reader receives the signal and estimates the propagation channel for the backscattering and the transparent state of the tag. As each state codes a bit of the tag message, the reader is able to decode the tag message.

Massive MIMO antennas in 5G networks exploit the spatial diversity of the propagation channel to increase the robustness or the throughput of the wireless communication link. It has been shown in 2.1.7 that 5G MIMO antenna can provide large benefits for low power IoT devices. Indeed, the space-time digital processing capability of the mMIMO 5G base station can be used to detect low power connected objects.

In [127] and [128], an AmBC Wi-Fi system is proposed where source, tag and reader are equipped with MIMO antennas. Such system exploits channel diversity thanks to multiple radiating elements per antenna. However in experiments, the number of receiving antenna elements was limited to a maximum of 4 elements for the source, tag and reader.

MIMO reader is studied in [88] to overcome the limitations of AmBC systems. A low complexity algorithm is proposed for the multi-antenna reader to optimize the throughput. However, tag used is not entirely passive and this system has not been experimented and tested in real environment.

We propose to exploit the channel spatial diversity using an antenna with 64 elements as reader. The considered mMIMO antenna is optimized for a carrier frequency between 3.6-3.8

GHz. This antenna has been designed for space-time channel sounding and presented in [129]. The antenna is a Slant Uniform Planar Array (SUPA), composed of 32 elements in vertical polarization and 32 in horizontal polarization with a uniform spacing of half-wavelength.

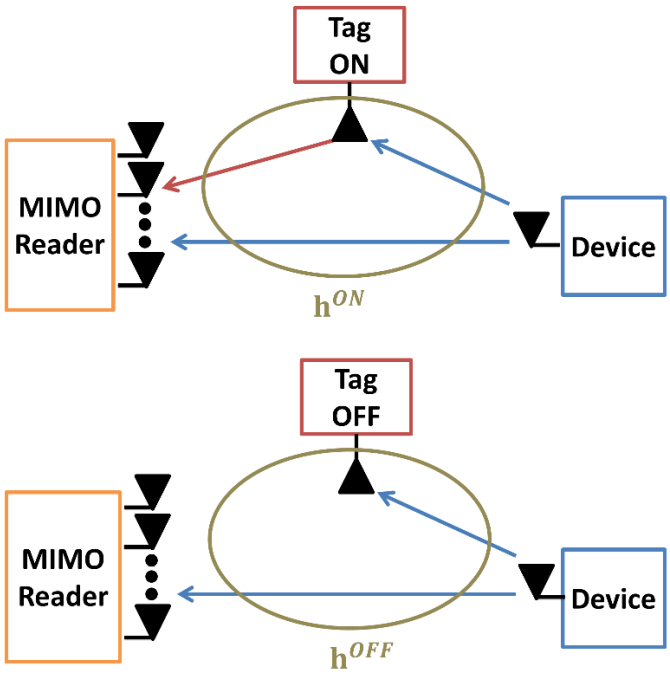

Figure 4-10 Backscattering system using MIMO reader in uplink configuration.

Based on the experimental channel estimation campaign, we propose to evaluate the performance of the system using a LSE estimator to detect the state of the tag. The performance is evaluated by adding additive white gaussian noise (AWGN) to the received signal based on the real channel estimation. Hence, the performance can be evaluated as function of the SNR.

The study is organized as follows: sub-section 4.2.2 presents our system model, sub-section 4.2.3 presents experimental setup, sub-section 4.2.4 presents our results and the section 4.2.5 concludes this study.

4.2.2. System Model

4.2.2.1. *Channel estimation*

As illustrated in Figure 4-10, we consider an AmBC system, in an uplink configuration, with a mobile device as a source and a mMIMO antenna as a reader. The reader is equipped with a SUPA of K elements with uniform spacing of half-wavelength.

We consider a single-antenna tag with two states: a transparent state (OFF) and a backscattering state (ON), depending on the tag state, the channel between the device and the reader is slightly different as shown in Figure 4-10.

In order to use a realistic model of the mMIMO antenna and the propagation channel, the

channel impulse response (CIR) is measured for each antenna element of the SUPA. The measured CIR is a discrete channel acquired for a maximum excess delay T_{max}, with symbol duration of T_s. The channel coefficients are determined for a bandwidth $B = 1/(T_s)$. The CIR is measured M times in order to average the measurement noise. The m^{th} experimental measurement of the CIR $\mathbf{h}^{(m)}$ is defined as:

$$\mathbf{h}^{(m)}(t) = \sum_{q=0}^{Q-1} h^{(m,q)} \delta(t - qT_s), \tag{4-11}$$

where $h^{(m,q)} \in \mathbb{C}$ is a complex gain, q the time index and Q the number of time index. We have $(Q-1)T_s$, the maximum excess delay.

The estimated channel coefficient vector $\mathbf{h}$ is determined by averaging the M experimental measurement. Therefore $\mathbf{h}$ is defined as:

$$\mathbf{h}(qT_s) = \frac{1}{M} \sum_{m=1}^{M} \mathbf{h}^{(m)}(qT_s), \tag{4-12}$$

The reader stores $\mathbf{h}$ for the two states of the tag. We denote $\mathbf{h}^{(OFF)}$ and $\mathbf{h}^{(ON)}$, as the stored $\mathbf{h}$ for the transparent and backscattering states, respectively.

The signal received for the q^{th} time index, over the K antenna ports of the reader is $\mathbf{y}(qT_s) \in \mathbb{C}^{K\times 1}$, it is defined for the antenna $k \in [1 \dots K]$ as:

$$\mathbf{y_k}(qT_s) = \mathbf{h_k}(qT_s)\sqrt{P_u} + \mathbf{v_k}(qT_s), \tag{4-13}$$

where and $\mathbf{h_k}(qT_s)$ the normalized channel coefficient between the device D and the antenna element k for the bandwidth B, $\mathbf{v_k}(qT_s)$ is the noise for the element k of the reader, and P_u is the transmit power spectral density. We denote $P_{noise} = \frac{E[\|\mathbf{v}\|^2]}{K}$, as the received noise power spectral density, where $\|.\|^2$ is the Frobenius norm. We define a signal to noise ratio metric SNR:

$$SNR = \frac{P_u}{P_{noise}}. \tag{4-14}$$

4.2.2.2. *LSE Estimator*

The reader compares $\mathbf{y}$ and the stored estimation $\mathbf{h}$ and calculated $\hat{y}$ the mean square error:

$$\hat{y} = \arg\min \left\{ \sum_{q=0}^{Q-1} \|\mathbf{z}(qT_s) - \mathbf{y}(qT_s)\|^2 \right\} \tag{4-15}$$

$$with\ \mathbf{z}(qT_s) \in \left\{\mathbf{h}^{(ON)}(qT_s), \mathbf{h}^{(OFF)}(qT_s)\right\}.$$

Based on the equation (4-15) we obtain two values of $\hat{y}$, for $\mathbf{z} = \mathbf{h}^{(ON)}$ and for $\mathbf{z} = \mathbf{h}^{(OFF)}$, the estimator keeps the minimum value between the two. It associates an estimated bit equals to 1 if

the backscattering state is detected (ON) and 0 if the transparent state is detected (OFF).

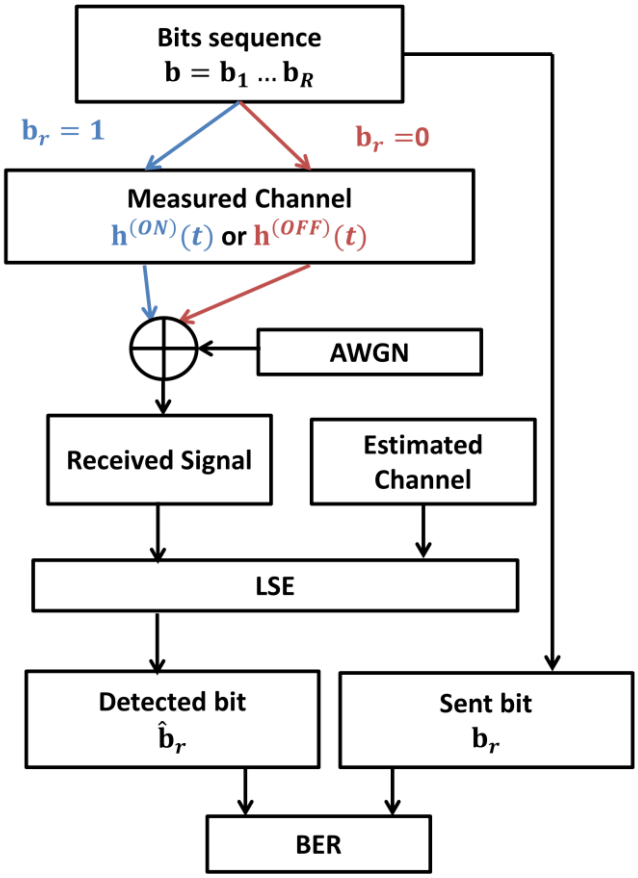

Figure 4-11 Overview of system detector.

To evaluate the general performance of the system, we consider a random sequence of R sent bits $\mathbf{b} = \mathbf{b}_1 \dots \mathbf{b}_r \dots \mathbf{b}_R$, if $\mathbf{b}_r = 1$ (or $\mathbf{0}$ respectively) we use $\mathbf{h} = \mathbf{h}^{(ON)}$ (or $\mathbf{h}^{(OFF)}$ respectively) in equation (4-13). Then, we deduce a sequence of R bits from the LSE detector $\hat{\mathbf{b}} = \hat{\mathbf{b}}_1 \dots \hat{\mathbf{b}}_r \dots \hat{\mathbf{b}}_R$, we compare the detected bits $\hat{\mathbf{b}}$ with the sent bits $\mathbf{b}$ and we calculate the BER as follows:

$$BER = \frac{\sum_{r=1}^{R} \left| \hat{\mathbf{b}}_r - \mathbf{b}_r \right|^2}{R}. \tag{4-16}$$

4.2.3. Experimental Setup

CIR measurements were conducted in an anechoic chamber. The experimental system consisted of a 64 elements mMIMO antenna, a device to illuminate a two states tag. These elements are illustrated in the complete system in Figure 4-12 and in Figure 4-13 as separated elements.

For a sample acquisition, the device, illustrated in Figure 4-13-c), transmits a pulse signal at the carrier frequency of 3.7 GHz. The mMIMO antenna, illustrated in Figure 4-13-a), receives

the device signal through the propagation channel acquires the signal on each of the 64 elements. The system response is measured for a maximum excess delay of 4.10^{-8} seconds for different antenna and bandwidth configurations.

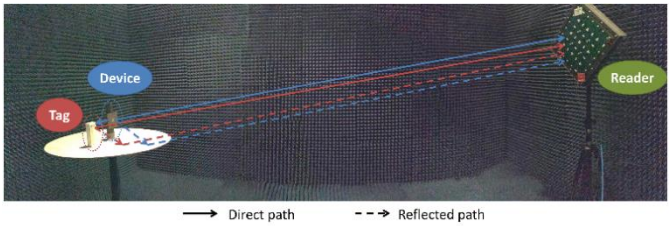

Figure 4-12 Photo of the complete experimental system.

The two states tag is illustrated in Figure 4-13-b), we observe the half wavelength dipole antennas and a switch that allows us to change the state of the tag. The switch can open-circuit the antenna branch (transparent) and short-circuit the branch of the antenna (backscattering).

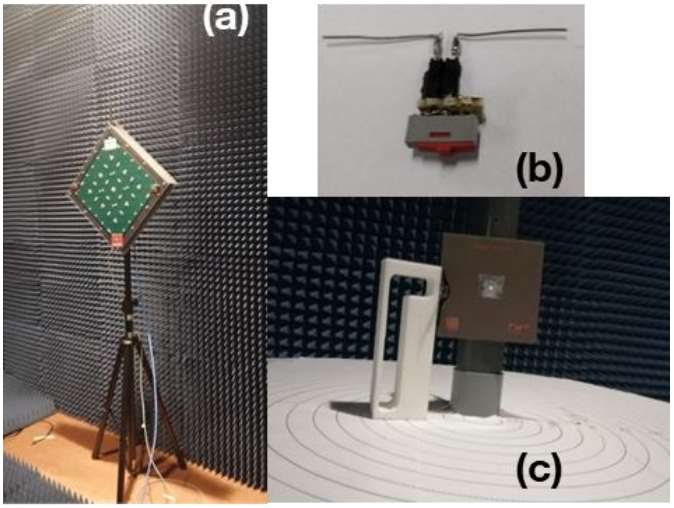

Figure 4-13 Photos of the 64 elements antenna (a), of the tag (b), of device and tag (c).

The channel has been measured for a distance separating the tag and the device equal to 2λ, and for a fixed position of the device, the tag and the MIMO antenna. The measurement has been done for the two states of the tag (transparent and backscattering). Each channel acquisition was repeated between M=5 to M=6 times.

Table 4-2 Experimental Parameters.

Parameters	***Details***	***Value***	***Units***
K	Number of Reader Antenna	{1, 2, 4, 8, 16, 32, 64}	
R	Number of bits per sequence	10^6	
d^{D-T}	Distance between the Device and the tag	2λ	m
M^{ON}	Number of acquisition (ON state)	6	
M^{OFF}	Number of acquisition (OFF state)	5	

The gains and the phases for each elements of the MIMO antenna are obtained with the measurement campaign. Based on these acquisitions, the 64 channels are evaluated for the two states of the tag.

In this simulation we evaluate the performance of the tag state detection using a LSE algorithm for a SNR between -10 dB and 20 dB.

4.2.3.1. *Massive MIMO Antenna*

We evaluate the performance as function of the number of receiving antenna elements. The different configurations are illustrated in Figure 4-14. The number K of antenna elements depends on the number of active elements on the reader antenna. The configurations are chosen in such a way that the total spatial occupancy of the active elements increases with K. This enables us to emulate a large variety of readers: from small devices, laptops, tablets, small cells, MIMO base stations, up to mMIMO base stations.

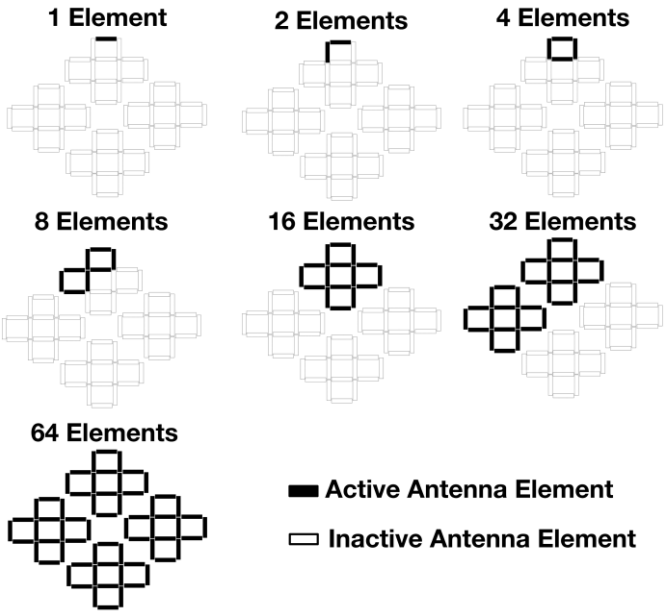

Figure 4-14 Configurations of the MIMO antenna.

4.2.3.2. *Bandwidth*

The performance of the system is also evaluated as a function of the bandwidth. We consider 3 different configurations for the bandwidth of the measured signal, detailed in Table 4-3. For each configuration, we keep the same central frequency, as illustrated in Figure 4-15.

Table 4-3 Bandwidth Configurations.

Bandwidth Configuration	***B1***	***B2***	***B3***
Bandwidth (MHz) : B	100	60	20
Number of time samples per acquisition : Q	5	3	1
Symbol duration (seconds) : T_s	1.10^{-8}	2.10^{-8}	5.10^{-8}
Maximum excess delay (seconds) : T_{max}	40.10^{-8}	40.10^{-8}	40.10^{-8}

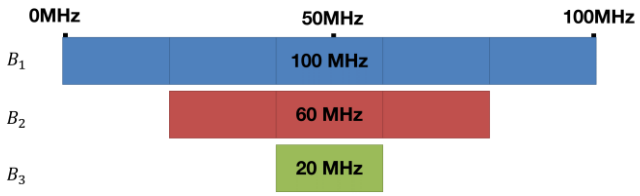

Figure 4-15 Configurations of the bandwidth.

In order to allow fair comparison between the three configurations, the power spectral densities of the signal and the noise are kept identical when changing the bandwidth. As a consequence, when we consider a large bandwidth, the number of symbols increases but the SNR (per symbol) is the same.

4.2.4. Results

This section presents experimental results based on the model depicted in 4.2.2, and the setup given in Section 4.2.3.

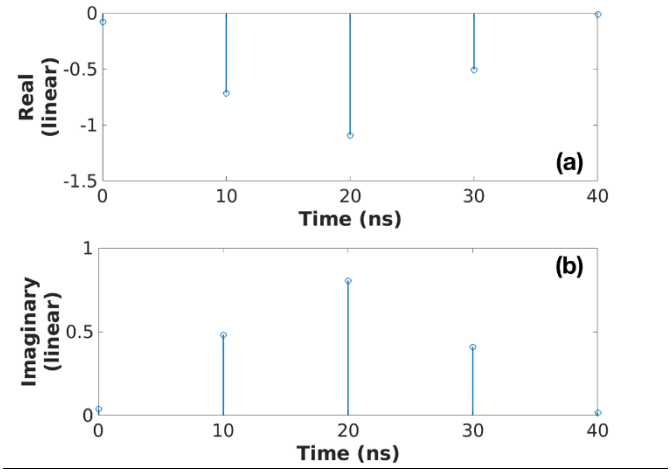

Figure 4-16 Example of CIR as function of the time for the first antenna element: a) real part b) imaginary part.

We first observe in Figure 4-16 the amplitude of the experimental CIR of the system for the first element of the reader antenna as function of the time. The channel has several echoes corresponding to the tag and the support table. The support creates a non-negligible reflection even if the material of the support is not very sensitive to electromagnetic waves.

In Figure 4-17, the 64 elements of the mMIMO antenna are positioned on a grid of 8 lines and 8 columns. The maps illustrate the spatial signature in line as function of the time for the two states. The top maps (a) illustrate the amplitude of the CIR coefficients for qT_s = 0 to 40 ns. The bottom maps (b) illustrate the phase between -180° and 180° of the CIR. We observe the spatial diversity of the mMIMO antenna. One can note that between the two states of the tag the differences are visible in the phase domain. The amplitude of the signal received for each element

of the reader is not significantly impacted by the state of the tag. However, the impact is more significant for the phase domain.

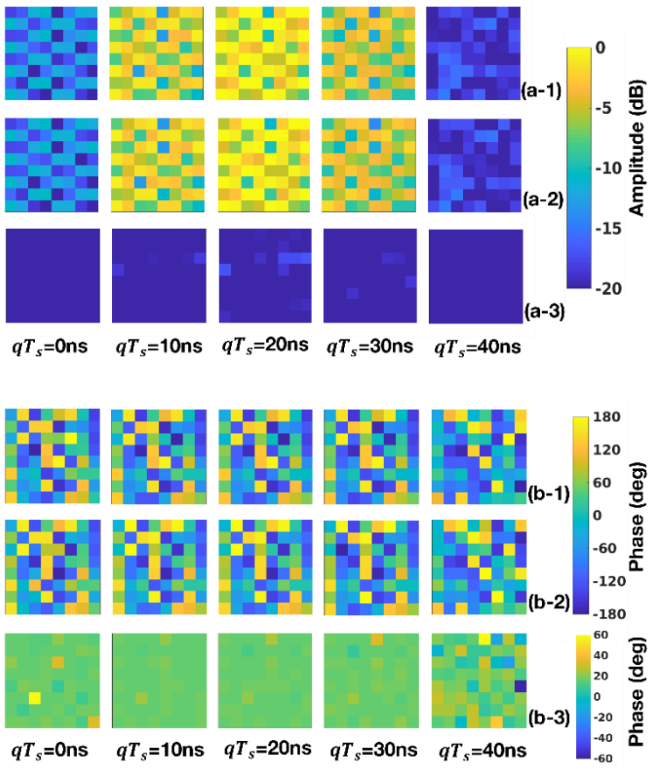

Figure 4-17 Example of CIRs for the 64 receive antenna elements configurations. a-1) amplitude of the CIR for the transparent state, a-2) amplitude of the CIR for the backscattering state, a-3) amplitude difference between the two states b-1) phase of the CIR for the transparent state, b-2) phase of the CIR for the backscattering state, b-3) difference of phase between the two states (on average equal to 16 degrees).

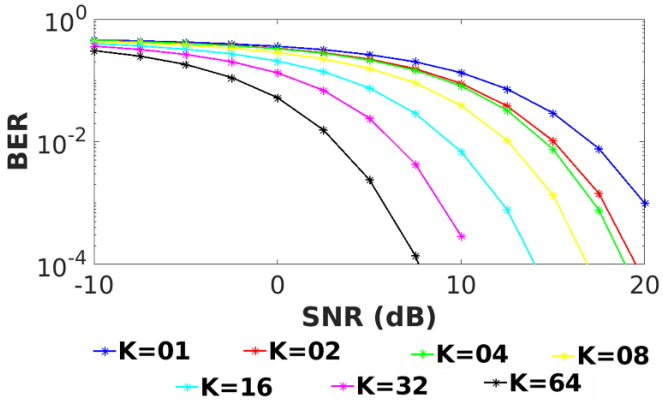

Figure 4-18 Bit error rate as function of SNR for different K antenna elements configurations.

Figure 4-18 illustrates the BER as function of the SNR for different configurations of *K* antenna elements. Each antenna configuration is evaluated for the bandwidth configuration B1 (100 MHz). We observe that as the number of antennas increases the performance is improved. The MIMO antenna exploits the channel diversity and this improves the reliability and the

robustness of the detection.

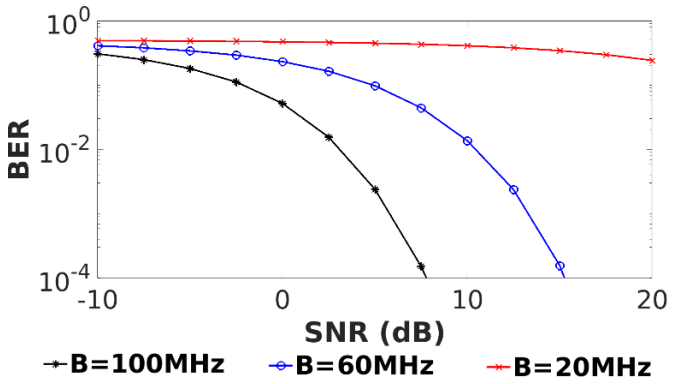

Figure 4-19 Bit error rate as function of SNR for different bandwidth configurations.

Figure 4-19 illustrates the BER as function of the SNR for different bandwidth configurations. Each bandwidth configuration is evaluated for $K = 64$ antenna elements. We observe that the performance is improved if the bandwidth increases. This is due to the fact that the frequency diversity of the channel increases with the bandwidth. Indeed, the impact of the echoes, which create frequency diversity, increases with the bandwidth. Diversity improves the performance of the LSE detector. The performance of the bandwidth $B = 20$ MHz is poor because the bandwidth is too reduced to have the impact of the echoes.

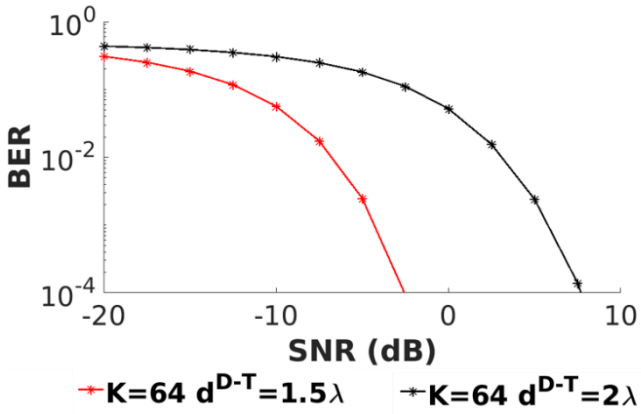

Figure 4-20 Bit error rate as function of SNR for different device to tag distance configurations.

Finally, we evaluate the performance depending on the distance between the device and the tag. Device location is fixed and the tag is located at 1.5 or 2 lambda of the device. In the Figure 4-20 we observe that the performance is impacted by the distance. This effect has been observed in SISO with ellipses in [47] and was due to the phase of the signal. As we observe in Figure 4-21 the phase difference is more significant for the configuration $d^{D-T} = 1.5\lambda$ and may result in the performance improvement. For further studies, remains the performance evaluation with respect to the distance between the tag and the device in a MIMO reader configuration.

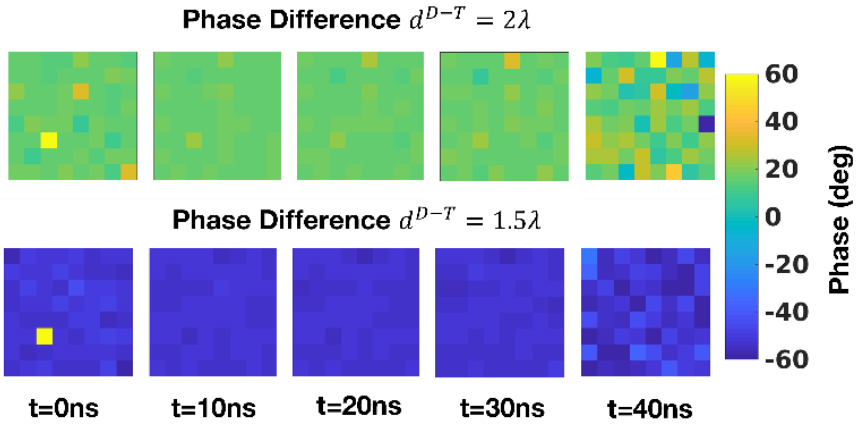

Figure 4-21 Phase difference of the CIR between the two states (transparent and backscattering) for different distance device to tag configurations. 64 elements of the mMIMO antenna are positioned on a grid of 8 lines and 8 columns.

4.2.5. Conclusion

In this section, we have evaluated the performance of an ambient backscatter system with a mMIMO antenna as a reader and a mobile device as a source, experimentally. A device sends a signal to the reader that is backscattered or not, by a tag, depending on the tag state. The reader estimates the channel for the two states of the tag (transparent and backscattering) and applies a least square error algorithm to detect the bit sent by the tag corresponding to the state of the tag. This experimental evaluation has been done for multiple values of signal to noise ratio. We show that the spatial diversity of the reader antenna highly improves the performance of the detection. We have also shown the impact of the number of receiving antenna and the bandwidth. Future studies should assess the performance on more complex propagation channels, outside anechoic chamber and using multi-state tags.

Chapter 5

Reconfigurable Intelligent Surface-assisted AmBC

The main objective of this chapter is to investigate the impact of RIS deployment on AmBC systems performance. We propose to use the RIS in order to improve the quality of the signal at the reader and the tag locations. We first present the characteristic of our RIS prototype with continuous phase-shifting. Then, we assess experimentally with the presented prototype a method to improve the performance of the RIS-assisted AmBC system.

5.1. INTRODUCTION

In the literature, RISs have been proposed to increase the quality of the signal at the reader location in an AmBC system [98]. More precisely, it has been shown by means of simulations in rich-scattering environments that an RIS can modify the multipath channel and enhances the system performance. Similarly, in [130] it has been proposed to use an RIS to assist a cognitive backscattering communication system. However, these solutions proposed in [98] and [130] have not been tested and verified experimentally. Indeed, the idea of using RISs in AmBC systems has only been experimentally studied from the information-theoric standpoint in [131], where an RIS communicates a message to a reader.

In this chapter, we propose a new practical RIS-assisted AmBC system, to be deployed above an information desk on which tags are exposed for the purpose of reading. In our system the RIS does not transmit any data but helps existing tags to transmit to the reader. In our proposed system, the ambient source is the room Wi-Fi access point which position is fixed and in LOS of the desk, and its location is known, i.e., registered at the RIS. On the contrary, the exact locations of the tag and reader on the desk are unknown. The desk area is split into pre-defined locations. The RIS is close to the desk and has two features. First, the RIS can pick a beam among a pre-defined codebook. Each beam is designed to reflect waves coming from the exact source location towards one of the pre-defined locations on the desk. Second, the RIS can apply a common phase

shift to all its elements. The RIS tests several pairs of beam and common phase-shift. Each time, the reader reports a performance quality feedback (a quantized contrast for instance). The RIS and the reader together search for the beam and common phase-shift pair that maximizes the performance. We expect, with such approach, to improve the BER, with respect to the scenario without RIS, with a similar approach as in 4.1: i.e., either by creating a "hot spot" on the tag (and boosting the backscattered wave), or by creating "coherent spots" both on the tag and the reader, in such a way that all waves reflected by the RIS combine coherently with all other waves, when arriving at the reader (to boost the received contrast). Finally, through experiments, we validate our approach and show a significant performance improvement.

The rest of the chapter is organized as follows: Section 5.2 introduces the model of our proposed new system, Section 5.3 introduces the RIS prototype with continuous phase-shifting capability and discusses its characteristics, Section 5.4 describes our experimental setup for validation, Section 5.5 illustrates the obtained experimental results and Section 5.6 concludes this paper.

5.2. System Model

5.2.1. Channel modeling

We consider the communication between one tag and one reader assisted by an RIS in a LOS environment. Our system model, illustrated in Figure 5-1, does not take into account the mutual coupling between the RIS elements (cells) [132]. First, the source transmits a signal originally destined to a legacy device. The signal is then reflected by the RIS with M cells and also backscattered by the tag to the reader.

The reader (R) receives the signal from the source (S) through the channel g composed of four different paths between S and R. Among them, two paths are controlled by the RIS and two are modulated by the tag (T). The direct path is denoted by "S-R". The multi-hop path that is modulated by the tag is denoted by "S-T-R". The multi-hop path that is reflected by the RIS is denoted by "S-R, RIS". Finally, the path that is reflected by the RIS and is modulated by the tag is denoted by "S-T-R, RIS". Other paths, with more hops, are neglected. Multi-hop paths are composed of single-hop paths: "S-T", "T-R". Table 5-1, defines, for each path, the path-specific notation of the channel coefficient h, the amplitude a and the distance d. With such notation and definitions, g is given by:

$$g = h^{S-R} + \gamma h^{S-T-R} + h^{S-R,Ris} + \gamma h^{S-T-R,Ris}, \quad (5\text{-}1)$$

where γ is a scalar that can take two different values depending on the state of the tag ($\gamma = 1$ if the tag is in the backscattering state and $\gamma = 0$ if the tag is in the transparent state).

Table 5-1 Notations of the propagation channel coefficients for all paths.

Path	***Channel coefficient*** ($\boldsymbol{h} \in \mathbb{C}$)	***Phase of the propagation channel coefficient*** ($\boldsymbol{\phi} \in \mathbb{R}$)	***Amplitude*** ($\boldsymbol{a} \in \mathbb{R}^+$)	***Distance*** ($\boldsymbol{d} \in \mathbb{R}^+$)
S-R	h^{S-R}	ϕ^{S-R}	a^{S-R}	d^{S-R}
S-T	h^{S-T}	ϕ^{S-T}	a^{S-T}	d^{S-T}
T-R	h^{T-R}	ϕ^{T-R}	a^{T-R}	d^{T-R}
S-T-R	h^{S-T-R}	ϕ^{S-T-R}	a^{S-T-R}	d^{S-T-R}
S-R,RIS	$h^{S-R,Ris}$	$\phi^{S-R,Ris}$	NA	NA
S-T-R,RIS	$h^{S-T-R,Ris}$	$\phi^{S-T-R,Ris}$	NA	NA

Whatever the path without RIS reflection is, the coefficient h of a propagation channel can be approximated by:

$$h = ae^{j\phi}, \tag{5-2}$$

with $\phi = \frac{2\pi d}{\lambda}$, where λ corresponds to the wavelength of the signal. The channel coefficient of a path between a point A and a point B, assisted by the reflection of the RIS, depends on the channel coefficients of the sub-paths between A and each cell of the RIS, and the sub-paths between each cell of the RIS and B.

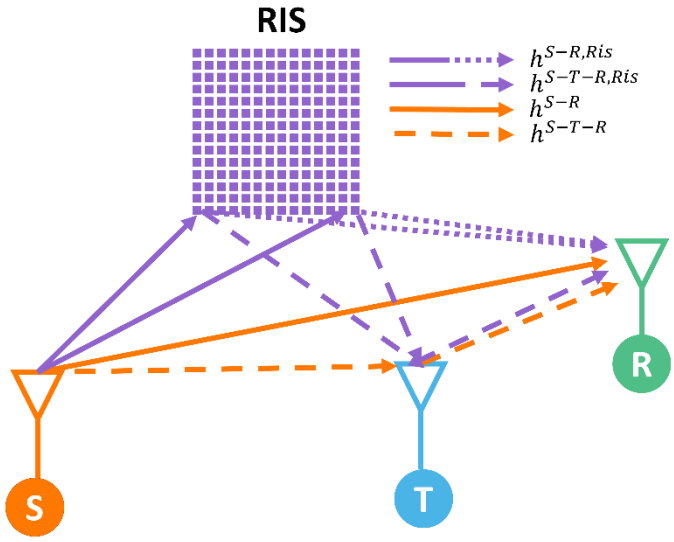

Figure 5-1 System model with the links between the source (S), the RIS, the tag (T) and the reader (R).

Hence we define the channel vectors $\mathbf{h}^{Ris-R} \in \mathbb{C}^{M\times 1}$, $\mathbf{h}^{S-Ris} \in \mathbb{C}^{1\times M}$ and $\mathbf{h}^{Ris-T} \in \mathbb{C}^{M\times 1}$ with sub-paths defined in Table 5-2. For each sub-path, the sub-path-specific notation for the channel coefficient h, its amplitude a and its phase ϕ, is provided. Again, whatever the sub-path is, we

have: $h = ae^{j\phi}$.

Table 5-2 Notations for the RIS channel sub-paths.

Sub-Path	***Channel coefficient*** ($\mathbf{h}_m \in \mathbb{C}$)	***Phase of the propagation channel coefficient*** ($\boldsymbol{\phi} \in \mathbb{R}$)	***Amplitude*** ($\boldsymbol{a} \in \mathbb{R}^+$)	***Distance*** ($\boldsymbol{d} \in \mathbb{R}^+$)
S-cell m of the RIS	$\mathbf{h}_m^{S-Ris}$	ϕ_m^{S-Ris}	a_m^{S-Ris}	d_m^{S-Ris}
cell m of the RIS-R	$\mathbf{h}_m^{Ris-R}$	ϕ_m^{Ris-R}	a_m^{Ris-R}	d_m^{Ris-R}
cell m of the RIS-T	$\mathbf{h}_m^{Ris-T}$	ϕ_m^{Ris-T}	a_m^{Ris-T}	d_m^{Ris-T}

With the notations defined in Table 5-1 and Table 5-2, we obtain:

$$h^{S-T-R} = h^{S-T} h^{T-R}, \tag{5-3}$$

$$h^{S-R,Ris} = \mathbf{h}^{S-Ris}\mathbf{u}\mathbf{h}^{Ris-R}, \tag{5-4}$$

$$h^{S-T-R,Ris} = \mathbf{h}^{S-Ris}\mathbf{u}\mathbf{h}^{Ris-T} h^{T-R}, \tag{5-5}$$

where $\mathbf{u}$ is the matrix of the reflection beamforming phase-shift coefficients applied to the cells of the RIS. In this chapter, we consider an RIS that can only phase shifts the signal (without amplitude modulation). Therefore, $\mathbf{u}$ is a diagonal matrix, of size M, of unitary complex coefficients.

5.2.2. Energy detector: performance metrics

On the reader side, we consider an energy detector to detect the tag. The performance of such detector depends on the amplitude of the signal contrast received by the reader Δg between the two states of the tag, i.e. $\Delta g = \left| |g_{\gamma=1}| - |g_{\gamma=0}| \right|$. The signal level received by the reader for each state of the tag ($\gamma = 1$ or $\gamma = 0$) can be determined with the equation (5-1) and the amplitude of the contrast can be expressed, with the RIS Δg^{Ris} and without the RIS Δg^{ref}, as follows:

$$\Delta g^{ref} = \left| |h^{S-R} + h^{S-T-R}| - |h^{S-R}| \right|, \tag{5-6}$$

$$\Delta g^{Ris} = \left| \left| h^{S-R} + h^{S-T-R} + h^{S-R,Ris} + h^{S-T-R,Ris} \right| - \left| h^{S-R} + h^{S-R,Ris} \right| \right|. \tag{5-7}$$

In these expressions, only the terms $h^{S-R,Ris}$ and $h^{S-T-R,Ris}$ are controllable by the RIS.

Considering an energy detector used by the reader to decode the tag message, the performance is given, as in [47] by:

$$BER = 0.5 \operatorname{erfc}\left(\frac{\Delta g}{\xi}\right), \tag{5-8}$$

where ξ is the square root of the noise average power.

5.2.3. Codebook-based reflection beamforming

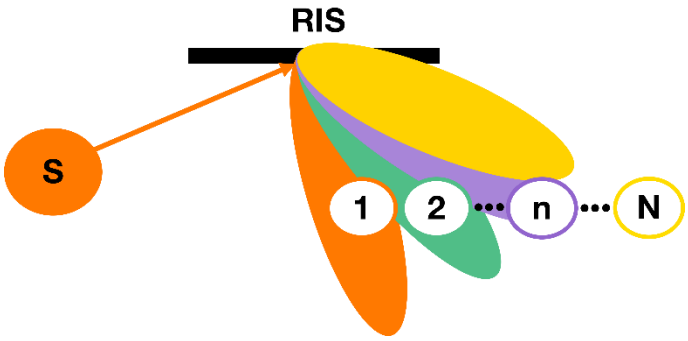

Figure 5-2 Codebook principle.

We propose to improve Δg with the RIS by using a codebook-based reflection beamforming state approach. We first split the considered area (information desk) on which the tag and the reader are placed into N predefined locations. For each location n, we compute the matrix of predefined reflection beamforming coefficients $\mathbf{b}^{(n)}$ that must be applied to the RIS, to create a reflected beam targeting the considered location n, as illustrated in Figure 5-2. $\mathbf{b}^{(n)}$ is a vector of unitary complex coefficients of size M. The codebook $\boldsymbol{B}$ is defined as the set of reflection beamforming vector $\boldsymbol{B} = \{\mathbf{b}^{(1)} \dots \mathbf{b}^{(n)}, \dots, \mathbf{b}^{(N)}\}$, each vector corresponds to a reflection beamformer that targets a predefined location. We build the diagonal phase-shift matrix $\mathbf{u}$ as follows:

$$\mathbf{u}_{m,m}(n,\delta) = \mathbf{b}_m{}^{(n)} e^{j\delta}, \tag{5-9}$$

With this notation, $\mathbf{b}_m{}^{(n)}$ is a cell-specific beam coefficient to be applied to the cell m of the RIS to target the location n, whereas $\delta \in \Delta$ is a beam phase-shift applied to all cells, that is chosen among a set of P pre-defined beam phase-shifts, $\Delta = \left\{0, \dots, \frac{2\pi}{P}, \dots, \frac{2\pi(P-1)}{P}\right\}$.

In order to compensate the phase shifts induced by the propagation channel (see equation (5-2)) and therefore ensure a coherent focusing towards the target exact location n (as illustrated in Figure 5-3), the predefined reflected beamforming coefficient $\mathbf{b}_m{}^{(n)}$ of the m$^{\text{th}}$ cell of the RIS is computed from:

$$\mathbf{b}_m{}^{(n)} = \alpha_m e^{-j2\pi \frac{d_m^{S-Ris} + d_m^{Ris-n}}{\lambda}}, \tag{5-10}$$

where α_m is the amplitude the unit cell reflection coefficient. Note that to compute the predefined coefficient $\mathbf{b}_m{}^{(n)}$ the location of the source and the RIS, and the propagation channels, must be known. The chosen spherical wave assumption for the phase dependence is suitable for the considered scenario, where the source and the target are close to the RIS. Indeed, as illustrated in Figure 5-3, in this case, the difference of beam coefficients between two successive cells is not

constant as it takes into account the exact distances between all elements. Note that this simple computation method of reflecting beamforming coefficients does not take into account the mutual coupling between the cells of the RIS. We thus expect this method to be accurate enough to control for the direction of the main lobe of the reflected beam and less accurate for the control of the side lobes of the reflected beams.

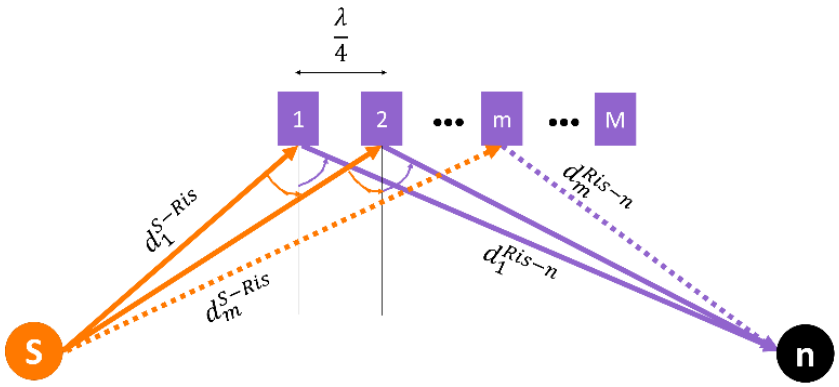

Figure 5-3 Illustration of the model for the cells coherently targeting the location n, knowing the exact location of the source S.

Together, the RIS and the reader find, through an exhaustive search, the $\mathbf{b} \in \boldsymbol{B}$ and δ pairs that maximise the performance, e.g. Δg. We expect at least two types of such pairs to exist such as $\Delta g^{Ris} > \Delta g^{ref}$.

In the first type of pairs, a "hot spot" beamformer $\mathbf{b}^{hs} \in \boldsymbol{B}$ improves Δg^{Ris} by boosting $h^{S-T-R,Ris}$ and reducing $h^{S-R,Ris} \approx 0$: thus, it creates a hot spot on the tag. In this case, equation (5-7) becomes:

$$\Delta g^{Ris} \sim \left| \left| h^{S-R} + h^{S-T-R} + h^{S-T-R,Ris} \right| - \left| h^{S-R} \right| \right|. \tag{5-11}$$

In this case, δ must be chosen such that:

$$\arg(h^{S-R} + h^{S-T-R}) = \arg\left(h^{S-T-R,Ris}\right) [2\pi], \tag{5-12}$$

which is equivalent to:

$$\delta = \arg(h^{S-R} + h^{S-T-R}) - \arg\left(\mathbf{h}^{S-Ris}\mathbf{b}^{hs}\mathbf{h}^{Ris-T}h^{T-R}\right) [2\pi]. \tag{5-13}$$

In the second type of pair, a "coherent spot" beamformer would attain the coherence condition. More precisely, the coherence condition illustrated in Figure 5-4 is obtained when the sum of the signals controlled by the RIS arrive at the reader location in phase with the sum of all the other signals. Such condition ensures that the two sums combine coherently and boost Δg^{Ris}. This coherence condition is expressed as follows:

$$\arg(h^{S-R} + h^{S-T-R}) = \arg\left(h^{S-T-R,Ris} + h^{S-R,Ris}\right) [2\pi]. \tag{5-14}$$

We expect to find in the codebook a beam $\mathbf{b}^{cc} \in \boldsymbol{B}$ that boosts $h^{S-T-R,Ris} + h^{S-R,Ris}$, for instance, by targeting at the same time the tag and the reader locations. For example, in some

cases, this term can be boosted by two lobes of the same beam, pointing at the tag and the reader. Then, the following δ satisfies condition:

$$\delta = \arg(h^{S-R} + h^{S-T-R}) - \arg(\mathbf{h}^{S-Ris}\mathbf{b}^{cc}\mathbf{h}^{Ris-R} + \mathbf{h}^{S-Ris}\mathbf{b}^{cc}\mathbf{h}^{Ris-T}h^{T-R}). \quad (5\text{-}15)$$

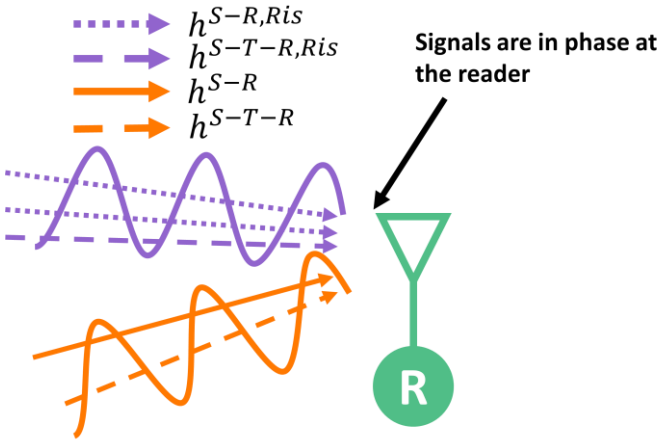

Figure 5-4 Illustration of the coherent spots with the signals controlled by the RIS in phase with the direct signals (not passing through the RIS) at the reader.

5.3. RIS Prototype with Continuous Phase-Shifting

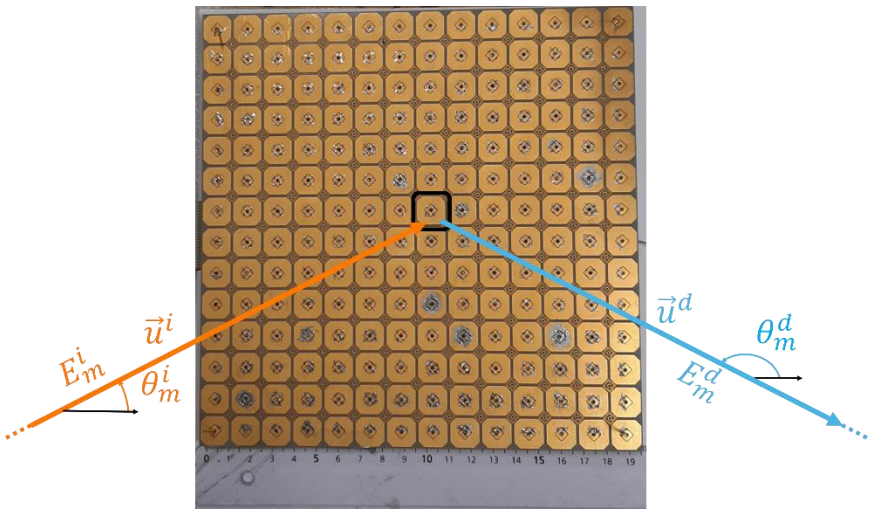

Figure 5-5 RIS prototype with continuous phase-shifting. The incident (orange) and reflected (blue) fields are illustrated for one single cell. The passive beamforming is obtained thanks to the independent control of all cells.

For the experiment we consider, as illustrated in Figure 5-5, a RIS prototype composed of 14×14 unit cells. Each unit cell is a reflecting conductive patch that can be reconfigured independently of the others. In particular, the unit cell is a three-dimensional patch on a dielectric substrate. The patch is made of two conductive areas separated by an annular slot. The inner and outer areas are connected to each other with four MA46H120 varactor diodes. The specific

arrangement of the varactor diodes ensures the adjustment of the capacitance of the unit cell, which provides the desired tunability of the reflection coefficient of the unit cell. In detail, in the reverse bias, the capacitance of a varactor diode is inversely proportional to the junction voltage. Thus, the capacitance of the unit cell can be tuned by controlling the DC voltage applied to the four varactors. As illustrated in Figure 5-6, the unit cell can be reconfigured by applying different voltages to the four varactor diodes, which, in turn, enables the configuration of the reflection coefficient.

In the realized unit cell structure, four varactors are used for each unit cell for ensuring a good symmetry of the radiation pattern. All unit cells have identical design and size, i.e., 14×14 mm. They are engineered to operate in the frequency range 5.15-5.75 GHz [133][134], which yields a cell size of approximately a quarter of the signal wavelength. The unit cell structure has been characterized through full-wave simulations in Ansys HFSS under periodic boundary conditions. In detail, the results are obtained by considering an infinitely large surface that is a periodic repetition of a unit cell configured to realize a given reflection coefficient.

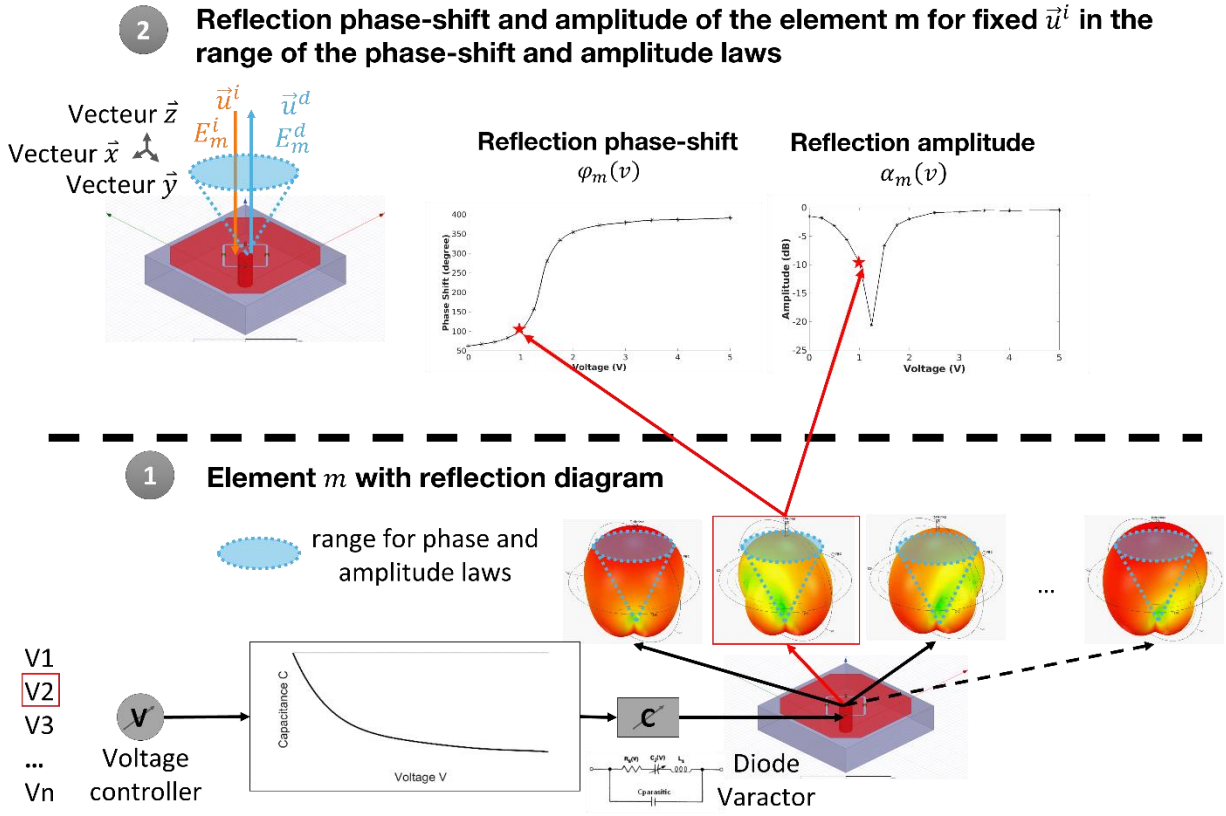

Figure 5-6 Unit cell with a voltage-controlled tunable reflection coefficient $r(\vec{u}^i, v)$. Full-wave simulation results under periodic boundary conditions [133][134].

As illustrated in Figure 5-6 , the reflection coefficient of each unit cell can be obtained through the voltage-controlled capacitance. A periodic surface reflects an incident plane wave of direction $\vec{u}^i$ in several discrete directions given by the reciprocal lattice. Here because the cell dimension is smaller than half a wavelength, the wave is reflected only in the specular direction, i.e., $\vec{u}^d =$

$\vec{u}^i - 2\vec{n}(\vec{u}^i.\vec{n})$ where $\vec{n}$ is the normal direction of the RIS cell. Due to the linearity of the RIS, the reflected electric field can be written with respect to the incident field E^i as $E^d = E^i \cdot r(\vec{u}^i, v)$, where v is the voltage applied to the unit cell, $\vec{u}^i$ is a unit-norm vectors defined by the azimuth and elevation angles of incidence (θ^i, φ^i) in spherical coordinates, and $r(\cdot)$ is the reflection coefficient. Note that in order to take into account the polarization effect, the reflection coefficient is a 2x2 matrix. However for sake of simplicity, we assume that r is a scalar. The reflection coefficient is probed using the Ansys HFSS EM software under periodic boundary conditions and through measurements conducted with the RIS prototype. As far as the full-wave simulations are concerned, the reflection coefficient of each unit cell is indirectly characterized as a function of the capacitance c of the varactor diodes. As far as the experimental characterization through measurements is concerned the reflection coefficient of each unit cell is directly characterized as a function of the voltage v applied to the varactor diodes. Since the capacity of each varactor diode is voltage-controlled, as illustrated in Figure 5-6, c and v are directly related to each other, i.e., $c = c(v)$. This relation is not necessary in this chapter, but it can be derived through measurements.

The characterization of the reflection characteristics of the unit cell is illustrated in Figure 5-7 for various elevation angles of the incident and reflected electric field. The figure reports, in particular, the phase $\varphi_m(\cdot)$ and the amplitude $\alpha_m(\cdot)$ of the reflection coefficient as a function of the capacitance of the varactor diodes (HFSS simulations) and the junction voltage (prototype experiments). From the results illustrated in Figure 5-7, we evince that both the phase and the amplitude of the reflection coefficient of each unit cell are almost independent of the angle of incidence and reflection, if the incident angle is less than 40 degrees. Within this range of angles, notably, the radiation pattern of the unit cell can be assumed to be almost omnidirectional. For wider angles of deflection, on the other hand, Figure 5-6 shows that the radiation pattern of the unit cell is not omnidirectional, but it depends on the angle of incidence and reflection. As expected, Figure 5-7 shows that the reflection coefficient can be adjusted by appropriately controlling the junction voltage in the range 0-5 V, which corresponds to a capacity in the range 0.2-1 pF.

By considering, therefore, angles of incidence and reflection no larger than 40 degrees with respect to the normal to the unit cell, a simple model for the reflection coefficient of the unit cells can formulated as follows:

$$r(\vec{u}^i, v) \approx r(v) \approx g_0\, \alpha_m(v) e^{j\varphi_m(v)} \tag{5-1}$$

where g_0 denotes the unit cell (constant) gain, and $\alpha(v)$ and $\varphi(v)$ denote the normalized amplitude and the phase of the unit cell reflection coefficient, respectively, which can be configured in a continuous manner as a function of the voltage v that is applied to the varactor diodes. The relation in (5-1) has been experimentally characterized with the RIS prototype. By analyzing the Figure 5-7, we observe that the amplitude and the phase of the reflection coefficient

are dependent of each other, since they both change with the control voltage. In particular, the smallest values of amplitude and the major variation of the phase of the reflection coefficient (see Figure 5-7) are in the same range of DC voltage.

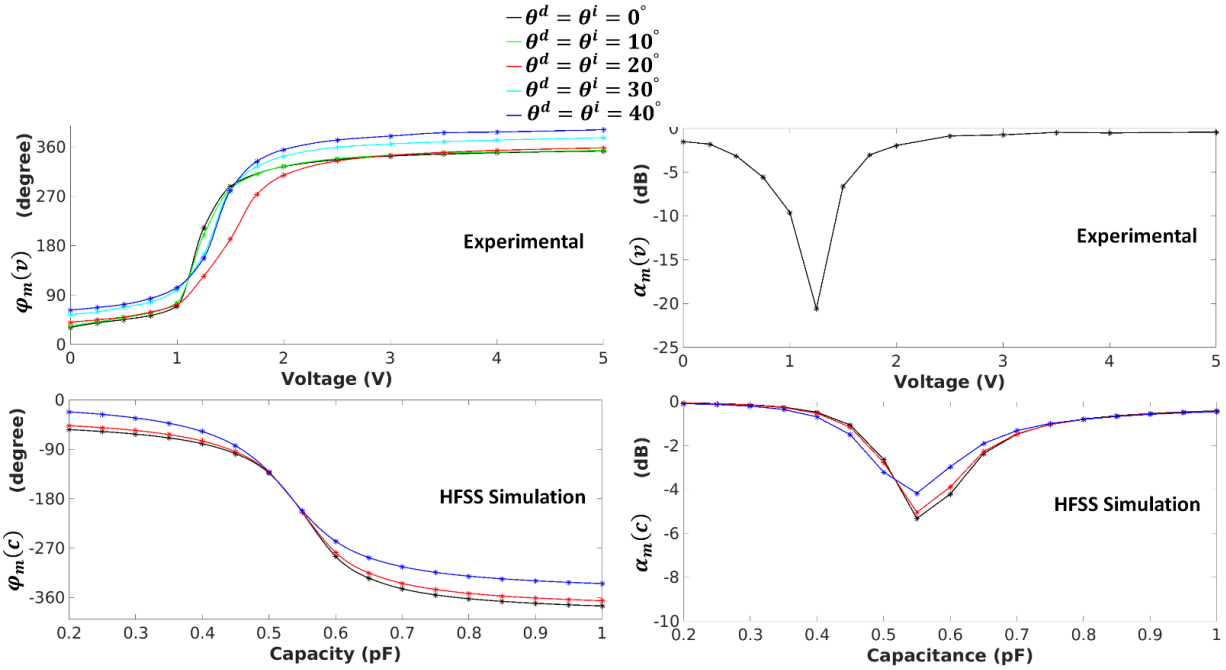

Figure 5-7 Phase and amplitude of $r(\vec{u}^i, v)$ *as a function of* v *and for fixed* $\vec{u}^i$ ($\varphi^i = 0, \varphi^d =$ 180 *degrees). HFSS simulations vs. experimental measurements.*

Therefore to apply the phase-shift condition to create a passive reflected beamforming from the equation (5-10) (5-10), we can choose the voltage that gives:

$$\varphi_m(v)^{(n)} = j2\pi \frac{d_m^{S-Ris} + d_m^{Ris-n}}{\lambda}, \tag{5-16}$$

Thanks to the characterization between the voltage and the phase-shift, we can experimentally apply different voltage values on each cell to obtain the phase-shift corresponding to the predefined beamformer $\mathbf{b}^{(n)}$ that passively reflect the signal toward the (n) location

In this section, we have characterized the phase and amplitude response of the RIS prototype, and have introduced a simple model for the reflection coefficient of each unit cell, based on full-wave simulations, under the modeling assumption of periodic boundary conditions, and experiments. We have demonstrated the main capabilities of the designed RIS prototype: The phase-shift induced by each unit cell can be continuously controlled as a function of the control voltage applied to the unit cell. This feature can be exploited in order to control the angle of reflection of the incidence signal and to beamform the reflected signal towards the desired direction. This is analyzed and experimentally validated next.

5.4. EXPERIMENTAL SETUP

We conduct experimental measurements to validate the proposed principle of RIS-assisted AmBC system presented in Section 5.2. As illustrated in Figure 5-8, the measurements are set up on a desk, with all the devices (source, tag, reader and RIS) in the LOS of each other. The characteristics of the RIS prototype have been detailed in 5.3.

In order to evaluate the benefit of the RIS, two different configurations are tested and compared: with and without RIS. We evaluate the performance of the AmBC system in terms of BER for various **b** and δ pairs.

In the experimental setup, the source, the tag and the reader are all equipped with dipole antennas vertically polarized. The source generates an ambient signal with a 500kHz bandwidth at 5.2GHz. The reader receives the combined signals of the source, the RIS and the tag. A non-coherent energy detector is implemented in the reader to measure, in real time, the contrast Δg defined in Section 5.2. Both the source and the reader are controlled by an universal software radio peripheral (USRP) B210 on two separated channels. The software-defined radio "GNU Radio" is used to acquire the data and process the signals.

The tag switches between two states by disconnecting or connecting the two branches of its dipole thanks to an electronically controlled PIN diode connected between the two branches of the dipole.

The coordinates of the location of each element of the system are denoted by (x^E, y^E, z^E), where the element E can be the source (S), the tag (T), the reader (R) or the RIS. All the elements are located in the same horizontal plane (desk), with $(z^S = z^T = z^R = z^{Ris})$ as vertical coordinates (see as shown in Figure 5-8).

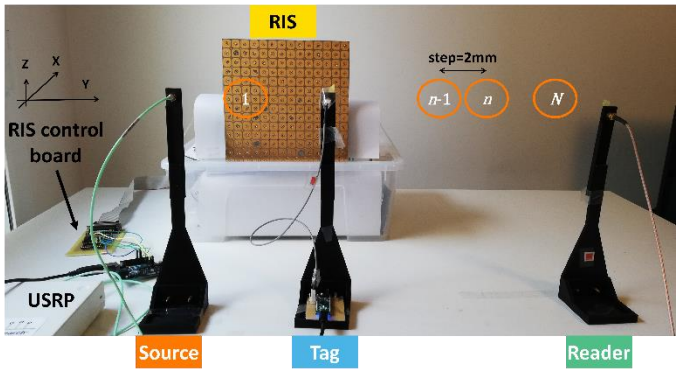

Figure 5-8 Experimental setup.

Hence, we propose to exploit the symmetry of this configuration and limit the control of the RIS beamforming to the horizontal plane only. More precisely, the same beam coefficient is applied to each cell in the same column of the RIS. As a consequence 14 columns are controlled independently.

We first split the desk into N pre-defined locations illustrated in Figure 5-8. For each location n, we compute the corresponding codebook according to Section 5.2 and to the locations of the elements detailed in Table 5-3. Note that as the inter-cell distance is a quarter of the wavelength, the mutual coupling between the RIS elements is not negligible and will impact the radiation pattern. However, the simple codebook computation method of Section 5.2, i.e. without mutual coupling taken into account, is expected to be accurate enough for the control of the main direction and less accurate for the control of side lobes. The N target locations are chosen along the y axis. As the elements are located on that same y axis, we vary the y coordinate of the targets between $y = 0.1$m and $y = 0.4$m with a step of 2mm. This results in $N = 151$ different locations and a codebook of 151 different reflected beams.

Regarding the beam phase-shift δ, we select $P = 18$ phase shift values between 0 and 2π.

Table 5-3 Experimental Parameters.

Parameters	***Details***	***Value***	***Units***
M	Number of independantly controlled RIS cells	14	
N	Number of Beams	151	
P	Number of Beam phase shifts	18	
(x^S, y^S, z^S)	Location of the source	$(0, 0, 0)$	m
$(x^{RIS}, y^{RIS}, z^{RIS})$	Location of the center of the RIS	$(0, 0.1, 0)$	m
(x^T, y^T, z^T)	Location of the tag	$(0, 0.13, 0)$	m
(x^R, y^R, z^R)	Location of the reader	$(0, 0.57, 0)$	m

5.5. RESULTS

This section reports the simulation results obtained by using the simple model described in Section 5.2 and the experimental results obtained from the setup described in Section 5.4.

The following parameters are set to the same values for the simulation and the experiments: the locations of the source, tag, reader and RIS, the carrier frequency, the pre-defined codebook and the predefined set of phase shifts (given in Section 5.4). For both the simulations and the experiments, all reflection beams of the codebook and all phase shifts are tested. For each pair of $\mathbf{b} \in \boldsymbol{B}$ and δ, the contrast is assessed either by simulation or by direct experimental measurement at the reader side. In each case, the corresponding simulated BER and measured BER is derived. In addition, we conduct measurements in the absence of the RIS to provide a reference for comparison.

In Figure 5-9-a) and b), we observe the simulated BER and measured BER, respectively, as a function of the index (n) of the reflected beam applied $\mathbf{b}^{(n)}$ and the applied phase shift δ. As expected, we observe, in Figure 5-9, by simulations and experiments, that some pairs of reflected beam and beam phase-shift improve the performance: i.e., these correspond to the yellow pairs

that minimize the BER.

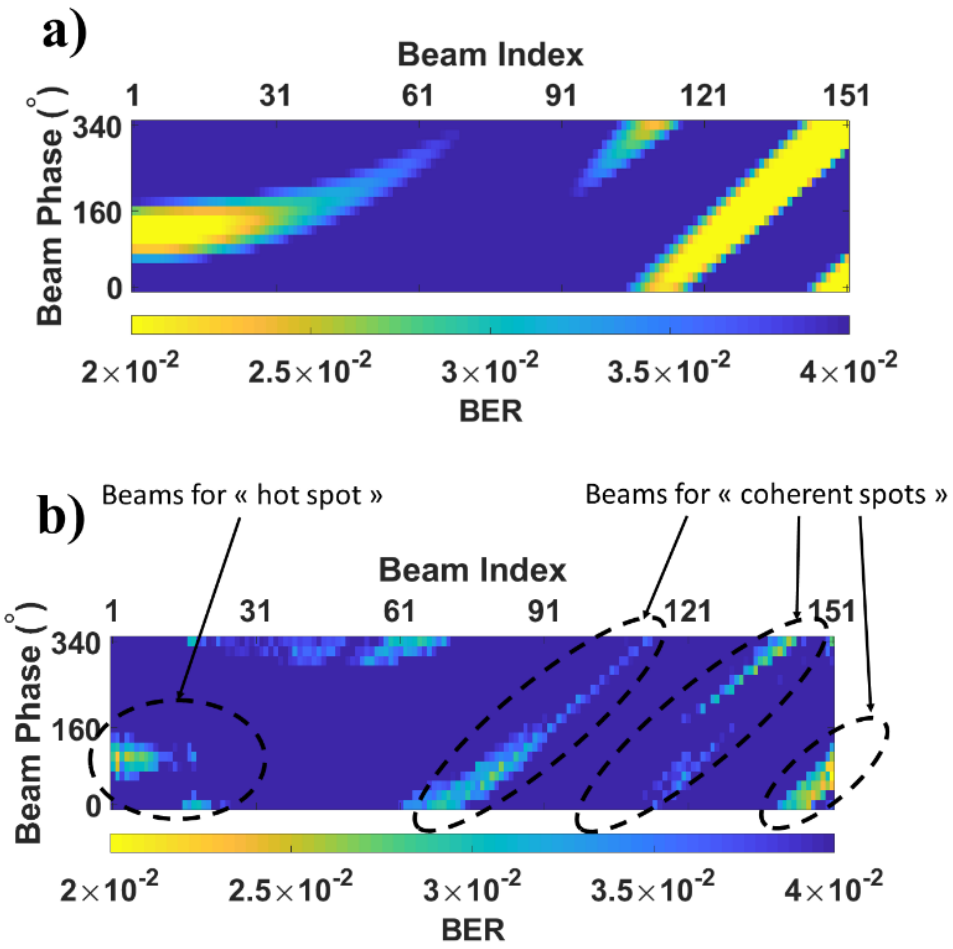

Figure 5-9 Simulation (a) and experimental (b) results of the BER achievable depending on the beam of the codebook and the phase shift applied to the beam.

As expected, hot spots on the tag can be created with some reflected beams between 1 and 31 and with an optimised beam phase-shift fulfilling the condition in (5-13). One example of such reflected beam (the reflected beam 1) is illustrated in Figure 5-9-a), where the simulated spatial map of the reflected signal strength is plotted in dB color scale. We observe, in this example, that the reflected beam 1 creates a hot spot on the tag thanks to its main lobe, whereas the reader receives almost no signal from the RIS. We also observe in Figure 5-9-b) that, for the reflected beam 1, the condition (5-13) is approximatively obtained for $\delta = 140°$.

As expected, coherent spots can be obtained with several beams between 60 and 151 and with an optimized beam phase-shift verifying the condition in (5-15). Two examples of such beams (the reflected beams 68 and 145, respectively) are illustrated in Figure 5-10-b) and c), with simulated maps of the reflected signal strength in dB color scale. As illustrated in Figure 5-10-b) and c), respectively, the reflected beams 68 and 145, respectively, create coherent spots on both the tag and the reader, thanks to their main and side lobes. For both the reflected beams 68 and

145, we observe in Figure 5-9.b) that the coherent condition in (5-15) is approximatively obtained for $\delta = 0°$.

We note that, in the simulated reflected beams, we did not take into account the mutual coupling. Hence, accurate information on the direction of the main lobe is obtained whereas the side lobes may be overestimated.

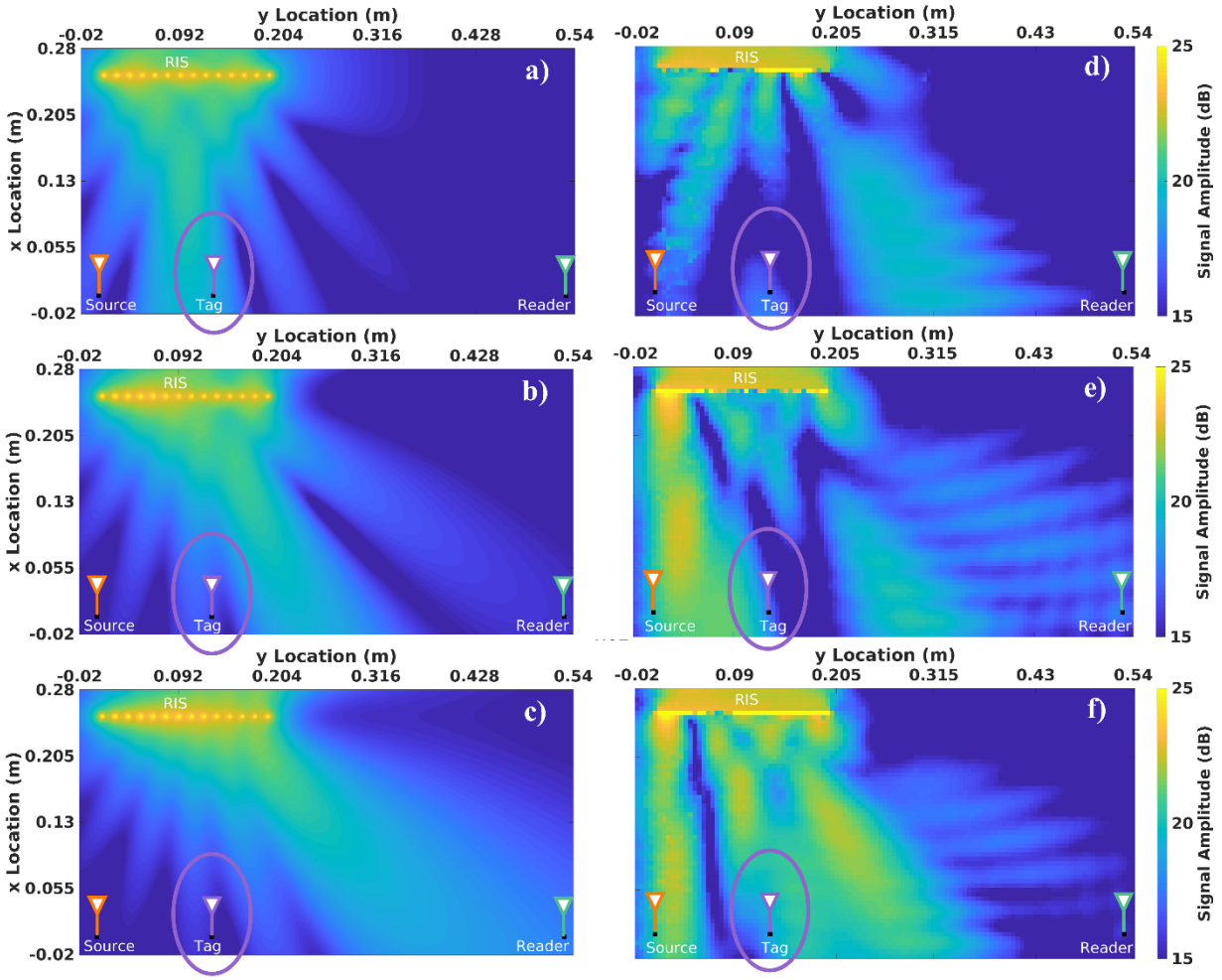

Figure 5-10 Map illustrations of the beamformed reflected signal of the RIS for the reflection phase coefficient of beam 1 a),d) and beam 68 b),e) beam 145 c),f) from the codebook: (a)-(c) shows the results obtained with the simple model and (d)-(f) show the results obtained through full-wave simulations in Ansys HFSS.

The results reported in Figure 5-10 are obtained as follows.

- ***Simplified model***. Given the locations of the source, tag, RIS, and reader in Figure 5-8, three pairs of beam and phase shift are considered. The field scattered by the RIS is determined by using the simplified model for the RIS and the simple analytical model from section 5.2. However, we account for the fact that the amplitude of the reflection coefficient of each unit cell is dependent of the applied phase shift (and the unit cell control voltage).

- ***Full-wave simulations in Ansys HFSS.*** We simulate the entire RIS structure in Ansys HFSS by considering the actual scattering from each unit cell as illustrated in Figure 5-6. The same pairs of beam and phase shift as for the simplified model are considered, but no assumption

on the modeling of the unit cells is made. In particular, the mutual coupling among the unit cells of the RIS is implicitly considered. In addition, the finite size of the RIS is taken into account in the full-wave simulations and no periodic boundary conditions at the unit cell level are applied in this case.

The results illustrated in Figure 5-10 show, as expected, that some differences exist between the predictions obtained by using (5-10), as compared with those obtained with accurate full-wave simulations. We note, however, that the simplified model for the RIS well predicts the direction of the reflected beam of interest. The mismatch between the simple model and the full-wave simulations in Ansys HFSS can be reduced by enriching the model for the RIS proposed at the expenses of a higher modeling and optimization complexity. Also, it needs to be mentioned that the tag in Figure 5-10 is located near the Fraunhofer's far-field distance, which in part justifies the mismatch in Figure 5-10.

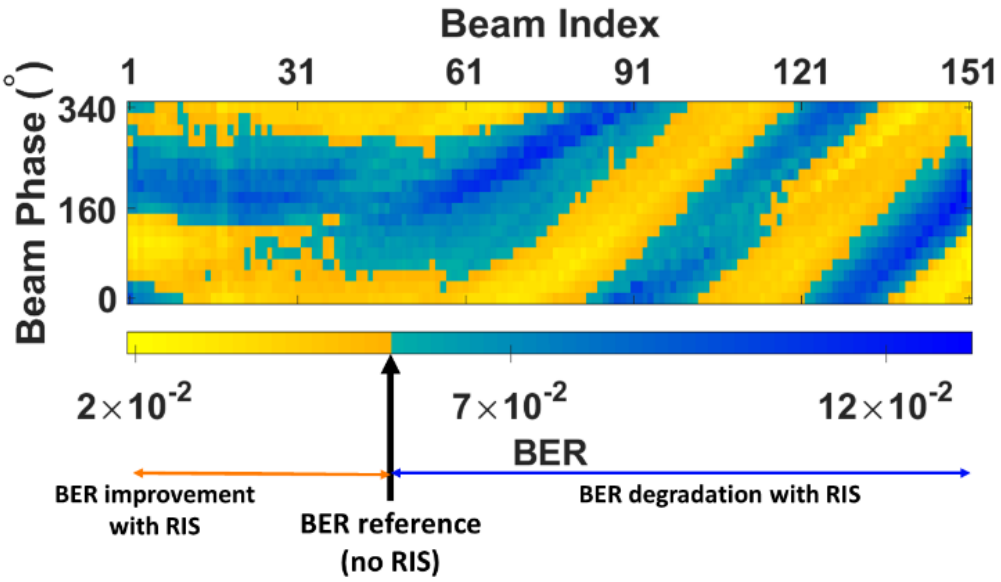

Figure 5-11 Experimental results of the BER improvement/degradation due to the RIS depending on the beam of the codebook and the phase shift applied to the beam.

Finally, in Figure 5-11, we provide a performance comparison of the AmBC system with and without RIS. In the absence of the RIS, the system attains a reference BER value of 5.37×10^{-2} that has been assessed through experimental measurements. In the presence of the RIS, the system attains a BER that is plotted in Figure 5-11 as a function of the beam and phase shift pairs, in color scale. The chosen color scale highlights BER values exceeding the reference BER value (in blue) and BER values better than the reference BER value (in yellow). In yellow, we hence observe the pairs of $\mathbf{b}$ and δ that improve the BER compared to the configuration without RIS, whereas, in blue we have the RIS configurations that degrade the system performance.

These experimental results demonstrate that, assisted by an RIS that uses a codebook-based reflection beamforming scheme whose beams are chosen among a set of pre-defined beams for pre-defined locations and whose beam phase shifts are selected among a set of predefined values,

the BER performance of an AmBC system can be improved.

5.6. CONCLUSION

In this chapter, we have demonstrated experimentally that RISs can improve the performance of AmBC systems. The proposed RIS is able to realize pairs of a reflected beam (belonging to a codebook) and a beam phase-shift that improve the tag-to-reader bit-error-rate. Since the RIS controls the reflected signal, a hot spot on the tag or coherent spots on the tag and the reader can be created to assist the communication between the tag and the reader. Future studies will evaluate more general codebooks that could be applied in different setups and also ML algorithms to optimize the phase reflection coefficients.

Chapter 6

Conclusion and Perspectives

6.1. Conclusion

Internet of things connects billions of devices that communicate information between each other. IoT devices are used for different purposes in a lot of application domains. For example, they can be used for smart tracking, smart monitoring, etc. and in such applications the mobility is an important aspect of IoT device. To combine the mobility of the device and the communication features, wireless technology is widely used in IoT. Wireless communications for IoT devices is very challenging because, it must be at the same time ultra-low power to extend the lifetime of the device and sufficiently high range to be used in many different scenarios.

Recently, the technology named AmBC has been proposed for IoT. This technique is filling the low power requirement for IoT devices. The principle of AmBC is to modulate the backscattering of the electromagnetic waves existing in the environment. In this way a tag can transmit information to a reader without generating additional signal. Therefore, the AmBC tag can be very low power. This principle is so low consuming that the tags can harvest energy from their environment with a solar panel or a rectenna for example.

This technology has significant benefits that can enhance IoT communications, however, the range of communications between a tag and a reader is still very limited. Indeed, the performance of this technology highly depends on the quality of the ambient signal. Two unfavorable scenarios can happen: the tag may not be sufficiently illuminated or the reader may be strongly interfered.

In this thesis we proposed to improve AmBC systems thanks to future mobile networks. We investigated three promising technologies that have been developed recently.

First we have shown that the polarization of the signal can be exploited to improve the robustness of AmBC. We investigated the compact reconfigurable antenna technology, developed for spatial modulation, such antennas can be tuned to obtain different radiation patterns with different polarizations. This antenna technology can be implemented on the tag side and by

switching between different patterns the tag can be better detected by the reader. We studied this system theoretically, by simulation and finally we experimentally demonstrated that reconfigurable antenna can enhance AmBC systems.

Secondly, we investigated the AmBC with the 5G network equipments. This new generation of mobile network includes many new features that can be exploited for AmBC. More specifically we studied the mMIMO antennas deployed in base stations that enhance mobile communication thanks to the spatial diversity. We demonstrated that these mMIMO antennas can be used as the source or the reader in AmBC corresponding to the 5G downlink and uplink scenarios, respectively. In a downlink scenario the mMIMO antenna can beamform the signal to create hot spots on tag locations and good reception spot on the reader location. We show that this is possible considering a stable channel and a UE that trains the source to beamform on the specified locations. In an uplink scenario, we have shown that the mMIMO antenna, used as the reader, can exploit the spatial diversity to improve the sensibility of the detection. Additionally, more complex scheme can be implemented to improve the detection of the tag message.

Finally, we have demonstrated that the next generation of mobile networks can be designed to assist AmBC. The new reconfigurable intelligent surface paradigm is currently studied and envisaged for the 6G network. This technology enables smart radio environment, meaning that the propagation environment can be controlled. Practically, this is possible thanks to a large number of tunable elementary cells in the RIS. Therefore, we have demonstrated that an RIS can partially control the ambient signal to provide a good quality signal on the tag and reader location to assist the AmBC system.

6.2. FUTURE PERSPECTIVES

We list in the sequel potential directions for future works.

Further studies regarding the polarization-based reconfigurable tag concentrate on the reconfigurable antenna. For example, the antenna can be optimized regarding the frequency of the ambient signal to reduce its size to be easily implemented in IoT devices. From the analytical side the model can be enriched by taking into account the joint effects of the reconfigurable antenna gain, directivity and polarization.

For AmBC friendly-5G systems, next studies regarding the downlink configuration should focus on experimental validation of the use of training devices and should explore alternative solutions for radio propagation channels in line-of-sight, and improvements exploiting channel coding. Future studies concerning the uplink configuration with the mMIMO reader should assess the performance of the AmBC on more complex propagation channels, outside anechoic chamber in a more realistic environment. Moreover thanks to the complexity of the detector, multi-state tags could be implemented and detected by such a reader.

For the RIS-assisted system, the codebook of beams presented was based on path difference for the RIS cells determined for pre-defined locations of the source and the RIS. It would be interesting to determine and evaluate more general codebooks that could be applied in different setups. Additionally, it would be interesting to optimize the phase-shifts of the RIS cells by using ML algorithms. Finally, from the experimental side the setup of the RIS prototype could be improved to control all cells independently instead of the limiting the control to fourteen columns. The control of the reflected could therefore be evaluated in a 3-dimensionnal environment.

Résumé (Français)

1. INTRODUCTION

L'internet des objets (IoT) désigne le réseau qui connecte les objets physiques [1]. Un objet connecté, IoT possède par exemple des capteurs et génère des données qui sont communiquées à travers un réseau, par exemple les objets connectés peuvent être du type montre connectée, dispositif de localisation, caméra de sécurité, etc. Ces objets connectés peuvent être de nature radicalement différente afin couvrir des applications dans divers domaines tels que la santé, l'industrie, les réseaux de capteurs sans-fil, la maison intelligente, etc. À mesure que l'IoT évolue, de nouveaux cas d'utilisation et de nouvelles applications sont développés [2]. L'IoT est une technologie récente et très prometteuse, le marché associé est dynamique et en pleine croissance. Notamment, le nombre d'objets connectés ne cesse d'augmenter et, selon des études, il aurait atteint 10 milliards en 2018 et il est prévu qu'il atteigne 25 milliards à la fin de 2021 [3-7].

Les caractéristiques essentielles d'un dispositif connecté sont la capacité de mesurer une certaine caractéristique physique et de transmettre les données à un dispositif maître afin de les analyser. Deux familles de technologies peuvent être utilisées pour la communication des données : la technologie sans fil et la technologie filaire. La technologie filaire a été largement utilisée pour la communication, mais elle est difficile à mettre en œuvre car elle nécessite le déploiement de câbles entre les dispositifs fixes et une passerelle vers le réseau. La technologie filaire est donc limitée et coûteuse, mais elle a l'avantage d'être très sûre et fiable. La deuxième catégorie correspond à la technologie sans fil qui est plus flexible et pour laquelle les dispositifs peuvent être déployés plus facilement et à moindre coût.

Dans le contexte de l'IoT, la technologie sans fil fait face à deux défis qui sont la portée de la communication et la durée de vie du dispositif. Considérant ces deux points clés, de nouvelles technologies ont été proposées : la radio-identification (RFID) [8], les réseaux étendus à longue portée (LoRAWAN) [9], Zigbee [10], Bluetooth [11], etc. Chaque technologie offre des avantages spécifiques pour diverses applications, par exemple, les dispositifs RFID sont très

faible consommateurs d'énergie, tandis que la technologie LoRaWAN permet de réaliser des communications à longue portée. En fonction des exigences des applications, différentes solutions IoT peuvent être envisagées. La communication par rétrodiffusion ambiante (AmBC) est une technologie récente et prometteuse qui permet d'atteindre une très longue durée de vie des dispositifs [12]. Cette technologie permet une communication avec très peu d'énergie, de sorte que les dispositifs peuvent être auto-alimentés en récupérant l'énergie de la lumière du soleil ou même des ondes radiofréquences (RF). De même que la technologie RFID, les dispositifs de rétrodiffusion ambiante transmettent les données de manière passive. La rupture de la technologie AmBC par rapport aux autres technologies de communication sans fil est qu'elle "réutilise" les ondes EM de l'environnement.

Plus concrètement, dans la technologie AmBC, un dispositif appelé tag module le champ RF provenant d'une source RF ambiante, comme une tour de télévision [12], un point d'accès Wi-Fi [13], une station de base, etc. Naturellement, le signal rayonné par la source ambiante est déjà modulé et répond aux normes de la technologie de la source. Néanmoins, le tag de rétrodiffusion ambiante module le signal ambiant à un rythme lent, de sorte que la modulation du tag peut être considérée comme une variation du canal de propagation par le récepteur traditionnel du signal ambiant et n'est donc pas affecté par les tags AmBC. Cependant, un récepteur dédié à l'AmBC, aussi appelé reader, est capable de détecter l'information modulée par le tag dans le signal ambiant. En général, le reader utilise les variations de l'amplitude du champ rétrodiffusé induites par le tag. Plus précisément, dans la mise en œuvre la plus simple, le tag module l'amplitude du signal ambiant avec deux états différents : dans un état, le tag réfléchit les ondes ambiantes dans toutes les directions, c'est-à-dire que le tag rétrodiffuse le signal, tandis que dans un deuxième état, le tag est presque transparent au signal EM et n'a presque aucun impact sur le signal ambiant. En passant électroniquement d'un état à l'autre, le tag module le signal rétrodiffusé en fonction du message à transmettre, ce qui entraîne des variations du niveau de puissance du signal ambiant au niveau du reader. À partir de ces variations, le lecteur peut décoder le signal pour récupérer le message du tag.

Cette technologie permet donc aux dispositifs connectés de communiquer des informations à un reader sans émettre d'ondes supplémentaires. À l'heure où l'on s'interroge sur les effets des ondes électromagnétiques, cette technique récente vise à "recycler" les ondes électromagnétiques et donc à améliorer l'efficacité spectrale des signaux radio. Elle permet également une communication à ultra-basse consommation pour l'IoT car l'émission radio est l'une des parties les plus consommatrices des dispositifs sans fil. Cette caractéristique est très importante dans la conception des dispositifs IoT, de sorte qu'ils pourraient être déployés sans batterie et uniquement alimentés par la récupération d'énergie.

La recherche sur les technologies de communication à faible puissance correspond à une autre préoccupation de notre monde actuel : l'écologie liée à la consommation d'énergie et en particulier l'émission de gaz à effet de serre. À cet égard, les "technologies de l'information" représentent

4 % des émissions mondiales de gaz à effet de serre [14]. Il est donc essentiel de développer des technologies de communication susceptibles de réduire l'impact écologique global.

Dans le domaine des télécommunications, de nouveaux défis sont à relever et doivent être résolus afin de parvenir à un monde durable. Compte tenu des préoccupations actuelles, les systèmes AmBC peuvent être considérés comme une étape de l'évolution vers le futur des communications [15]. Alors que la cinquième génération de réseaux mobiles (5G) est actuellement en cours de déploiement et vise un débit plus important, une latence plus faible et la connexion de millions de dispositifs ou plus, la prochaine génération pourrait également prendre en compte l'impact écologique des télécommunications. La technologie AmBC pourrait être développée et, si elle est suffisamment satisfaisante, promue auprès des entités de normalisation pour les normes des prochaines générations.

2. CONTEXTE

Cette technologie prometteuse qui "réutilise" les ondes électromagnétiques ambiantes présente également certains inconvénients du fait que le tag n'émet aucun signal. En effet, dans sa forme la plus simple, cette technologie peut être sujette à de forts effets d'interférences qui réduisent considérablement la portée de communication et le débit de données.

Dans cette thèse, nous cherchons à développer un cadre théorique pour la propagation du signal dans le contexte des AmBCs, à déterminer les limites de cette technologie, à proposer des améliorations à ces systèmes en tenant compte des dernières avancées de la recherche, et à évaluer les performances des systèmes AmBC. Nous étudions spécifiquement l'évolution des AmBC en tenant compte des technologies actuelles dans le domaine de la modulation spatiale (SM) [16], des réseaux 5G [17] et également des dernières technologies émergentes pour la sixième génération de réseaux mobiles (6G) [18].

Nous étudions trois évolutions différentes des AmBCs pour améliorer les performances de ces systèmes, à savoir :

- Dans le chapitre 3, nous proposons d'exploiter la diversité de polarisation du canal de propagation pour améliorer les performances et la robustesse des systèmes AmBC. Ce chapitre est partiellement basé sur les résultats obtenus dans le cadre d'un projet consacré au SM, nous montrons qu’il est possible d'améliorer la robustesse et grâce à des antennes compactes reconfigurables.

- Dans le chapitre 4, nous étudions le potentiel des réseaux 5G pour améliorer les performances et surmonter les limitations des systèmes AmBC. En effet, le réseau 5G étant en cours de déploiement, il pourrait apporter des avantages à la technologie AmBC, grâce à ses nouvelles fonctionnalités. Plus précisément, nous nous concentrons sur les antennes à « entrées multiples sorties multiples » (MIMO) utilisées dans les réseaux 5G afin de faciliter la détection des tags de rétrodiffusion ambiante et d’améliorer la qualité du signal rétrodiffusé. Nous proposons de rendre

les tags AmBC compatibles pour les réseaux 5G.

- Dans le chapitre 5, nous étudions les surfaces intelligentes reconfigurables (RIS), qui est une technologie récente actuellement envisagée pour les futurs réseaux mobiles. Les RIS ont la capacité de réfléchir les signaux de manière contrôlée. Dans des cas d'utilisation réels, les RIS pourraient être déployés dans l'environnement pour augmenter la diversité du canal de propagation et donc d'améliorer la qualité du signal dans un réseau. Nous proposons d'utiliser les RIS pour aider les systèmes AmBC en améliorant les performances de la liaison entre le tag et le reader.

Pour chaque étude, nous proposons une méthode pour évaluer les avantages de l'évolution du système proposé. Tout d'abord, nous définissons un système de référence correspondant aux systèmes AmBC actuels et nous déterminons avec des données mesurables, une métrique de performance. Sur la base de ce système de référence, nous pouvons déterminer l'amélioration ou la détérioration due aux évolutions proposées. La performance de ce système est principalement évaluée sur la base de deux métriques :

- le débit de données réalisable : le nombre de bits qu'un tag AmBC peut transmettre par seconde.

- la portée de la communication : elle correspond à la distance à laquelle les tags peuvent être détectés par un lecteur.

Ces deux métriques sont évidemment fortement dépendantes. Par conséquent, dans la plupart de ces travaux, une seule métrique sera évaluée.

D'autres paramètres existent et peuvent être évalués, tel que la consommation d'énergie. Cependant, dans ce travail, nous utilisons des diodes conventionnelles ou des varicaps dont l'efficacité énergétique a déjà été évaluée et qui ont montré qu'ils étaient plus performants que les autres technologies. Par conséquent, l'aspect consommation d'énergie qui est fortement lié aux avantages de cette technologie n'est pas abordé dans ce travail.

En termes de performance, les scénarios peuvent être évalués sur la base de trois approches différentes et complémentaires : théorique, simulation ou expérimentale. Dans cette thèse, nous étudions les évolutions potentielles des systèmes AmBC selon ces trois perspectives. Nous proposons d'établir un modèle théorique du système en considérant et justifiant différentes hypothèses "simples ". Nous évaluons, à partir des approches théoriques et de simulation, les performances du système pour différentes configurations. Enfin, grâce à des expérimentations prenant en compte la complexité de l'environnement, nous validons les résultats théoriques et de simulation pour certaines configurations spécifiques.

3. CONTRIBUTIONS

Nos principales contributions s'articulent comme suit :

Dans le chapitre 3, nous considérons un système AmBC composé d'une source ambiante, d'un reader et d'un tag capable de changer la polarisation de son antenne. Nous proposons d'améliorer le tag AmBC en utilisant la technologie des antennes reconfigurables développée pour la SM. Nous introduisons un tag reconfigurable en polarisation pour améliorer la robustesse de la liaison tag-reader face à l'interférence directe source-reader. Nous savons que la reconfigurabilité de l'antenne du tag peut augmenter l'efficacité spectrale, similairement à l'utilisation faite en SM. Ainsi, nous utilisons cette propriété pour améliorer la robustesse du système.

Nous comparons deux schémas de codage qui exploitent la diversité de polarisation. Dans le premier schéma de codage considéré, le tag, comme tout tag standard à deux états, envoie son message en passant d'un état de "rétrodiffusion" à un état "transparent". En pratique, cela est réalisé en commutant l'impédance de charge de l'antenne entre deux impédances différentes. Avec cette approche, le tag envoie le même message plusieurs fois, en utilisant à chaque fois un diagramme de rayonnement différent correspondant à un état de polarisation. Par conséquent, on s'attend à ce que le reader reçoive un signal de bonne qualité sur au moins un état de polarisation. Nous introduisons un deuxième schéma de codage dans lequel les données sont codées en passant d'un mode de rayonnement à un autre. Selon le principe SM, chaque mode est associé à une séquence de bits. Comme pour le premier schéma, nous pensons qu'un choix optimisé des états de polarisation améliorera les performances du système.

Pour évaluer les avantages du tag proposée, nous présentons un modèle simple du tag qui peut être étudié théoriquement et numériquement à l'aide d'un logiciel de simulation électromagnétique basé sur la méthode des moments (MoM). Nous évaluons les performances du système par simulation en utilisant ce modèle. Enfin, nous évaluons également expérimentalement la mise en œuvre proposée en utilisant différentes antennes, y compris des antennes reconfigurables. Ce travail a donné lieu à la publication de deux articles [19], [20].

Nous proposons dans le chapitre 4 d'améliorer les performances du système de rétrodiffusion ambiante en utilisant des équipements 5G de type « massive multiple-input multiple-output » (mMIMO). Dans les réseaux 5G, les tags AmBC pourraient communiquer avec des stations de base ou des smartphones. Nous considérons deux configurations, la transmission 5G en liaison montante et en liaison descendante, où la source ambiante du signal peut être soit la station de base (liaison descendante), soit le smartphone (liaison montante).

Nous étudions d'abord la configuration de la liaison descendante et nous exploitons la capacité de formation de faisceau de l'antenne source mMIMO. Nous proposons d'utiliser la capacité de formation de faisceau de l'antenne source pour créer des zones de forte puissance pour les tags et des zones de bonne réception pour les readers. Nous considérons deux types de zones de bonne réception : une "zone de faible puissance" avec une très faible interférence source-reader ; et une "zone cohérente" avec une interférence source-reader mais étant cohérente (c'est-à-dire en phase) avec le signal rétrodiffusé. Nous avons développé une approche en plusieurs étapes qui consiste en :

- une phase d'entraînement pendant laquelle la station de base acquiert le canal de propagation pour créer la matrice de précodage,

- une phase de formation de faisceau, au cours de laquelle la station de base détermine le précodage sur la base de l'estimation du canal et transmet le signal de diffusion formé par faisceau qui crée les différentes zones,

- une phase de communication, dans laquelle, finalement, le tag rétrodiffuse le signal au reader.

Dans cette étude, nous comparons trois précodeurs différents, chacun ayant un impact différent sur le signal rétrodiffusé. Nous évaluons les performances du système pour les trois configurations par simulation dans un canal de propagation de Rayleigh. Ce travail a donné lieu à la publication d'un article [21].

Dans un second scénario, nous étudions la configuration de la liaison montante où l'antenne mMIMO est utilisée du côté du reader pour détecter les messages rétrodiffusés par le tag. Nous proposons d'exploiter la diversité spatiale du canal en utilisant une antenne du côté du reader composé de 64 éléments. Nous évaluons expérimentalement un scénario de transmission en liaison montante dans une chambre anéchoïque. Dans un premier temps, un appareil mobile, considéré comme la source, envoie des signaux pilotes au reader mMIMO. Le tag AmBC située entre le mobile et le reader a un impact sur le canal de propagation et comme le tag considéré a deux états : un état de rétrodiffusion et un état transparent, le canal de propagation entre le mobile et le reader dépend de l'état du tag. Du côté du reader, l'estimation du canal de propagation est faite pour les états rétrodiffusant et transparent du tag. Comme chaque état code un bit du message du tag, le reader est capable de décoder le message du tag avec une meilleure sensibilité grâce au grand nombre d'antennes. Nous proposons d'évaluer les performances du système en utilisant un estimateur d'erreur des moindres carrés (LSE) pour détecter l'état du tag. Ce travail a donné lieu à la publication d'un article [22].

Dans le chapitre 5, nous étudions les futurs réseaux mobiles et la technologie émergente des RISs. Nous proposons un nouveau système AmBC assisté par des RIS, à déployer sur un bureau d'information exposant des tags qui ont pour but d’être lus. Dans le système proposé, les RISs sont utilisées pour améliorer la transmission entre les tags et les readers. L'avantage des RISs est de permettre un contrôle partiel du canal de propagation. Cette propriété est particulièrement pertinente dans le cas de la technologie AmBC où la source ne peut être contrôlée.

Nous évaluons la capacité de formation de faisceau de manière passive des RISs afin d'aider les tags AmBC. Nous proposons une méthode où la RIS reflète le signal dans la direction du tag. Tout d'abord, la RIS peut choisir un faisceau parmi une sélection prédéfini de faisceaux. Chaque faisceau est conçu pour réfléchir les ondes provenant de l'emplacement exact de la source vers l'un des emplacements prédéfinis sur le bureau. Deuxièmement, la RIS peut aussi appliquer un déphasage commun à tous ses éléments. La RIS teste plusieurs paires de faisceaux et de déphasage commun. À chaque fois, le lecteur apporte un retour sur la qualité des performances.

La RIS et le reader recherchent ensemble la paire de faisceau et de déphasage commun qui maximise les performances. Nous espérons, avec cette approche, améliorer le taux d'erreur binaire (BER), par rapport au scénario sans RIS, soit en créant une "zone de forte puissance" sur le tag ce qui va amplifier le signal rétrodiffusé, soit en créant des "zones cohérentes" à la fois sur le tag et sur le reader, de telle sorte que toutes les ondes réfléchies par la RIS se combinent de manière cohérente avec toutes les autres ondes, lorsqu'elles arrivent au niveau du reader pour améliorer le contraste du signal reçu. Nous proposons de valider cette approche par des expériences. Ce travail a conduit à la publication de deux articles [23], [24].

4. PERSPECTIVES FUTURES

Concernant le tag reconfigurable en polarisation, les futurs travaux de recherche pourraient se concentrer sur les prototypes d'antennes reconfigurables. Par exemple, l'antenne reconfigurable du tag peut être optimisée en ce qui concerne la fréquence du signal ambiant afin de réduire sa taille pour être facilement mise en œuvre dans les dispositifs IoT. Du point de vue analytique, le modèle peut être enrichi en prenant en compte les effets conjoints du gain, de la directivité et de la polarisation de l'antenne reconfigurable.

Pour les systèmes le réseau 5G adapté aux AmBC, les prochaines études concernant la configuration de la liaison descendante devraient se concentrer sur la validation expérimentale de l'utilisation de dispositifs d'entraînement pour focaliser le signal sur les zones prédéfinies, explorer des solutions alternatives pour les canaux de propagation radio en ligne de vue et explorer des améliorations exploitant le codage de canal. Les études futures concernant la configuration de la liaison montante avec le reader mMIMO devraient évaluer les performances de l'AmBC sur des canaux de propagation plus complexes, hors chambre anéchoïque, dans un environnement plus réaliste. De plus, grâce à la complexité du détecteur, des tags à plusieurs états pourraient être mis en œuvre et détectés par un tel reader.

Pour le système AmBC assisté par la RIS, la formation de faisceaux présentée était basée sur la différence de chemin pour chaque cellule de la RIS déterminées pour des emplacements prédéfinis de la source et de la RIS. Il serait intéressant de déterminer et d'évaluer des configurations de faisceaux plus générales qui pourraient être appliquées dans différents environnements. De plus, il serait intéressant d'optimiser le contrôle des cellules de la RIS en utilisant des algorithmes ML. Enfin, du point de vue expérimental, la configuration du prototype de la RIS pourrait être améliorée pour contrôler toutes les cellules indépendamment au lieu de limiter le contrôle aux différentes colonnes. Le contrôle de la réflexion pourrait ainsi être évalué dans un environnement tridimensionnel.

References

[1] F. Mattern and C. Floerkemeier, “From the Internet of Computers to the Internet of Things,” in *From Active Data Management to Event-Based Systems and More: Papers in Honor of Alejandro Buchmann on the Occasion of His 60th Birthday*, K. Sachs, I. Petrov, and P. Guerrero, Eds. Berlin, Heidelberg: Springer Berlin Heidelberg, 2010, pp. 242–259.

[2] “Le monde des objets connectés : des écosystèmes en ébullition - Hello Future Orange,” in *Hello Future*, Dec. 16, 2019. https://hellofuture.orange.com/fr/le-monde-des-objets-connectes-des-ecosystemes-en-ebullition/.

[3] R. van der Meulen “Gartner Says 8.4 Billion Connected ‘Things’ Will Be in Use in 2017, Up 31 Percent From 2016.” *Gartner*, Feb. 7, 2017. https://www.gartner.com/en/newsroom/press-releases/2017-02-07-gartner-says-8-billion-connected-things-will-be-in-use-in-2017-up-31-percent-from-2016.

[4] P. Newman, “The Internet Of Things 2020: Here’s what over 400 IoT decision-makers say about the future of enterprise connectivity and how IoT companies can use it to grow revenue,” in *Business Insider*, Mar. 2020. https://www.businessinsider.com/internet-of-things-report.

[5] K. L. Lueth “State of the IoT 2018: Number of IoT devices now at 7B – Market accelerating.” in *IoT Analytics*, Aug. 2018. https://iot-analytics.com/state-of-the-iot-update-q1-q2-2018-number-of-iot-devices-now-7b/.

[6] “A Guide to the Internet of Things” *Intel*. https://www.intel.com/content/dam/www/public/us/en/images/iot/guide-to-iot-infographic.png.

[7] L. Columbus, “10 Charts That Will Challenge Your Perspective Of IoT’s Growth,” *Forbes*. Jun. 2018. https://www.forbes.com/sites/louiscolumbus/2018/06/06/10-charts-that-will-challenge-your-perspective-of-iots-growth/.

[8] K. Finkenzeller, *RFID Handbook: Fundamentals and Applications in Contactless Smart Cards, Radio Frequency Identification and Near-Field Communication*. 2010. [Online]. Available: https://ieeexplore.ieee.org/book/8040493.

[9] K. Mikhaylov, J. Petäjäjärvi, J. Haapola, and A. Pouttu, “D2D communications in LoRaWAN Low Power Wide Area Network: From idea to empirical validation,” in *2017 IEEE International Conference on Communications Workshops (ICC Workshops)*, May 2017, pp. 737–742.

[10] EETimes, “EETimes - ZigBee applications - Part 1: Sending and receiving data,” *EETimes*, Jul. 02, 2010. https://www.eetimes.com/zigbee-applications-part-1-sending-and-receiving-data/.

[11] C. Bisdikian, “An overview of the Bluetooth wireless technology,” *IEEE Commun. Mag.*, vol. 39, no. 12, pp. 86–94, Dec. 2001.

[12] V. Liu, A. Parks, V. Talla, S. Gollakota, D. Wetherall, and J. R. Smith, “Ambient Backscatter: Wireless Communication Out of Thin Air,” p. 12

[13] B. Kellogg, A. Parks, S. Gollakota, J. R. Smith, and D. Wetherall, “Wi-fi backscatter: internet connectivity for RF-powered devices,” in *Proceedings of the 2014 ACM conference on SIGCOMM*, Chicago Illinois USA, Aug. 2014, pp. 607–618.

[14] F. Bordage *et al.*, “Empreinte environnementale du numérique mondial,” *Green IT* . p. 40, 2019.

[15] W. Zhang *et al.*, “A green paradigm for Internet of Things: Ambient backscatter communications,” *China Commun.*, vol. 16, no. 7, pp. 109–119, Jul. 2019.

[16] R. Y. Mesleh, H. Haas, S. Sinanovic, C. W. Ahn, and S. Yun, “Spatial Modulation,” *IEEE Trans. Veh. Technol.*, vol. 57, no. 4, pp. 2228–2241, Jul. 2008.

[17] F. W. Vook, A. Ghosh, E. Diarte, and M. Murphy, “5G New Radio: Overview and Performance,” in *2018 52nd Asilomar Conference on Signals, Systems, and Computers*, Oct. 2018, pp. 1247–1251.

[18] E. C. Strinati *et al.*, “Wireless Environment as a Service Enabled by Reconfigurable Intelligent Surfaces: The RISE-6G Perspective,” *arXiv:2104.06265*, Apr. 2021.

[19] R. Fara, D.-T. Phan-Huy, A. Ourir, M. Di Renzo, and J. de Rosny, “Robust Ambient Backscatter Communications with Polarization Reconfigurable Tags,” in *2020 IEEE 31st Annual International Symposium on Personal, Indoor and Mobile Radio Communications*, Aug. 2020, pp. 1–7.

[20] R. Fara *et al.*, “Polarization-Based Reconfigurable Tags for Robust Ambient Backscatter Communications,” *IEEE Open J. Commun. Soc.*, vol. 1, pp. 1140–1152, 2020.

[21] R. Fara, D.-T. Phan-Huy, and M. D. Renzo, “Ambient backscatters-friendly 5G networks: creating hot spots for tags and good spots for readers,” in *2020 IEEE Wireless Communications and Networking Conference (WCNC)*, May 2020, pp. 1–7.

[22] R. Fara, N. Bel-Haj-Maati, D.-T. Phan-Huy, N. Malhouroux, and M. Di Renzo, “First experimental evaluation of ambient backscatter communications with massive MIMO reader,” in *2020 IEEE 31st Annual International Symposium on Personal, Indoor and Mobile Radio Communications*, Aug. 2020, pp. 1–6.

[23] R. Fara, D.-T. Phan-Huy, P. Ratajczak, A. Ourir, M. Di Renzo, and J. de Rosny, “Reconfigurable Intelligent Surface -Assisted Ambient Backscatter Communications -- Experimental Assessment,” *arXiv:2103.08427*, Apr. 2021.

[24] R. Fara, P. Ratajczak, D.-T. P. Huy, A. Ourir, M. Di Renzo, and J. De Rosny, "A Prototype of Reconfigurable Intelligent Surface with Continuous Control of the Reflection Phase," *arXiv:2105.11862*, May 2021.

[25] U. N. O. and A. Administration, *English: heliograph - Signaling with heliograph near Monument 92. Alaska - Canada border. International Boundary Commission*. 1910. [Online]. Available: https://commons.wikimedia.org/wiki/File:Heliograph.jpg?uselang=fr.

[26] "Backscattering," *American Heritage® Dictionary of the English Language, Fifth Edition. (2011)*.

[27] U. N. W. Service, *Français : Principe du radar: émission d'une impulsion d'onde radio très intense mais brève, l'énergie frappe une cible et une petite portion de l'énergie est retournée au radar.* 2002. [Online]. Available: https://commons.wikimedia.org/wiki/File:Radarops.gif.

[28] Y. Blanchard, "Une histoire du radar en lien avec les mutations du système technique," *Rev. Electr. Electron.*, vol. 2019, pp. 35–46, Jul. 2019.

[29] H. Stockman, "Communication by Means of Reflected Power," *Proc. IRE*, vol. 36, no. 10, pp. 1196–1204, Oct. 1948.

[30] J. Griffin, D. Research, and F. Ave, "The Fundamentals of Backscatter Radio and RFID Systems," p. 90, 2009.

[31] N. V. Huynh, D. T. Hoang, X. Lu, D. Niyato, P. Wang, and D. I. Kim, "Ambient Backscatter Communications: A Contemporary Survey," *IEEE Commun. Surv. Tutor.*, vol. 20, no. 4, pp. 2889–2922, Fourthquarter 2018.

[32] J. Kimionis, A. Bletsas, and J. N. Sahalos, "Increased Range Bistatic Scatter Radio," *IEEE Trans. Commun.*, vol. 62, no. 3, pp. 1091–1104, Mar. 2014.

[33] J. Kimionis, A. Bletsas, and J. N. Sahalos, "Bistatic backscatter radio for power-limited sensor networks," in *2013 IEEE Global Communications Conference (GLOBECOM)*, Dec. 2013, pp. 353–358.

[34] S. H. Choi and D. I. Kim, "Backscatter radio communication for wireless powered communication networks," in *2015 21st Asia-Pacific Conference on Communications (APCC)*, Oct. 2015, pp. 370–374.

[35] J. Kimionis, A. Bletsas, and J. N. Sahalos, "Bistatic backscatter radio for tag read-range extension," in *2012 IEEE International Conference on RFID-Technologies and Applications (RFID-TA)*, Nov. 2012, pp. 356–361.

[36] A. Gati *et al.*, "Key technologies to accelerate the ICT Green evolution -- An operator's point of view," *arXiv:1903.09627*, Mar. 2019.

[37] J. K. Schindler, R. B. Mack, and P. Blacksmith, "The control of electromagnetic scattering by impedance loading," *Proc. IEEE*, vol. 53, no. 8, pp. 993–1004, 1965.

[38] W. C. Barott, "Coherent Backscatter Communications Using Ambient Transmitters and

Passive Radar Processing," in *2014 National Wireless Research Collaboration Symposium*, May 2014, pp. 15–20.

[39] D. Bharadia, K. R. Joshi, M. Kotaru, and S. Katti, "BackFi: High Throughput WiFi Backscatter," *ACM SIGCOMM Comput. Commun. Rev.*, vol. 45, no. 4, pp. 283–296, Aug. 2015.

[40] R. C. Hansen, "Relationships between antennas as scatterers and as radiators," *Proc. IEEE*, vol. 77, no. 5, pp. 659–662, May 1989.

[41] A. Bletsas, A. G. Dimitriou, and J. N. Sahalos, "Backscattering improvement of UHF RFID tag efficiency," in *2010 International Workshop on Antenna Technology (iWAT)*, Lisbon, Portugal, Mar. 2010, pp. 1–4.

[42] A. Bletsas, A. G. Dimitriou, and J. N. Sahalos, "Improving Backscatter Radio Tag Efficiency," *IEEE Trans. Microw. Theory Tech.*, vol. 58, no. 6, pp. 1502–1509, Jun. 2010.

[43] F. Fuschini, C. Piersanti, F. Paolazzi, and G. Falciasecca, "Analytical Approach to the Backscattering from UHF RFID Transponder"

[44] R. Green, "The general theory of antenna scattering." Doctoral dissertation, Ohio State University, 1963.

[45] C. A. Balanis, *Antenna theory: analysis and design*, 3rd Edition, John Wiley and Sons, New York, 2005.

[46] P. V. Nikitin and K. V. S. Rao, "Theory and measurement of backscattering from RFID tags," *IEEE Antennas Propag. Mag.*, vol. 48, no. 6, pp. 212–218, Dec. 2006.

[47] K. Rachedi *et al.*, "Demo Abstract : Real-Time Ambient Backscatter Demonstration," *IEEE INFOCOM 2019 - IEEE Conference on Computer Communications Workshops (INFOCOM WKSHPS)*, pp. 987-988, Apr. 2019.

[48] K. Rachedi, D. T. P. Huy, N. Selmene, A. Ourir, and J. de Rosny, "Spatial characterization of the ambient backscatter communication performance in line-of-sight," in *2019 IEEE International Symposium on Antennas and Propagation and USNC-URSI Radio Science Meeting*, Jul. 2019, pp. 645–646.

[49] Q. Tao, C. Zhong, H. Lin, and Z. Zhang, "Symbol Detection of Ambient Backscatter Systems with Manchester Coding," *arXiv:1804.03512*, Apr. 2018.

[50] M. A. Khan, M. Sharma, and R. B. Prabhu, "FSM based FM0 and Miller encoder for UHF RFID Tag Emulator," in *2009 IEEE International Advance Computing Conference*, Mar. 2009, pp. 1317–1322.

[51] S. N. Daskalakis, J. Kimionis, A. Collado, G. Goussetis, M. M. Tentzeris, and A. Georgiadis, "Ambient Backscatterers Using FM Broadcasting for Low Cost and Low Power Wireless Applications," *IEEE Trans. Microw. Theory Tech.*, vol. 65, no. 12, pp. 5251–5262, Dec. 2017.

[52] G. Wang, F. Gao, R. Fan, and C. Tellambura, "Ambient Backscatter Communication

Systems: Detection and Performance Analysis," *IEEE Trans. Commun.*, vol. 64, no. 11, pp. 4836–4846, Nov. 2016.

[53] F. Engmann, F. A. Katsriku, J.-D. Abdulai, K. S. Adu-Manu, and F. K. Banaseka, "Prolonging the Lifetime of Wireless Sensor Networks: A Review of Current Techniques," *Wirel. Commun. Mob. Comput.*, vol. 2018, p. e8035065, Aug. 2018.

[54] A. S. Adila, A. Husam, and G. Husi, "Towards the self-powered Internet of Things (IoT) by energy harvesting: Trends and technologies for green IoT," in *2018 2nd International Symposium on Small-scale Intelligent Manufacturing Systems (SIMS)*, Apr. 2018, pp. 1–5.

[55] D. T. Phan Huy, *Ambient Backscatter Communication with Solar Tag*. [Online Video]. Available: https://www.dailymotion.com/video/x6urfvz.

[56] A. Eid, J. G. D. Hester, and M. M. Tentzeris, "5G as a wireless power grid," *Sci. Rep.*, vol. 11, no. 1, Art. no. 1, Jan. 2021.

[57] Yuri Tikhov, Il-Jong Song, and Young-Hoon Min, "Rectenna design for passive RFID transponders," in *2007 European Microwave Conference*, Oct. 2007, pp. 995–998.

[58] K. Rachedi, "Antennes Compactes Reconfigurables en Diagramme de Rayonnement pour la Modulation Spatiale MIMO et Introduction aux communications numériques par rétrodiffuseurs," 2019.

[59] S. Guruacharya, X. Lu, and E. Hossain, "Optimal Non-Coherent Detector for Ambient Backscatter Communication System," *IEEE Trans. Veh. Technol.*, vol. 69, no. 12, pp. 16197–16201, Dec. 2020.

[60] J. K. Devineni and H. S. Dhillon, "Non-Coherent Signal Detection and Bit Error Rate for an Ambient Backscatter Link under Fast Fading," in *2019 IEEE Global Communications Conference (GLOBECOM)*, Dec. 2019, pp. 1–6.

[61] N. Fasarakis-Hilliard, P. N. Alevizos, and A. Bletsas, "Coherent Detection and Channel Coding for Bistatic Scatter Radio Sensor Networking," *IEEE Trans. Commun.*, vol. 63, no. 5, pp. 1798–1810, May 2015.

[62] M. D. Renzo, H. Haas, A. Ghrayeb, S. Sugiura, and L. Hanzo, "Spatial Modulation for Generalized MIMO: Challenges, Opportunities, and Implementation,"in Proc. *IEEE*, vol. 102, no. 1, pp. 56–103, Jan. 2014.

[63] M. D. Renzo, H. Haas, and A. Ghrayeb, "Spatial Modulation for MIMO Wireless Systems," *IEEE Tutorial.*, p. 421, 2013. https://hal-supelec.archives-ouvertes.fr/hal-00840278v2/file/SMTutorial_FullSlides.pdf

[64] M. Wen *et al.*, "A Survey on Spatial Modulation in Emerging Wireless Systems: Research Progresses and Applications," *arXiv:1907.02941*, Jul. 2019.

[65] K. M. Humadi, A. I. Sulyman, and A. Alsanie, "Spatial Modulation Concept for Massive Multiuser MIMO Systems," *Int. J. Antennas Propag.*, vol. 2014, p. e563273, Jun. 2014.

[66] M. D. Renzo, H. Haas, and P. M. Grant, “Spatial modulation for multiple-antenna wireless systems: a survey,” *IEEE Commun. Mag.*, vol. 49, no. 12, pp. 182–191, Dec. 2011.

[67] S. M. Alamouti, “A simple transmit diversity technique for wireless communications,” *IEEE J. Sel. Areas Commun.*, vol. 16, no. 8, pp. 1451–1458, Oct. 1998.

[68] D.-T. Phan-Huy *et al.*, “Single-Carrier Spatial Modulation for the Internet of Things: Design and Performance Evaluation by Using Real Compact and Reconfigurable Antennas,” *IEEE Access*, vol. 7, pp. 18978–18993, 2019.

[69] K. Rachedi, D. T. Phan Huy, A. Ourir, and J. de Rosny, “Reconfigurable Split Ring Resonators for Spatial Modulation Communications,” in *2019 13th European Conference on Antennas and Propagation (EuCAP)*, Mar. 2019, pp. 1–5.

[70] A. Ourir, K. Rachedi, D.-T. Phan-Huy, C. Leray, and J. de Rosny, “Compact reconfigurable antenna with radiation pattern diversity for spatial modulation,” in *2017 11th European Conference on Antennas and Propagation (EUCAP)*, Mar. 2017, pp. 3038–3043.

[71] Y. Kokar *et al.*, “First Experimental Ambient Backscatter Communication Using a Compact Reconfigurable Tag Antenna,” in *2019 IEEE Globecom Workshops (GC Wkshps)*, Dec. 2019, pp. 1–6.

[72] P. Portos, P. Ratajczak, and F. Ferrero, “Design of a miniature and reconfigurable antenna system for spatial modulation and ambient backscattering,” in *2020 International Workshop on Antenna Technology (iWAT)*, Feb. 2020, pp. 1–3.

[73] “5G drives the real-time enterprise,” *Orange Business Services*. May 2019. https://www.orange-business.com/en/magazine/5g-drives-realtime-enterprise.

[74] A. Ghosh, “5G New Radio (NR) : Physical Layer Overview and Performance,” *IEEE Communication Theory Workshop*, p. 38, 2018.

[75] A. Ghosh, A. Maeder, M. Baker, and D. Chandramouli, “5G Evolution: A View on 5G Cellular Technology Beyond 3GPP Release 15,” *IEEE Access*, vol. 7, pp. 127639–127651, 2019.

[76] J. H. Bae, A. Abotabl, H.-P. Lin, K.-B. Song, and J. Lee, “An overview of channel coding for 5G NR cellular communications,” *APSIPA Trans. Signal Inf. Process.*, vol. 8, ed 2019.

[77] T. L. Marzetta, “Noncooperative Cellular Wireless with Unlimited Numbers of Base Station Antennas,” *IEEE Trans. Wirel. Commun.*, vol. 9, no. 11, pp. 3590–3600, Nov. 2010.

[78] K. Werner, H. Asplund, D. V. P. Figueiredo, N. Jaldén and B. Halvarsson, "LTE-advanced 8×8 MIMO measurements in an indoor scenario," *2012 International Symposium on Antennas and Propagation (ISAP)*, pp. 750-753, 2012.

[79] M. Pappa, C. Ramesh, and M. N. Kumar, “Performance comparison of massive MIMO and conventional MIMO using channel parameters,” in *2017 International Conference on Wireless Communications, Signal Processing and Networking (WiSPNET)*, Mar. 2017, pp. 1808–1812.

[80] E. G. Larsson, O. Edfors, F. Tufvesson, and T. L. Marzetta, "Massive MIMO for next generation wireless systems," *IEEE Commun. Mag.*, vol. 52, no. 2, pp. 186–195, Feb. 2014.

[81] N. Fatema, G. Hua, Y. Xiang, D. Peng, and I. Natgunanathan, "Massive MIMO Linear Precoding: A Survey," *IEEE Syst. J.*, vol. 12, no. 4, pp. 3920–3931, Dec. 2018.

[82] S. Gunnarsson, J. Flordelis, L. V. der Perre, and F. Tufvesson, "Channel Hardening in Massive MIMO-A Measurement Based Analysis," in *2018 IEEE 19th International Workshop on Signal Processing Advances in Wireless Communications (SPAWC)*, Jun. 2018, pp. 1–5.

[83] S. Wesemann, H. Schlesinger, A. Pascht, and O. Blume, "Measurement and Characterization of the Temporal Behavior of Fixed Massive MIMO Links," in *WSA 2017; 21th International ITG Workshop on Smart Antennas*, Mar. 2017, pp. 1–8.

[84] D. Phan-Huy, S. Wesemann, J. Bjoersell, and M. Sternad, "Adaptive Massive MIMO for fast moving connected vehicles: It will work with Predictor Antennas!," in *WSA 2018; 22nd International ITG Workshop on Smart Antennas*, Mar. 2018, pp. 1–8.

[85] J. D. Griffin and G. D. Durgin, "Multipath fading measurements for multi-antenna backscatter RFID at 5.8 GHz," *2009 IEEE International Conference on RFID*, pp. 322-329, 2009.

[86] C. He, X. Chen, Z. J. Wang, and W. Su, "On the performance of MIMO RFID backscattering channels," *J Wireless Com Network 2012*, p. 357, 2012.

[87] C. Boyer and S. Roy, "Backscatter Communication and RFID: Coding, Energy, and MIMO Analysis," *IEEE Trans. Commun.*, vol. 62, no. 3, pp. 770–785, Mar. 2014.

[88] D. Mishra and E. G. Larsson, "Multi-Tag Backscattering to MIMO Reader: Channel Estimation and Throughput Fairness," *arXiv:1908.08748*, Aug. 2019.

[89] A. N. Parks, A. Liu, S. Gollakota, and J. R. Smith, "Turbocharging ambient backscatter communication," in Proc. *of the 2014 ACM conference on SIGCOMM*, Chicago Illinois USA, Aug. 2014, pp. 619–630.

[90] G. C. Alexandropoulos and M. Kountouris, "Maximal Ratio Transmission in Wireless Poisson Networks under Spatially Correlated Fading Channels," *arXiv:1508.06440*, Aug. 2015.

[91] T. K. Y. Lo, "Maximum ratio transmission," *IEEE Trans. Commun.*, vol. 47, no. 10, pp. 1458–1461, Oct. 1999.

[92] A. Wiesel, Y. C. Eldar, and S. Shamai, "Zero-Forcing Precoding and Generalized Inverses," *IEEE Trans. Signal Process.*, vol. 56, no. 9, pp. 4409–4418, Sep. 2008.

[93] T. Haynes, "A Primer on Digital Beamforming," *Spectrum Signal Processing*, vol. 11, p. 15, 1998

[94] Benson, "Phased Array Beamforming ICs Simplify Antenna Design" *Analog Dialogue*, vol. 53, p. 4, Jan 2019.

[95] M. A. Albreem, M. Juntti, and S. Shahabuddin, “Massive MIMO Detection Techniques: A Survey,” *IEEE Commun. Surv. Tutor.*, vol. 21, no. 4, pp. 3109–3132, Fourthquarter 2019.

[96] M. A. M. Moqbel, W. Wangdong, and A. Z. Ali, “MIMO Channel Estimation Using the LS and MMSE Algorithm,” *IOSR J. Electron. Commun. Eng.*, vol. 12, no. 01, pp. 13–22, Jan. 2017.

[97] S. Tiiro, J. Ylioinas, M. Myllyla, and M. Juntti, “Implementation Of The Least Squares Channel Estimation Algorithm For Mimo-Ofdm Systems,” *Int. ITG Workshop Smart Antennas*, p. 7, 2009.

[98] M. D. Renzo *et al.*, “Smart radio environments empowered by reconfigurable AI meta-surfaces: an idea whose time has come,” *EURASIP J. Wirel. Commun. Netw.*, vol. 2019, no. 1, p. 129, May 2019.

[99] G. C. Alexandropoulos, G. Lerosey, M. Debbah, and M. Fink, “Reconfigurable Intelligent Surfaces and Metamaterials: The Potential of Wave Propagation Control for 6G Wireless Communications,” *arXiv:2006.11136*, Jun. 2020.

[100] E. Basar, “Reconfigurable Intelligent Surface-Based Index Modulation: A New Beyond MIMO Paradigm for 6G,” *IEEE Trans. Commun.*, vol. 68, no. 5, pp. 3187–3196, May 2020.

[101] E. Björnson, H. Wymeersch, B. Matthiesen, P. Popovski, L. Sanguinetti, and E. de Carvalho, “Reconfigurable Intelligent Surfaces: A Signal Processing Perspective With Wireless Applications,” *arXiv:2102.00742*, Feb. 2021.

[102] E. Basar, M. Di Renzo, J. De Rosny, M. Debbah, M.-S. Alouini, and R. Zhang, “Wireless Communications Through Reconfigurable Intelligent Surfaces,” *IEEE Access*, vol. 7, pp. 116753–116773, 2019.

[103] M. Di Renzo *et al.*, “Smart Radio Environments Empowered by Reconfigurable Intelligent Surfaces: How It Works, State of Research, and The Road Ahead,” *IEEE J. Sel. Areas Commun.*, vol. 38, no. 11, pp. 2450–2525, Nov. 2020.

[104] “Press Releases : DOCOMO Conducts World’s First Successful Trial of Transparent Dynamic Metasurface,” *NTT DOCOMO Home*. January 17, 2020. https://www.nttdocomo.co.jp/english/info/media_center/pr/2020/0117_00.html.

[105] V. Arun and H. Balakrishnan, “RFocus: Beamforming Using Thousands of Passive Antennas,” in *Proceedings of the 17th USENIX Symposium on Networked Systems Design and Implementation*, Santa Clara, CA, USA, Feb. 2020, p. 17.

[106] W. Tang *et al.*, “Wireless Communications With Reconfigurable Intelligent Surface: Path Loss Modeling and Experimental Measurement,” *IEEE Trans. Wirel. Commun.*, vol. 20, no. 1, pp. 421–439, Jan. 2021.

[107] L. Dai *et al.*, “Reconfigurable Intelligent Surface-Based Wireless Communications: Antenna Design, Prototyping, and Experimental Results,” *IEEE Access*, vol. 8, pp. 45913–45923, 2020.

[108] X. Pei *et al.*, "RIS-Aided Wireless Communications: Prototyping, Adaptive Beamforming, and Indoor/Outdoor Field Trials," *arXiv:2103.00534*, Feb. 2021.

[109] Q.-U.-A. Nadeem, A. Kammoun, A. Chaaban, M. Debbah, and M.-S. Alouini, "Intelligent Reflecting Surface Assisted Wireless Communication: Modeling and Channel Estimation," *arXiv:1906.02360*, Dec. 2019.

[110] J. Chen, Y.-C. Liang, H. V. Cheng, and W. Yu, "Channel Estimation for Reconfigurable Intelligent Surface Aided Multi-User MIMO Systems," *arXiv:1912.03619*, Dec. 2019.

[111] S. Ali *et al.*, "6G White Paper on Machine Learning in Wireless Communication Networks," *arXiv:2004.13875*, Apr. 2020.

[112] P. Yang, Y. Xiao, M. Xiao, and S. Li, "6G Wireless Communications: Vision and Potential Techniques," *IEEE Netw.*, vol. 33, no. 4, pp. 70–75, Jul. 2019.

[113] A. Zappone, M. D. Renzo, and M. Debbah, "Wireless Networks Design in the Era of Deep Learning: Model-Based, AI-Based, or Both?," *IEEE Trans. Commun.*, vol. 67, no. 10, pp. 7331–7376, Oct. 2019.

[114] J. Gao, C. Zhong, X. Chen, H. Lin, and Z. Zhang, "Unsupervised Learning for Passive Beamforming," *arXiv:2001.02348*, Jan. 2020.

[115] Z. Mhanna, A. Sibille, R. Contreras, and C. Roblin, "Statistical characterization of channel polarization for RFID backscattering channels," in *2013 7th European Conference on Antennas and Propagation (EuCAP)*, Apr. 2013, pp. 1883–1887.

[116] S. Hebib, S. Bouaziz, H. Aubert, and F. Lerasle, "Antennes lecteurs RFID à polarisation circulaire pour application robotique," in *17èmes Journées Nationales Microondes*, Brest, France, May 2011, pp. 1–4.

[117] P. Yang, M. D. Renzo, Y. Xiao, S. Li, and L. Hanzo, "Design Guidelines for Spatial Modulation," *IEEE Commun. Surv. Tutor.*, vol. 17, no. 1, pp. 6–26, Firstquarter 2015.

[118] P. Yang *et al.*, "Single-Carrier SM-MIMO: A Promising Design for Broadband Large-Scale Antenna Systems," *IEEE Commun. Surv. Tutor.*, vol. 18, no. 3, pp. 1687–1716, thirdquarter 2016.

[119] M. Di Renzo, "Spatial modulation based on reconfigurable antennas — A new air interface for the IoT," in *MILCOM 2017 - 2017 IEEE Military Communications Conference (MILCOM)*, Baltimore, MD, Oct. 2017, pp. 495–500.

[120] E. Basar, M. Wen, R. Mesleh, M. Di Renzo, Y. Xiao, and H. Haas, "Index Modulation Techniques for Next-Generation Wireless Networks," *IEEE Access*, vol. 5, pp. 16693–16746, 2017.

[121] M. Wen *et al.*, "A Survey on Spatial Modulation in Emerging Wireless Systems: Research Progresses and Applications," *IEEE J. Sel. Areas Commun.*, vol. 37, no. 9, pp. 1949–1972, Sep. 2019.

[122] R. Long, G. Yang, Y. Pei, and R. Zhang, "Transmit Beamforming for Cooperative

Ambient Backscatter Communication Systems," in *GLOBECOM 2017 - 2017 IEEE Global Communications Conference*, Dec. 2017, pp. 1–6.

[123] E. Onggosanusi *et al.*, "Modular and High-Resolution Channel State Information and Beam Management for 5G New Radio," *IEEE Commun. Mag.*, vol. 56, no. 3, pp. 48–55, Mar. 2018.

[124] T. Kashima *et al.*, "Large scale massive MIMO field trial for 5G mobile communications system," in *2016 International Symposium on Antennas and Propagation (ISAP)*, Oct. 2016, pp. 602–603.

[125] Technical Specification Group Radio Access Network, "3GPP TS 38.201 V15.0.0 (2017-12) Technical Specification 3rd Generation Partnership Project," Dec. 2017. https://www.etsi.org/deliver/etsi_ts/138200_138299/138201/15.00.00_60/ts_138201v150000p.pdf.

[126] H. Sampath, P. Stoica, and A. Paulraj, "Generalized linear precoder and decoder design for MIMO channels using the weighted MMSE criterion," *IEEE Trans. Commun.*, vol. 49, no. 12, pp. 2198–2206, Dec. 2001.

[127] J. Zhao, W. Gong, and J. Liu, "Spatial Stream Backscatter Using Commodity WiFi," in *Proceedings of the 16th Annual International Conference on Mobile Systems, Applications, and Services*, New York, NY, USA, Jun. 2018, pp. 191–203.

[128] X. Liu, Z. Chi, W. Wang, Y. Yao, and T. Zhu, "VMscatter: A Versatile MIMO Backscatter," in *Proceedings of the 17th USENIX Symposium on Networked Systems Design and Implementation (NSDI '20)*, Santa Clara, CA, USA, Feb. 2020, p. 17.

[129] P. Pajusco, F. Gallee, N. Malhouroux, and R. Burghelea, "Massive antenna array for space-time channel sounding," in *2017 11th European Conference on Antennas and Propagation (EUCAP)*, Paris, France, Mar. 2017, pp. 865–868.

[130] Y.-C. Liang, Q. Zhang, E. G. Larsson, and G. Y. Li, "Symbiotic Radio: Cognitive Backscattering Communications for Future Wireless Networks," *arXiv:2007.01506*, Jul. 2020.

[131] R. Karasik, O. Simeone, M. Di Renzo, and S. Shamai, "Single-RF Multi-User Communication Through Reconfigurable Intelligent Surfaces: An Information-Theoretic Analysis," *arXiv:2101.07556*, Jan. 2021.

[132] A. Abrardo, D. Dardari, M. Di Renzo, and X. Qian, "MIMO Interference Channels Assisted by Reconfigurable Intelligent Surfaces: Mutual Coupling Aware Sum-Rate Optimization Based on a Mutual Impedance Channel Model," *arXiv:2102.07155*, Feb. 2021.

[133] J. M. Baracco, P. Ratajczak, P. Brachat, J. M. Fargeas, and G. Toso, "Reconfigurable Antennas Demonstrators Using Varactors Technology," presented at the 39th ESA Antenna Workshop on Innovative Antenna Systems and Technologies for Future Space Missions, ESA/ESTEC, Noordwijk, The Netherlands, Oct. 2018.

[134] P. Ratajczak, P. Brachat, J. Fargeas, and J. Baracco, "C-band active reflectarray based

on high impedance surface," in *2013 IEEE International Symposium on Phased Array Systems and Technology*, Oct. 2013, pp. 570–576.